Diploma Thesis

Tensile stresses in a concrete slab under central Falling Weight Deflectometer loading, as a function of thermal curling, and its prediction from the surface temperature history: field tests and structural analysis

submitted in satisfaction of the requirements for the degree
Diplom-Ingenieur
of the TU Wien, Faculty of Civil and Environmental Engineering

---

Diplomarbeit

Zugspannungen in einer Betonfahrbahnplatte unter zentraler Fallgewichts-Deflektometer-Belastung, als Funktion der thermischen Aufwölbung, und ihre Vorhersage aus dem Oberflächentemperaturverlauf: Feldversuche und Strukturanalyse

ausgeführt zum Zwecke der Erlangung des akademischen Grads
Diplom-Ingenieur
eingereicht an der TU Wien, Fakultät für Bau- und Umweltingenieurwesen

Lukas Seeliger, BSc

Matr.Nr.: 11912379

Betreuung: Univ. Prof. Dipl.-Ing. Dr. techn. **Bernhard Pichler**
Proj. Ass.in Dipl.-Ing.in **Sophie Schmid**, BSc
Institut für Mechanik der Werkstoffe und Strukturen
Technische Universität Wien
Karlsplatz 13/202, 1040 Wien, Österreich

Wien, im Jänner 2025

Abstract

Pavement structures endure many load cycles, leading to concrete fatigue in rigid pavements, making design challenging. This thesis focuses on quantifying tensile stresses in concrete slabs caused by FWD testing on curled slabs and by traffic running over them, respectively. "Curling" refers to slab curvature due to non-uniform temperature distribution. Two challenges are addressed using real-scale experiments at field testing sites and engineering mechanics modeling with analytical solutions, minimizing Finite Element simulations to the possible minimum.

Challenge 1 refers to quantifying tensile stresses experienced by a concrete-over-asphalt pavement on Austria's highway A10, resulting from 19 central Falling Weight Deflectometry (FWD) tests. Despite identical test execution, measured surface deflections varied. Temperature data from four slab depths during FWD testing are used to quantify the concrete slab's thermal eigencurvature. This allows for showing a linear increase in deflections with negative eigencurvature. Tensile stresses at the slab's underside center are quantified by dividing the problem into three load cases: (i) dead load of the curled slab, (ii) thermal eigenstresses of concrete, and (iii) impact of the falling weight. Load case (i) involves a nonlinear contact problem due to slab lift-off, solved using Finite Element simulations for a plate resting on a Winkler foundation. The computed tensile stresses increase nonlinearly with negative eigencurvature, while being practically independent of the modulus of subgrade reaction. Load case (ii) is computed analytically. Thermal eigenstresses show a non-trivial hysteretic correlation with the eigencurvature of the slab. Load case (iii) refers to the slab's configuration changes resulting from FWD testing. The related structural model refers to a single plate with free edges on a Winkler foundation, extended by uniform subgrade stress. The modulus of subgrade reaction and the additional uniform subgrade stress are optimized for every FWD test, to replicate the measured deflections. Tensile stresses are computed analytically. They increase moderately with negative eigencurvature.

Challenge 2 refers to the prediction of the slab's thermal eigencurvature using the slab's surface temperature history as boundary condition for one-dimensional heat ingress into a half-space. The heat conduction problem is solved analytically, providing the temperature profile and enabling eigencurvature computation. Application to data from a field testing site on Austria's highway A2 shows that seven days of temperature history, with measurements every 15 minutes, are sufficient for eigencurvature prediction.

Finally, implications for operation of highways and pavement design are discussed. Slab stresses due to a design wheel load of 50 kN are quantified by linear scaling of the stresses from load case (iii) and superposing them with the stresses from load cases (i) and (ii). When a design vehicle travels over a slab with large negative eigencurvature and eigenstresses, the resulting tensile stresses can be up to six times larger than when the vehicle travels over the slab with small eigencurvature and eigenstresses. Thus, it is recommendable to operate truck weighing stations during periods of significant tensile stresses, and to schedule heavy-load transport during the earlier morning when both the eigencurvature of the slab and the eigenstresses of concrete are small. The thermo-mechanical model from Challenge 2 allows for real-time monitoring of the eigencurvature evolution using surface temperature data from ice warning systems. In the future, it will be interesting to combine eigencurvature evolutions with data from traffic monitoring systems, such that realistic tensile stress histories can be determined as exposure conditions for the fatigue assessment of concrete pavement slabs.

Kurzfassung

Straßen sind zahlreichen Belastungszyklen ausgesetzt, wodurch es bei starrer Bauweise zur Betonermüdung kommt. Die vorliegende Diplomarbeit befasst sich mit der Quantifizierung von Zugspannungen in Betonfahrbahnplatten im aufgewölbten Zustand, hervorgerufen durch Fallgewichts-Deflektometer (FWD) Versuche. Der Begriff „Aufwölbung“ bezeichnet dabei die Verformung der Platte aufgrund einer ungleichmäßigen Temperaturverteilung. Zwei Problemstellungen werden mit Hilfe von Versuchen an Feldmessstellen und ingenieurmechanischen Modellen gelöst, wobei Finite Elemente Simulationen auf ein Minimum reduziert werden.

Problemstellung 1 bezieht sich auf das Quantifizieren der Zugspannungen in einer Betonfahrbahnplatte auf der Autobahn A10, hervorgerufen durch 19 zentrale FWD Versuche. Die gemessenen Durchbiegungen steigen linear mit wachsender negativer thermischer Eigenverkrümmung der Platte an. Letztere wird aus Temperaturen, die in vier Tiefen während der FWD Versuche gemessen wurden, berechnet. Zum Quantifizieren der Zugspannungen in der Mitte der Plattenunterseite wird das Problem in drei Lastfälle unterteilt: (i) Eigengewicht der aufgewölbten Platte, (ii) thermische Eigenspannungen des Betons und (iii) Aufprall des Fallgewichts. In Lastfall (i) wird ein nichtlineares Kontaktproblem mit Hilfe von Finite-Elemente-Simulationen gelöst. Die berechneten Zugspannungen nehmen nichtlinear mit negativer Eigenverkrümmung zu, sind aber nahezu unabhängig vom Bettungsmodul. Der Lastfall (ii) wird analytisch berechnet. Die thermischen Eigenspannungen zeigen eine nicht-triviale hysteretische Korrelation mit der Eigenkrümmung der Platte. Der Lastfall (iii) beschreibt die Lageänderung der Platte zufolge der FWD-Tests. Das zugehörige Strukturmodell bezieht sich auf eine einzelne Platte mit freien Rändern auf einer Winklerbettung, welche durch eine gleichmäßige Bettungsspannung erweitert wird. Der Bettungsmodul und die zusätzliche gleichmäßige Bettungsspannung werden für jeden FWD-Test optimiert, um die gemessenen Durchbiegungen zu reproduzieren. Die Zugspannungen werden analytisch berechnet und nehmen mit negativer Eigenverkrümmung nur mäßig zu.

Problemstellung 2 bezieht sich auf die Vorhersage der thermischen Eigenverkrümmung der Platte unter Verwendung ihres Oberflächentemperaturverlaufs als Randbedingung für den eindimensionalen Wärmeeintrag in einen Halbraum. Das Wärmeleitungsproblem wird analytisch gelöst. Das daraus folgende Temperaturprofil ermöglicht die Berechnung der Eigenverkrümmung der Platte. Die Anwendung auf Temperaturdaten einer Feldmessstelle auf der Autobahn A2 zeigt, dass Temperaturmessungen über sieben Tage mit einem 15-minütigen Messintervall für die Vorhersage der Eigenverkrümmung ausreichen.

Abschließend wird die Bedeutung der Arbeit für den Autobahnbetrieb und die Bemessung diskutiert. Spannungen infolge einer Bemessungsradlast von 50 kN werden durch lineare Skalierung der Spannungen aus Lastfall (iii) und Überlagerung mit den Spannungen aus den Lastfällen (i) und (ii) erhalten. Eine Überfahrt über eine stark aufgewölbte Platte mit großen thermischen Eigenspannungen weckt Zugspannungen, die bis zu sechsmal größer sind als bei der gleichen Überfahrt im kaum aufgewölbten Zustand ohne nennenswerte thermische Eigenspannungen. Es ist daher empfehlenswert, LKW-Wiegestationen in Zeiten mit starker Zugspannungsbelastung zu betreiben und Schwerlasttransporte in den frühen Morgenstunden durchzuführen, weil dann sowohl die Eigenverkrümmung als auch die Eigenspannungen klein sind. Das thermo-mechanische Modell (Problemstellung 2) ermöglicht dabei die Echtzeitberechnung der Eigenverkrümmung durch Oberflächentemperaturmessungen von Frostspionen.

Danksagung

An dieser Stelle möchte ich all jenen danken, die mich bei der Erstellung der vorliegenden Diplomarbeit unterstützt haben. Allen voran gilt mein besonderer Dank Herrn Univ. Prof. Dipl.-Ing. Dr. techn. Bernhard Pichler für die Hauptbetreuung der Arbeit, die zahlreichen fachlichen Diskussionen, sowie die inhaltliche und sprachliche Unterstützung. Besonders möchte ich mich auch bei Frau Proj. Ass.in Dipl.-Ing.in Sophie Schmid, BSc für die zahlreichen Diskussionen sowie die begleitende Unterstützung und Betreuung bedanken. Bei Herrn Dipl.-Ing. Dr. techn. Rodrigo Díaz Flores und Herrn Assistant Prof. Dipl.-Ing. Dr. techn. Lukas Eberhardsteiner möchte ich mich für spannende Diskussionen bedanken. Herrn Dipl.-Ing. Dr. techn. Valentin Donev (Asfinag), Herrn Univ. Ass. Dipl.-Ing. Silvio Roth (TU Wien), Herrn Michael Celadnik und Herrn Philip Krcha (beide Nievelt Labor GmbH) danke ich für das Durchführen der zahlreichen FWD Versuche sowie das Bereitstellen der Daten. Zusätzlich sei dem gesamten Baustatik-Team gedankt, das mich überzeugt hat, als studentischer Mitarbeiter am Institut für Mechanik der Werkstoffe und Strukturen tätig zu werden. Stellvertretend möchte ich an dieser Stelle Herrn Univ. Ass. Dipl.-Ing. Maximilian Sorgner, BSc für die Betreuung meiner Bachelorarbeit danken.

Ein besonderer Dank gilt auch meiner Familie. Meinen Eltern, Gabi und Bruno, und meinem Bruder Thomas danke ich für ihre bedingungslose Unterstützung und Förderung, nicht nur während meines Studiums, sondern während meines gesamten Lebens. Ihr habt einerseits dafür gesorgt, dass ich mich voll und ganz auf mein Studium konzentrieren konnte, und anderseits habt ihr mir in schwierigen Phasen die wertvolle Ablenkung und den nötigen Ausgleich geboten.

Abschließend möchte ich mich bei meinen Studienkolleginnen und -kollegen bedanken, die im Laufe der Semester zu meinen Freundinnen und Freunden wurden. Dank euch werden mir sogar die längsten Nachtsessions sowie die zahlreichen Online-Lehrveranstaltungen während der Pandemie in lustiger Erinnerung bleiben.

Contents

Chapter 1

Introduction

A primary objective of pavement design is to guarantee a long service life. Pavement structures are subjected to many thousands of vehicle passages over the course of their service life. Each passage represents a load cycle. Consequently, the resistance of the pavement structure against fatigue is of critical importance. Focusing on rigid pavements, several fatigue strength models have been introduced, see e.g. [17, 20, 22, 23]. When it comes to quantification of the allowable number of load cycles of a concrete slab, the tensile stress-to-strength ratio of the load cycles represents a central input to fatigue models. In Austria, the design of rigid pavements is based on the fatigue model after Smith [13, 14]. In this approach, tensile stresses due to temperature-induced curling are superimposed with tensile stresses due to traffic load [2]. Thereby, "curling" refers to the thermal eigencurvature of a concrete slab resulting from a non-uniform temperature distribution across its thickness.

Curling stresses are quantified based on an estimated worst-case linear temperature gradient [2]. This approach can be traced back to the late 1920s, when Westergaard [29, 30] quantified stresses caused by linear temperature gradients in concrete slabs with infinite dimensions resting on a Winkler foundation [31]. Bradbury [4] adapted this approach to finite slabs. Both assumed a full-face contact between the slab and the next lower layer of the pavement structure. Modern design approaches account for the partial lift-off of the curled concrete slab [14]. In contrast to the prescribed linear temperature gradients used in design guides, in situ temperature measurements, see e.g. [1, 6, 21], have demonstrated spatially nonlinear temperature profiles. They can be subdivided into three parts: (i) a constant, (ii) a linear, and (iii) a nonlinear part [25]. The linear part results in temperature-induced curling and consequently curling stresses. The nonlinear part causes temperature-induced warping which is prevented at the scale of plate generators and consequently leads to self-equilibrated thermal eigenstresses of concrete [19].

As for the stresses under traffic load, Falling Weight Deflectometer (FWD) testing is a frequently used non-destructive test method that simulates traffic loading. It consists of dropping a standardized mass (= falling weight) from a defined height onto a damping element placed on top of the pavement structure. This impact results in a dynamic excitation of the pavement structure. In several distances from the center of the falling weight, surface deflection histories are recorded by means of displacement sensors called geophones. Usually, the geophones are aligned with the driving direction. Recently, benefits resulting from a star-shaped [7] and T-shaped [8] arrangement of geophones in central FWD testing on concrete slabs have been demonstrated.

The interpretation of FWD data remains a challenging task, especially when testing is performed on multilayered pavement structures. Repeated FWD testing at the same position, but at different dates, results in measured deflections which vary from test to test. Environmental factors such as moisture content and temperature are responsible for varying FWD test results according to the state-of-the-art knowledge in the field [26]. This is of particular significance for composite pavement structures, which consist of asphalt *and* concrete layers, for three reasons: (i) the stiffness of the subgrade exhibits a seasonal variation, (ii) the temperature-dependent stiffness of asphalt, and (iii) temperature-induced curling of the concrete layer. Curling can lead to

partial loss of full-face contact between the concrete slab and the adjacent layer. Notably, such loss of contact was confirmed through sledgehammer tests on a field testing site equipped with embedded accelerometers [11].

The present master thesis presents the results from 19 FWD tests, of which 14 were performed over the course of 24 hours. All FWD tests were conducted at the center of a concrete pavement slab of the emergency lane at a well-instrumented field testing site located on the highway A10 in Austria. Although, all FWD tests were performed with the same equipment and applying the same dynamic load, different surface deflections were measured. Herein, the differences are attributed to the varying temperature profiles within the pavement structure during FWD testing. The field testing site is equipped with temperature sensors, providing insights into the temperature profiles. Surface temperature measurements and temperature readings at the top, mid-depth, and the bottom of the "bottom concrete"-layer allow for quantifying the thermal eigencurvature of the concrete slab resulting in curling. A correlation analysis will be performed to study the relation between the eigencurvature of the slab and the measured deflections at different distances from the falling weight. Additionally, the largest tensile stresses under central FWD testing on the curled concrete slab will be computed by means of structural analysis. The problem at hand will be subdivided into three load cases: (i) dead load and curling of the slab, (ii) thermal eigenstresses of concrete, and (iii) FWD testing. As for the first load case, curling stresses will be computed by means of nonlinear Finite Element simulations inspired by [19]. The concrete slab will be modeled as a single plate with free edges, resting on a Winkler foundation, summarizing all the properties of the layers underneath into a single value: the modulus of subgrade reaction. As for the second load case, thermal eigenstresses of concrete will be computed analytically [19]. As for the third load case, the pointwisely measured FWD data will be replicated by a structural model based on Kirchhoff's linear theory of thin plates [18]. It is focused on the concrete slab resting again on a Winkler foundation, but this time extended by a uniform subgrade stress [7]. The replicated deflection field will then be inserted into the constitutive relations of the plate theory to compute stresses resulting from central FWD testing. Superimposing the three stress contributions will yield the total tensile stresses at the slab's underside center as a function of the thermal eigencurvature of the slab.

A thermo-mechanical model will be introduced to quantify the evolution of the thermal eigencurvature of concrete pavement slabs based on temperature histories measured at the slab's *surface*. The multilayered pavement structure will be modeled as an isotropic and homogeneous half-space. The measured surface temperature histories will be prescribed as boundary condition for one-dimensional heat ingress into the half-space. The problem will be solved by means of a series-solution, providing access to the temporal evolution of the temperature field within the concrete slab. A series-solution for the thermal eigencurvature will then be derived utilizing Kirchhoff's hypothesis. Finally, the thermo-mechanical model will be applied to a concrete pavement slab with in situ temperature monitoring located on the highway A2 in Austria. The simulated evolution of the thermal eigencurvature will be compared with values of the eigencurvature computed directly from temperatures measured inside the bulk of the concrete slab. In order to ensure a well-converged solution, sensitivity analyses regarding the minimum duration of the surface temperature history and the maximum time step size will be performed.

The present master thesis is structured as follows. Chapter 2 refers to the quantification of tensile stresses resulting from central FWD testing on a curled concrete slab at the aforementioned field testing site. Chapter 3 is devoted to the quantification of the thermal eigencurvature of concrete pavement slabs as a function of a measured surface temperature history. In Chapter 4 the implications for pavement design and operation of highways will be discussed. Chapter 5 contains the conclusions drawn from the present thesis.

Chapter 2

Tensile stresses resulting from central FWD testing on a curled concrete slab

2.1 Field tests: FWD and temperature measurements

FWD and temperature data were collected at a field testing site located on the highway "A10 – Tauern Autobahn" in Austria [11]. The concrete-over-asphalt composite pavement structure is composed of six layers. From the topmost to the bottommost layer they read as: top concrete (with thickness $h_{tc} = 5.0\,\text{cm}$), bottom concrete ($h_{bc} = 22.0\,\text{cm}$), asphalt ($h_{as} = 8.2\,\text{cm}$), cement-stabilized granular layer ($h_{cs} = 17.6\,\text{cm}$), unbound granular layer ($h_{ub} = 31.4\,\text{cm}$), and local subgrade, see Fig. 2.1(a) and [9, 11]. The top concrete was installed wet-on-wet on the bottom concrete. Thus, the concrete slab is a monolithic, two-layered composite structure. Its length, width, and thickness amount to 5.00 m, 3.50 m, and 0.27 m, respectively, see Fig. 2.1(b) and Tab. 2.1 for the geometric dimensions of the slab and the material properties of the concretes.

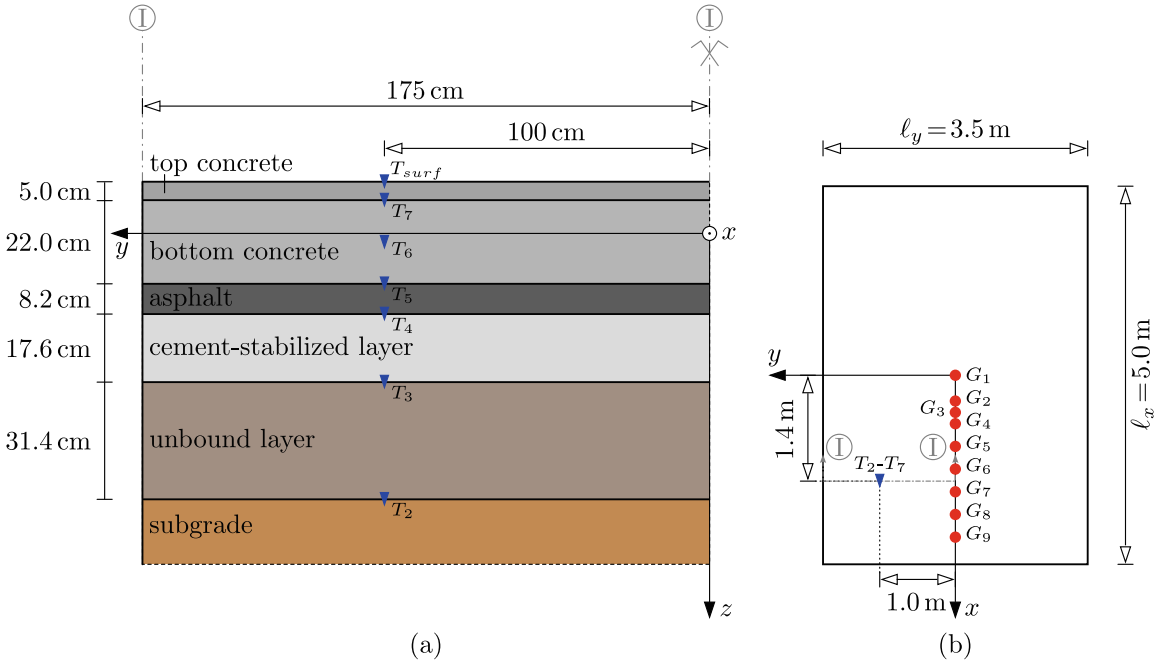

Fig. 2.1: FWD field testing site "A10": (a) cross section showing one half of the concrete-over-asphalt composite pavement structure and the vertical positions of temperature sensors, i.e. the six embedded sensors T_2 to T_7 and that at the surface labeled as T_{surf}, see blue triangles, and (b) top view of the concrete slab, illustrating the horizontal positions of the temperature sensors and geophones, see the blue triangle and the red circles, respectively.

Tab. 2.1: Geometric dimensions of the concrete slab "A10" consisting of two layers, and material properties of the concrete layers

Property	Value	Source
Length of the slab	$\ell_x = 5.0\,\mathrm{m}$	
Width of the slab	$\ell_y = 3.5\,\mathrm{m}$	
Thickness of the top concrete layer	$h_{tc} = 0.05\,\mathrm{m}$	
Thickness of the bottom concrete layer	$h_{bc} = 0.22\,\mathrm{m}$	
Modulus of elasticity of top concrete	$E_{tc} = 34.1\,\mathrm{GPa}$	[9]
Modulus of elasticity of bottom concrete	$E_{bc} = 46.3\,\mathrm{GPa}$	[9]
Mass density of top concrete	$\rho_{tc} = 2305\,\mathrm{kg/m^3}$	[11]
Mass density of bottom concrete	$\rho_{bc} = 2390\,\mathrm{kg/m^3}$	[11]

The field testing site is equipped with six embedded Pt100 sensors for in situ temperature monitoring, see blue triangles labeled as T_2 to T_7 in Fig. 2.1(a). They were embedded during the rehabilitation of the highway [11]. Positioned along a vertical axis, five sensors were installed at the interfaces between neighboring layers [9], and the sixth sensor, T_6, is situated at mid-depth of the bottom concrete layer, see Fig. 2.1(a). The sensors are positioned eccentric to the center of the slab, in order to decrease their influence on the behavior of the pavement during central FWD tests. The horizontal distance from the slab center amounts to 1.4 m in driving direction and to 1.0 m in lateral direction, see Fig. 2.1(b). The surface temperature was measured by means of a digital infrared thermometer, see the blue triangle labeled by T_{surf} in Fig. 2.1(a). The described sensor arrangement enabled a good spatial resolution of the temperature profile in the pavement structure during FWD testing.

Central FWD tests were performed at 19 distinct instants of time. 14 tests were performed during 24 hours, between 13h13 on Sep 13, 2022 and 13h39 on Sep 14, 2022. Five additional FWD tests were conducted during the period spanning from Jul, 2021 to Mar, 2022 [9]. All FWD tests were performed with a Dynatest 8082 trailer-mounted Heavy Weight Deflectometer, which applied a maximum force of 200 kN [9]. Nine geophones recorded the maximum deflections during the 14 tests in Sep, 2022. Eight geophones were used during the five tests conducted from Jul, 2021 to Mar, 2022. The displacement sensors were located at radial distances r_i from the center of the slab, ranging from 0.0 m to 2.1 m, see Fig. 2.1(b). Typically, multiple tests were performed right after another, see Tab. 2.2 for average values of the maximum deflections measured. The temperatures measured during FWD testing are listed in Tab. 2.3. The surface temperature ranged from −0.5 °C in Jan, 2022 to 28.2 °C at 15h09 on Sep 13, 2022.

Different deflections were measured, despite the fact that all FWD tests were performed at the same field testing site using the same measurement equipment and applying the same dynamic load. Thus, the measured differences are attributed to different temperature profiles within the pavement structure.

Tab. 2.2: Data from central FWD testing on the field testing site of highway A10: average values of maximum surface deflections measured in n_{FWD} tests at specific radial distances from the center of the slab.

		Deflections [mm] measured at a radial distance of:								
		$r_1 = 0.0\,\text{m}$	$r_2 = 0.3\,\text{m}$	$r_3 = 0.45\,\text{m}$	$r_4 = 0.6\,\text{m}$	$r_5 = 0.9\,\text{m}$	$r_6 = 1.2\,\text{m}$	$r_7 = 1.5\,\text{m}$	$r_8 = 1.8\,\text{m}$	$r_9 = 2.1\,\text{m}$
Time/Date	n_{FWD}	w_1	w_2	w_3	w_4	w_5	w_6	w_7	w_8	w_9
13h13	5	0.197	0.176	0.163	0.150	0.127	0.104	0.085	0.067	0.056
14h03	5	0.203	0.181	0.167	0.154	0.131	0.105	0.089	0.068	0.059
15h09	5	0.209	0.182	0.169	0.156	0.133	0.104	0.085	0.069	0.061
16h11	5	0.201	0.177	0.164	0.152	0.126	0.103	0.085	0.068	0.058
17h28	5	0.198	0.172	0.158	0.146	0.122	0.099	0.082	0.065	0.054
18h08	5	0.190	0.167	0.155	0.144	0.120	0.098	0.082	0.068	0.056
19h20	5	0.182	0.158	0.147	0.136	0.116	0.095	0.078	0.063	0.058
20h33	5	0.174	0.153	0.141	0.132	0.112	0.092	0.079	0.065	0.054
21h22	5	0.170	0.148	0.138	0.127	0.108	0.093	0.075	0.066	0.055
07h35	5	0.160	0.138	0.128	0.120	0.103	0.087	0.075	0.064	0.055
09h05	3	0.159	0.139	0.130	0.122	0.104	0.088	0.076	0.064	0.055
10h03	3	0.163	0.143	0.134	0.124	0.105	0.089	0.077	0.065	0.055
12h44	5	0.184	0.163	0.151	0.141	0.119	0.099	0.082	0.068	0.057
13h39	5	0.195	0.172	0.159	0.147	0.124	0.102	0.084	0.070	0.058
Jul 2021	15	0.186	0.167	–	0.144	0.122	0.103	0.086	0.072	0.061
Sep 2021	15	0.176	0.157	–	0.135	0.115	0.099	0.081	0.068	0.055
Oct 2021	17	0.169	0.150	–	0.131	0.110	0.092	0.075	0.062	0.052
Jan 2022	12	0.166	0.147	–	0.129	0.109	0.091	0.076	0.061	0.052
Mar 2022	12	0.171	0.152	–	0.130	0.109	0.095	0.076	0.066	0.052

Tab. 2.3: Data from central FWD testing on the field testing site of highway A10: temperatures measured at specific depths of the pavement structure.

	Temperatures [°C] measured in depths of:						
	$\bar{z}_{surf} = 0.00\,\text{m}$	$\bar{z}_7 = 0.05\,\text{m}$	$\bar{z}_6 = 0.16\,\text{m}$	$\bar{z}_5 = 0.27\,\text{m}$	$\bar{z}_4 = 0.35\,\text{m}$	$\bar{z}_4 = 0.53\,\text{m}$	$\bar{z}_2 = 0.84\,\text{m}$
Time/Date	T_{surf}	T_7	T_6	T_5	T_4	T_3	T_2
13h13	27.0	23.9	19.1	16.1	16.4	17.2	17.9
14h03	28.0	25.8	20.5	16.7	16.5	17.1	17.9
15h09	28.2	27.1	22.1	17.4	16.9	17.1	17.9
16h11	24.4	26.9	23.1	18.1	17.3	17.1	17.8
17h28	23.7	24.7	23.0	19.0	17.9	17.2	17.8
18h08	23.5	24.5	22.9	19.3	18.2	17.3	17.8
19h20	22.0	22.7	22.3	19.7	18.7	17.5	17.8
20h33	19.9	21.5	21.7	19.8	19.0	17.6	17.8
21h22	18.3	20.6	21.2	19.8	19.1	17.7	17.8
07h35	14.7	16.3	17.1	18.1	18.4	18.4	17.9
09h05	16.7	16.7	17.1	17.8	18.2	18.3	18.0
10h03	18.5	17.4	17.2	17.8	18.1	18.3	18.0
12h44	23.5	21.7	19.2	17.8	18.0	18.2	18.0
13h39	26.5	23.7	20.2	18.0	18.0	18.2	18.0
Jul 2021	25.5	24.7	22.4	22.1	22.4	21.1	19.6
Sep 2021	20.5	19.2	17.3	17.6	18.2	18.9	18.3
Oct 2021	10.5	10.5	8.8	9.0	9.6	11.0	12.7
Jan 2022	−0.5	−0.6	−0.7	−0.3	0.1	0.7	1.5
Mar 2022	8.5	8.7	8.5	9.2	9.7	9.8	8.4

2.2 Correlation of measured deflections with the eigencurvature of the concrete slab

Curling of a concrete slab results from temperature gradients along its thickness. This provides the motivation to quantify the thermal eigencurvature during the FWD tests based on measured temperature values T_5, T_6, T_7, and T_{surf}. To this end, a Cartesian x, y, z-coordinate system is introduced, with its origin situated at the geometric center of the slab. The midplane of the concrete slab is described by the x- and y-axes, with the x-axis being oriented in the driving direction. The z-axis runs downward in thickness direction, perpendicular to the midplane, see Fig. 2.1. The temperature profile across the concrete slab is approximated by means of a quadratic polynomial, as proposed in e.g. [6, 19]:

$$T(z,t) \approx A_0(t) + A_1(t)\left(\frac{z}{h}\right) + A_2(t)\left(\frac{z}{h}\right)^2, \tag{2.1}$$

where $A_0(t)$, $A_1(t)$, and $A_2(t)$ denote coefficients that are determined such as to ensure an optimal fitting between Eq. (2.1) and the measured temperatures in Tab. 2.3 for each time instant t, see Fig. A.1(a) of Appendix A for the fitted temperature profiles.

The thermal eigencurvature κ^e of a concrete pavement slab is, at any time t, equal to the first moment of the thermal eigenstrain distribution prevailing at that time [19]:

$$\kappa^e(t) = \frac{12}{h^3}\int_{-\frac{h}{2}}^{+\frac{h}{2}} \alpha_T \left[T(z,t) - T_{ref}\right] z \, \mathrm{d}z\,, \tag{2.2}$$

where α_T denotes the coefficient of thermal expansion of concrete, see Tab. 2.5, and T_{ref} denotes the reference temperature at which the slab is free of thermal eigenstrains. The thermal eigencurvature of the concrete slab at time t, is obtained by inserting the parabolic temperature field of Eq. (2.1) into Eq. (2.2) as:

$$\kappa^e(t) = \frac{\alpha_T}{h} A_1(t)\,. \tag{2.3}$$

The thermal eigencurvatures during the 19 FWD tests, computed by means of Eqs. (2.1)–(2.3) from the measured temperatures in Tab. 2.3, range from -4.90×10^{-4}/m at 14h03 on Sep 13 to $+1.32 \times 10^{-4}$/m at 07h35 on Sep 14, see Tab. 2.4. During 14 out of the total 19 FWD tests, the temperature profile within the concrete pavement slab results in negative thermal eigencurvatures.

The measured deflections (Tab. 2.2) decrease linearly with increasing thermal eigencurvature (Tab. 2.4), see Fig. 2.2. The absolute value of the slope decreases with increasing distance from the center of the falling weight. These results underline a strong correlation of the deflections measured during FWD testing and the temperature-induced eigencurvature of the concrete slab.

Tab. 2.4: Eigencurvature of the curled concrete slab "A10" at the time instants of FWD testing: κ^e according to Eq. (2.3) after fitting the temperature data T_5, T_6, T_7, and T_{surf} from Tab. 2.3 by means of the quadratic polynomial defined in Eq. (2.1).

Time/Date	κ^e [10^{-4}/m]
13h13	−4.62
14h03	−4.90
15h09	−4.74
16h11	−3.08
17h28	−2.11
18h08	−1.90
19h20	−1.00
20h33	−0.13
21h22	+0.50
07h35	+1.32
09h05	+0.48
10h03	−0.22
12h44	−2.40
13h39	−3.55
Jul 2021	−1.54
Sep 2021	−1.27
Oct 2021	−0.78
Jan 2022	+0.07
Mar 2022	+0.24

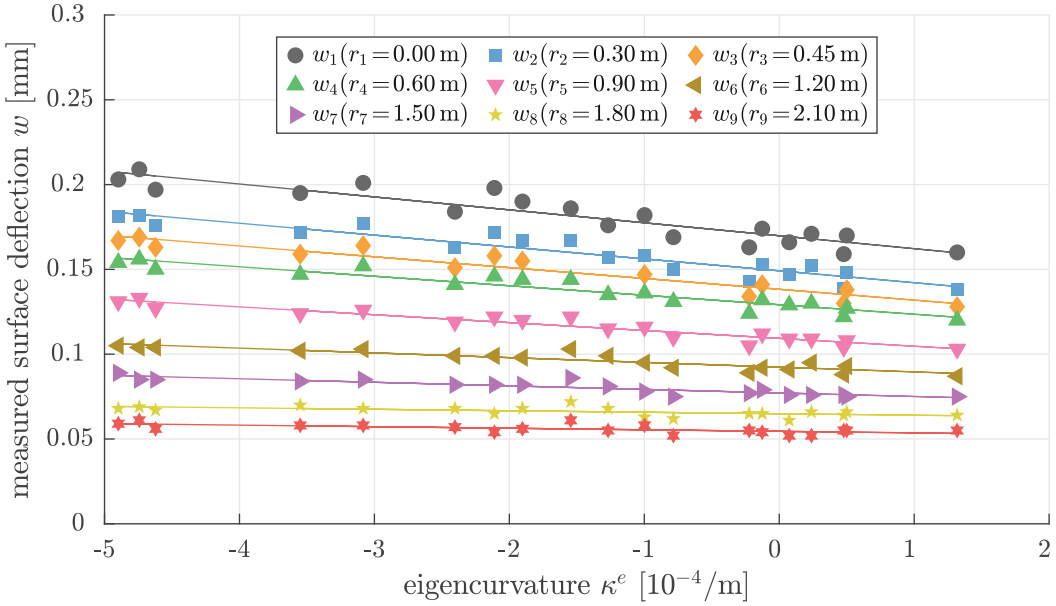

Fig. 2.2: Maximum surface deflections w_i, measured at radial distances r_i during 19 FWD tests on the concrete slab "A10", as a function of the eigencurvature κ^e of the slab: markers illustrate values from Tabs. 2.2 and 2.4, the solid graphs are best linear trendlines for surface deflections at specific radial distances.

2.3 Structural model and load case decomposition

In the remainder of this chapter, maximum tensile stresses experienced by the curled concrete slab during central FWD testing will be quantified. For the sake of simplicity, the monolithic, two-layered composite slab is introduced as a homogeneous plate, see Tab. 2.5 for its geometric dimensions and its material properties.

Tab. 2.5: Geometric dimensions of the structural model of the concrete slab "A10", dead load of the slab, flexural rigidity of the slab, and its effective homogeneous material properties.

Property	Value	Source
Length of the slab	$\ell_x = 5.0\,\mathrm{m}$	
Width of the slab	$\ell_y = 3.5\,\mathrm{m}$	
Thickness of the slab	$h = 0.27\,\mathrm{m}$	
Mass density of concrete	$\rho = 2375\,\mathrm{kg/m^3}$	
Dead load of the slab	$q = 6.29\,\mathrm{kPa}$	
Modulus of elasticity of concrete	$E = 41.6\,\mathrm{GPa}$	
Poisson's ratio of concrete	$\nu = 0.2$	[9]
Flexural rigidity of the slab	$K = 71.11\,\mathrm{MPa\,m^3}$	[9]
Coefficient of thermal expansion of concrete	$\alpha_T = 1.153 \times 10^{-5}/^\circ\mathrm{C}$	[28]

The structural analysis of the slab is decomposed into three load cases: (i) stresses due to dead load and curling, (ii) thermal eigenstresses, and (iii) stresses induced by the FWD load, see the following three sections.

2.4 Load case 1: Stresses at the slab's underside center due to dead load and curling

A structural model is used to compute stresses resulting from dead load and curling of the slab. Since it is unclear how to prescribe an eigencurvature in a multilayered simulation, the model is focused on the rectangular monolithic concrete slab which consists of the top concrete layer and the bottom concrete layer. The slab is modeled as a Kirchhoff plate, see Tab. 2.5 for its geometric dimensions and flexural rigidity.

The slab is modeled to be resting on a Winkler foundation [31], while the four lateral edges are idealized as free surfaces, see [19] for a similar approach. The dead load of the slab is a uniform vertical force per area and amounts to $q = 6.29\,\mathrm{kPa}$, see Tab. 2.5. The modulus of subgrade reaction k_s is unknown. Therefore, a sensitivity analysis is performed, i.e. k_s is set equal to $100\,\mathrm{MPa/m}$, $150\,\mathrm{MPa/m}$, $200\,\mathrm{MPa/m}$, and $250\,\mathrm{MPa/m}$, respectively.

The slab is subjected to a spatially uniform eigencurvature. In agreement with the values of the eigencurvature found during the FWD tests, see Tab. 2.4, eight values of κ^e are investigated. They range from $-5 \times 10^{-4}/\mathrm{m}$ to $+2 \times 10^{-4}/\mathrm{m}$, with a step size of $1 \times 10^{-4}/\mathrm{m}$. Under a negative eigencurvature, the corners of the slab are pressed downward, while its center may lift off from the Winkler foundation. Under a positive eigencurvature, the center of the slab is pressed downward, while its corners may lift off from the Winkler foundation.

The region of the concrete slab, which lifts off from the Winkler foundation, is a priori unknown. The nonlinear contact problem is solved iteratively and automatically using the FE software RFEM version 5.31.01 [10]. To this end, the midplane of the slab is discretized by means of 7000

quadratic Finite Elements of type "Kirchhoff bending theory", with a side length of 5 cm. The FE mesh consists of 7171 nodes.

In every single FE simulation, one specific value of the modulus of subgrade reaction is combined with one specific value of the eigencurvature. This results in a total of 32 numerical simulations.

The results of the FE simulations underline that the absolute value of the largest principal normal stress at the slab's underside center increases with (i) increasing absolute value of the eigencurvature and (ii) with increasing modulus of subgrade reaction, see Fig. 2.3. It is tensile in case of a negative eigencurvature, and it is compressive in case of a positive eigencurvature.

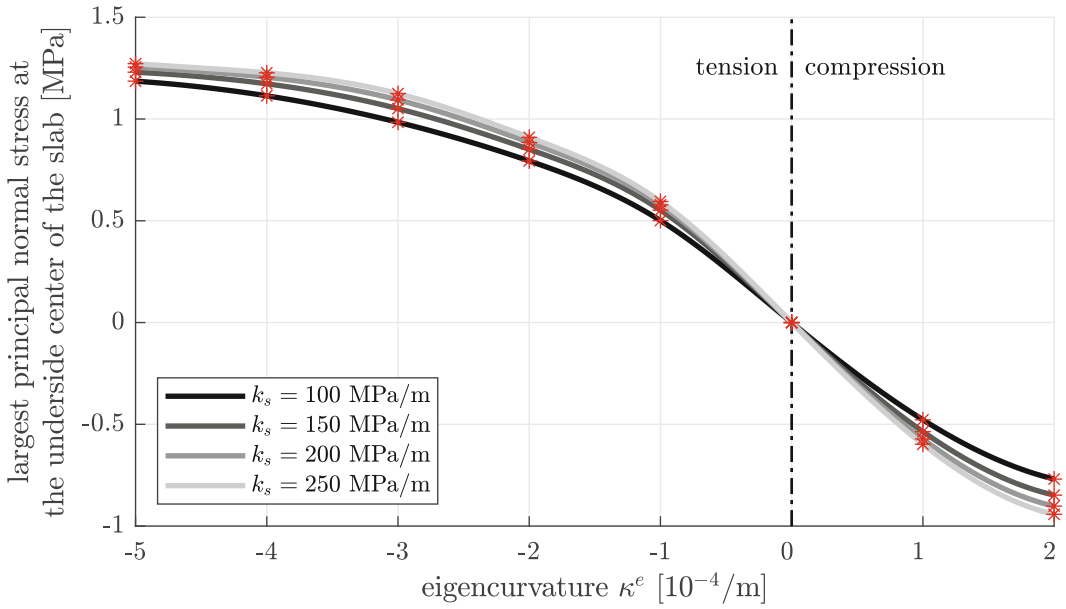

Fig. 2.3: Results from structural analysis of concrete slab "A10": largest principle normal stress at the slab's underside center, resulting from dead load and curling, for different values of the modulus of subgrade reaction k_s, as a function of the eigencurvature of the slab: markers illustrate results from nonlinear FE simulations, solid graphs are splines interpolating between the markers.

The maximum tensile stress due to dead load and curling, activated at the slab's underside center immediately before the 19 FWD tests, is found as follows. The largest negative eigencurvature according to Tab. 2.4, i.e. $\kappa^e = -4.90 \times 10^{-4}$/m, is marked on the abscissa of Fig. 2.3, and the corresponding tensile stresses are quantified. They range from 1.18 MPa for $k_s = 100$ MPa/m, to 1.27 MPa for $k_s = 250$ MPa/m, see Tab. 2.6. These results underline that the uncertainty regarding the modulus of subgrade reaction has a rather moderate influence on the estimation of the tensile stresses due to dead load and curling, activated at the slab's underside center immediately before FWD testing.

Tab. 2.6: Results from structural analysis of concrete slab "A10" at the time instants of FWD testing: largest principal normal stress at the slab's underside center, resulting from dead load and curling, for different values of the modulus of subgrade reaction k_s: stress values obtained by evaluating the splines of Fig. 2.3 for the eigencurvature values listed in Tab. 2.4.

	stresses [MPa] obtained with moduli of subgrade reaction of:			
Time/Date	$k_s = 100\,\mathrm{MPa/m}$	$k_s = 150\,\mathrm{MPa/m}$	$k_s = 200\,\mathrm{MPa/m}$	$k_s = 250\,\mathrm{MPa/m}$
13h13	1.17	1.21	1.24	1.26
14h03	1.18	1.23	1.25	1.27
15h09	1.17	1.22	1.24	1.26
16h11	1.00	1.06	1.11	1.14
17h28	0.82	0.88	0.91	0.94
18h08	0.77	0.83	0.86	0.89
19h20	0.50	0.55	0.58	0.59
20h33	0.07	0.08	0.08	0.08
21h22	−0.26	−0.29	−0.30	−0.32
07h35	−0.60	−0.67	−0.71	−0.75
09h05	−0.24	−0.27	−0.29	−0.30
10h03	0.12	0.13	0.14	0.15
12h44	0.88	0.94	0.98	1.01
13h39	1.06	1.13	1.17	1.19
Jul 2021	0.68	0.74	0.77	0.79
Sep 2021	0.60	0.66	0.68	0.70
Oct 2021	0.41	0.45	0.47	0.49
Jan 2022	−0.04	−0.04	−0.05	−0.05
Mar 2022	−0.12	−0.14	−0.15	−0.15

2.5 Load case 2: Thermal eigenstresses of concrete at the slab's underside

The self-equilibrated thermal eigenstresses of concrete are independent of the modulus of subgrade reaction and reads as [19]

$$\sigma_{eigen}(z,t) = -\frac{E}{1-\nu}\left\{\alpha_T\left[T(z,t) - T_{ref}\right] - \varepsilon^e(t) - \kappa^e(t)\,z\right\}, \tag{2.4}$$

where E denotes the modulus of elasticity of concrete, ν denotes the Poisson's ratio of concrete, $\varepsilon^e(t)$ denotes the eigenstretch of the midplane of the slab, at time t, which is defined as [19]

$$\varepsilon^e(t) = \frac{1}{h}\int_{-\frac{h}{2}}^{+\frac{h}{2}} \alpha_T\left[T(z,t) - T_{ref}\right]\,\mathrm{d}z\,, \tag{2.5}$$

and $\kappa^e(t)$ denotes the eigencurvature of the slab at time t, see Eq. (2.2). Insertion of $T(z,t)$ according to Eq. (2.1) into Eq. (2.5) yields

$$\varepsilon^e(t) = \frac{\alpha_T}{12}\left[12\,A_0(t) + A_2(t) - 12\,T_{ref}\right]. \tag{2.6}$$

Insertion of $T(z,t)$ according to Eq. (2.1), $\kappa^e(t)$ according to Eq. (2.3), and $\varepsilon^e(t)$ according to Eq. (2.6) into Eq. (2.4), and evaluation of the resulting expression for $z = h/2$ yields the following result for the thermal eigenstresses of concrete at the slab's underside:

$$\sigma_{eigen}(z{=}h/2,t) = -\frac{E\,\alpha_T\,A_2(t)}{6\,(1-\nu)}\,. \tag{2.7}$$

The thermal eigenstresses of concrete at the slab's underside, which prevailed during the 19 FWD tests, are computed by means of Eq. (2.7) from the measured temperatures listed in Tab. 2.3 and the concrete properties listed in Tab. 2.5. The values of the eigenstress of concrete range from −0.62 MPa at 13h13 on Sep 13 to +1.27 MPa at 16h11 on Sep 13, see Tab. 2.7.

Tab. 2.7: Results from structural analysis of concrete slab "A10" at the time instants of FWD testing: thermal eigenstress of concrete at the underside of the slab, $\sigma_{eigen}(z{=}h/2,t)$, according to Eq. (2.7) after fitting the temperature data T_5, T_6, T_7, and T_{surf} from Tab. 2.3 by means of the quadratic polynomial defined in Eq. (2.1), see also Tab. 2.5 for values of E, α_T, and ν.

Time/Date	$\sigma_{eigen}(z{=}h/2,t)$ [MPa]
13h13	−0.62
14h03	−0.29
15h09	0.21
16h11	1.27
17h28	0.93
18h08	0.85
19h20	0.70
20h33	0.82
21h22	0.93
07h35	0.25
09h05	−0.11
10h03	−0.42
12h44	−0.40
13h39	−0.58
Jul 2021	−0.39
Sep 2021	−0.59
Oct 2021	−0.24
Jan 2022	−0.12
Mar 2022	−0.13

When illustrating the thermal eigenstresses of concrete as a function of the thermal eigencurvature of the slab, a non-trivial correlation is obtained, see Fig. 2.4. The 14 data points corresponding to the tests conducted from 13h13 on Sep 13 to 13h39 on Sep 14 form a type of hysteretic loop that progresses in clockwise direction. The 5 data points referring to the tests performed from Jul 2021 to Mar 2022 are close to the bottom-right part of this hysteretic loop, see blue markers in Fig. 2.4. These results underline the following characteristic daily cycle: In the morning and early afternoon, during the heating phase of the slab, i.e. when heat is transported from the surface of the slab into its volume, the thermal eigenstress of concrete at the slab's underside is compressive and virtually constant at some −0.5 MPa, while the eigencurvature of the slab decreases progressively. The turnaround from compressive to tensile eigenstress of

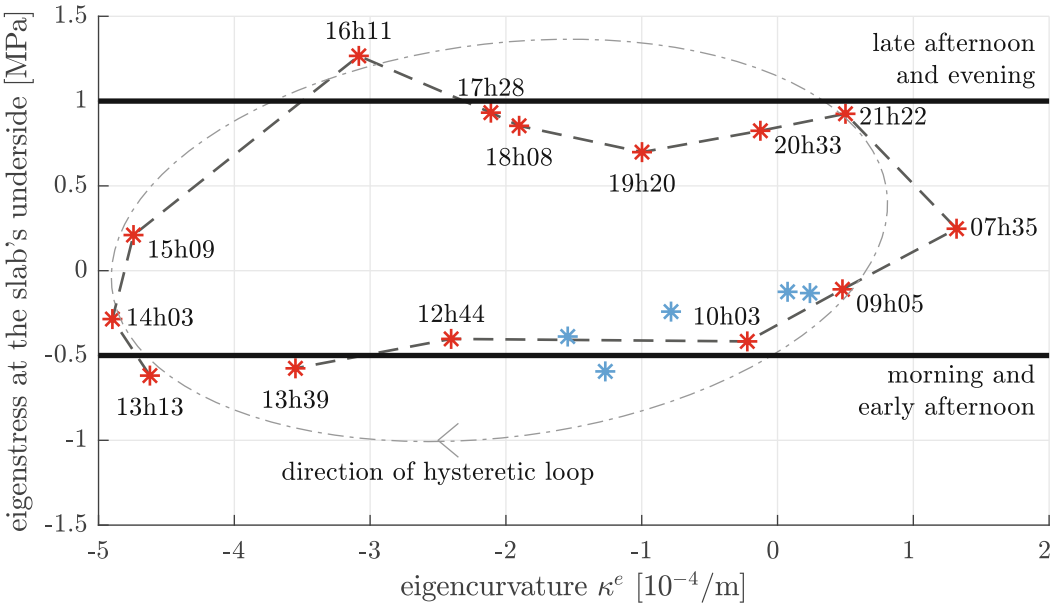

Fig. 2.4: Results from structural analysis of concrete slab "A10": thermal eigenstress of concrete at the slab's underside as a function of the thermal eigencurvature of the slab: markers illustrate values from Tabs. 2.4 and 2.7, the solid graphs illustrate approximations used for further analysis.

concrete takes place in the afternoon, within two to three hours, during which the eigencurvature of the slab is virtually constant and equal to the day's extreme value. In the later afternoon and evening, during the cooling phase of the slab, i.e. when heat is transported from the volume of the slab to its surface, the thermal eigenstress of concrete at the slab's underside is tensile and fluctuates around some 1.0 MPa, while the eigencurvature of the slab increases progressively. The turnaround from tensile to compressive eigenstress of concrete takes place in the night, during which the eigencurvature of the slab is slightly positive. It is concluded that the eigenstresses of concrete at the slab's underside can be approximated as being equal to (i) −0.5 MPa during the morning and early afternoon, and (ii) 1.0 MPa in the later afternoon and evening, see Fig. 2.4.

2.6 Load case 3: Stresses at the slab's underside center due to FWD testing

Deflections induced during FWD testing are also referred to as the "deflection basin". The latter delineates the disparity between the state of the concrete pavement slab prior to and under the action of the FWD load. In the following, a structural model is used to replicate the pointwisely measured deflection basin.

The structural model is focused on the monolithic concrete pavement slab, consisting of the top concrete layer and the bottom concrete layer. It is described by the Cartesian x, y, z-coordinate system of Fig. 2.1. The slab is modeled as a thin Kirchhoff plate [18], resting on a Winkler foundation [31]. The latter is extended by a uniform subgrade stress, in order to ensure that the simulations are capable of reproducing the measured deflections accurately, see [7] for details. Thus, the field equation of the boundary value problem at hand reads as

$$K\,\Delta\Delta w(x,y) + k\,w(x,y) - p_{aux} = p(x,y)\,, \tag{2.8}$$

where K denotes the flexural rigidity of the slab, see Tab. 2.5, $\Delta\Delta = \frac{\partial^4}{\partial x^4} + 2\,\frac{\partial^4}{\partial x^2 \partial y^2} + \frac{\partial^4}{\partial y^2}$ denotes the bilaplacian operator, $w(x,y)$ denotes the deflection basin, k denotes the modulus of subgrade reaction, such that $k\,w(x,y)$ is the Winkler-foundation-related subgrade stress, p_{aux} denotes the additional uniform subgrade stress [7], and $p(x,y)$ denotes the FWD load. It is equal to the maximum force exerted by the falling weight, 200 kN, introduced as a uniform load within a circular domain with radius $r_c = 0.15\,\mathrm{m}$:

$$p(x,y) = \begin{cases} \dfrac{200\,\mathrm{kN}}{r_c^2\,\pi} & \ldots \quad \sqrt{x^2+y^2} \le r_c\,, \\ 0 & \ldots \quad \sqrt{x^2+y^2} > r_c\,. \end{cases} \tag{2.9}$$

The values of the modulus of subgrade reaction k and of the additional uniform subgrade stress p_{aux} will be optimized in order to best explain the pointwisely measured deflections.

The deflection basin $w(x,y)$ is represented by a two-dimensional Fourier series of deflection modes which are double symmetric with respect to the x- and y-axes [7, 18]

$$w(x,y) = \sum_{m=0}^{N_m} \sum_{n=0}^{N_n} C_{mn} \cos\left(\frac{m\pi x}{\ell_x}\right) \cos\left(\frac{n\pi y}{\ell_y}\right) \quad \text{for} \quad \begin{cases} m = 0, 1, 3, \ldots, N_m, \\ n = 0, 1, 3, \ldots, N_n, \end{cases} \tag{2.10}$$

where C_{mn} denotes the sought Fourier coefficients, ℓ_x and ℓ_y denote the length and width of the slab, see Tab. 2.5, while m and n refer to the number of cosine half-waves of the corresponding deflection mode in x- and y-direction, respectively. The cosines with even values of m and n are disregarded, because they are antimetric. The total number of deflections modes taken into account is equal to $(N_m + 3)(N_n + 3)/4$, noting that $N_m \ge 1$ and $N_n \ge 1$.

The objective of the structural model is to best replicate the pointwisely measured deflection basin of each individual FWD test. To this end, it is useful to simply prescribe homogeneous stress boundary conditions at all four lateral edges of the concrete slab, although the analyzed concrete slab is connected with its neighbors in driving direction through dowels, and to its left neighbor through tie bars, while only the right edge is a free surface [11]. Mathematically, the "free edge"-boundary conditions can be expressed in terms of the following components of the Cauchy stress tensor $\boldsymbol{\sigma}$:

$$\sigma_{xy} = \sigma_{yx} = 0 \quad \text{at} \quad \begin{cases} x = \pm\dfrac{\ell_x}{2}, & \forall y \in \left[-\dfrac{\ell_y}{2}, +\dfrac{\ell_y}{2}\right], \\ y = \pm\dfrac{\ell_y}{2}, & \forall x \in \left[-\dfrac{\ell_x}{2}, +\dfrac{\ell_x}{2}\right], \end{cases} \tag{2.11}$$

$$\sigma_{xx} = \sigma_{xz} = 0 \quad \text{at} \quad x = \pm\frac{\ell_x}{2}, \quad \forall y \in \left[-\frac{\ell_y}{2}, +\frac{\ell_y}{2}\right], \tag{2.12}$$

$$\sigma_{yy} = \sigma_{yz} = 0 \quad \text{at} \quad y = \pm\frac{\ell_y}{2}, \quad \forall x \in \left[-\frac{\ell_x}{2}, +\frac{\ell_x}{2}\right]. \tag{2.13}$$

Therefore, the stress resultants at the edges of the slab vanish. This refers to the bending moments per length m_{xx} and m_{yy}, the twisting moments per length $m_{xy} = m_{yx}$, and the shear

forces per length q_x and q_y at $x = \pm\ell_x/2$ and $y = \pm\ell_y/2$, respectively. Accordingly, the "free edge"-boundary conditions (2.11)–(2.13) are reformulated as [7, 18, 27]

$$m_{xx} = \int_{-\frac{h}{2}}^{+\frac{h}{2}} \sigma_{xx}\, z \,\mathrm{d}z = 0 \qquad \text{at} \qquad x = \pm\frac{\ell_x}{2}, \quad \forall y \in \left[-\frac{\ell_y}{2}, +\frac{\ell_y}{2}\right], \tag{2.14}$$

$$m_{yy} = \int_{-\frac{h}{2}}^{+\frac{h}{2}} \sigma_{yy}\, z \,\mathrm{d}z = 0 \qquad \text{at} \qquad y = \pm\frac{\ell_y}{2}, \quad \forall x \in \left[-\frac{\ell_x}{2}, +\frac{\ell_x}{2}\right], \tag{2.15}$$

$$m_{xy} = m_{yx} = \int_{-\frac{h}{2}}^{+\frac{h}{2}} \sigma_{xy}\, z \,\mathrm{d}z = 0 \qquad \text{at} \qquad \begin{cases} x = \pm\dfrac{\ell_x}{2}, & \forall y \in \left[-\dfrac{\ell_y}{2}, +\dfrac{\ell_y}{2}\right], \\ y = \pm\dfrac{\ell_y}{2}, & \forall x \in \left[-\dfrac{\ell_x}{2}, +\dfrac{\ell_x}{2}\right], \end{cases} \tag{2.16}$$

$$q_x = \int_{-\frac{h}{2}}^{+\frac{h}{2}} \sigma_{xz} \,\mathrm{d}z = 0 \qquad \text{at} \qquad x = \pm\frac{\ell_x}{2}, \quad \forall y \in \left[-\frac{\ell_y}{2}, +\frac{\ell_y}{2}\right], \tag{2.17}$$

$$q_y = \int_{-\frac{h}{2}}^{+\frac{h}{2}} \sigma_{yz} \,\mathrm{d}z = 0 \qquad \text{at} \qquad y = \pm\frac{\ell_y}{2}, \quad \forall x \in \left[-\frac{\ell_x}{2}, +\frac{\ell_x}{2}\right]. \tag{2.18}$$

The sought Fourier coefficients C_{mn} in Eq. (2.10) are computed from a set of algebraic equations. They are derived from the Principle of Virtual Power [16], utilizing the amendment by Höller et al. [18] of Vlasov's theory for thin elastic plates on elastic Winkler foundations [27]. Under consideration of the field equation (2.8) and the "free edge"-boundary conditions (2.14)–(2.18) the Principle of Virtual Power reads as

$$\begin{aligned} \mathcal{L}^{ext} + \mathcal{L}^{int} = + \int_{-\frac{\ell_x}{2}}^{+\frac{\ell_x}{2}} \int_{-\frac{\ell_y}{2}}^{+\frac{\ell_y}{2}} \left[K \left(\frac{\partial^4 w}{\partial x^4} + 2\,\frac{\partial^4 w}{\partial x^2 \partial y^2} + \frac{\partial^4 w}{\partial y^4} \right) + k\, w - p_{aux} - p \right] \hat{w} \,\mathrm{d}y \,\mathrm{d}x \\ - \int_{-\frac{\ell_y}{2}}^{+\frac{\ell_y}{2}} \left[m_{xx}\,\frac{\partial \hat{w}}{\partial x} + m_{xy}\,\frac{\partial \hat{w}}{\partial y} - q_x\,\hat{w} \right] \Bigg|_{x=-\frac{\ell_x}{2}}^{x=+\frac{\ell_x}{2}} \mathrm{d}y \\ - \int_{-\frac{\ell_x}{2}}^{+\frac{\ell_x}{2}} \left[m_{xy}\,\frac{\partial \hat{w}}{\partial x} + m_{yy}\,\frac{\partial \hat{w}}{\partial y} - q_y\,\hat{w} \right] \Bigg|_{y=-\frac{\ell_y}{2}}^{y=+\frac{\ell_y}{2}} \mathrm{d}x = 0\,, \end{aligned} \tag{2.19}$$

where $\hat{w}$ denotes a virtual velocity field. It is introduced through an Ansatz function that is similar to the real deflection basin, see Eq. (2.10). For explicit equations for the Fourier coefficients C_{mn} and further details see [18]. In order to ensure a well-converged solution, N_m and N_n in Eq. (2.10) are both set equal to 59, resulting in 961 deflection modes. The related convergence analysis is focused on stresses rather than deflections. Therefore, it will be presented later.

All 19 individual FWD tests, see Tab. 2.2, are analyzed using the above described structural model. For each test, the optimal values of the modulus of subgrade reaction k and of the

additional uniform subgrade stress p_{aux} are searched within the intervals $k \in [100, 1100]$ MPa/m and $p_{aux} \in [0, 100]$ kPa. The resolution of the search grid is set equal to 10 MPa/m and 1 kPa for k and p_{aux}, respectively. This results in a total of $101 \times 101 = 10{,}201$ simulations for each individual FWD test. The quality of reproduction of the pointwisely measured deflection basin is quantified by means of the root mean square difference between the measured deflections $w_i(x_i)$, see Tab. 2.2, and simulated deflections $w(k, p_{aux}; x_i, y=0)$ computed by means of Eqs. (2.10) and (2.19) for each individual FWD test:

$$RMSD(k, p_{aux}) = \sqrt{\frac{1}{N_g} \sum_{i=1}^{N_g} \Big[w(k, p_{aux}; x_i, y=0) - w_i(x_i) \Big]^2}, \tag{2.20}$$

where N_g denotes the number of geophones and x_i denotes the x-coordinates of each geophone. Given that the geophones are positioned along the x-axis, x_i is equal to r_i, where r_i denotes the radial distance from the center of the slab, see Tab. 2.2. The number of geophones amounts to $N_g = 9$ for the 14 tests conducted from 13h13 on Sep 13 to 13h39 on Sep 14 and to $N_g = 8$ for the remaining five tests.

Insight into the properties of the $RMSD$-function according to Eq. (2.20) is provided for the FWD test at 13h13 on Sep 13 in Fig. 2.5, see Fig. A.1(b) of Appendix A for all other tests. The

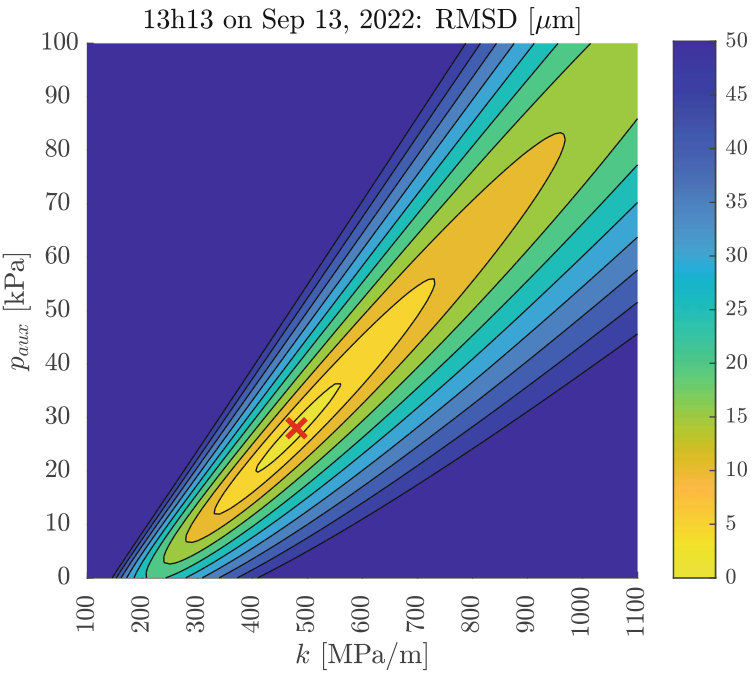

Fig. 2.5: Root mean square difference $RMSD$ according to Eq. (2.20) as a function of (i) the modulus of subgrade reaction k, see the abscissa, and (ii) the additional uniform subgrade stress p_{aux}, see the ordinate; for the FWD test at 13h13 on Sep 13, 2022: the red cross marks the pair of values $k = 480$ MPa/m and $p_{aux} = 28$ kPa at the minimum of the $RMSD$, where $RMSD = 3.02$ µm.

$RMSD$-function has a *single* minimum which is located *inside* the search intervals, see Fig. 2.5. This underlines that the identified values of k and p_{aux} represent a unique optimal solution of the underlying inverse problem.

The identified values of the modulus of subgrade reaction range from 440 MPa/m to 910 MPa/m, those of the additional uniform subgrade stress range from 26 kPa to 56 kPa, see Tab. 2.8. They increase with increasing value of thermal eigencurvature of the slab, see Figs. 2.6 and 2.7.

Tab. 2.8: Results from structural analysis of concrete slab "A10": optimal values of (i) the modulus of subgrade reaction k, and (ii) the additional uniform subgrade stress p_{aux}, and corresponding minimum of the root mean square difference according to Eq. (2.20), quantifying the difference between measured deflections listed in Tab. 2.2 and simulated deflections according to Eq. (2.10); for all 19 FWD tests.

Time/Date	k [MPa/m]	p_{aux} [kPa]	$RMSD$ [µm]
13h13	480	28	3.02
14h03	450	26	3.01
15h09	440	26	3.35
16h11	460	26	2.54
17h28	480	26	3.26
18h08	540	32	2.89
19h20	610	36	3.44
20h33	680	40	3.74
21h22	750	45	3.76
07h35	910	56	4.08
09h05	900	56	4.22
10h03	840	52	3.74
12h44	600	37	3.38
13h39	510	30	2.84
Jul 2021	600	39	3.24
Sep 2021	650	40	4.45
Oct 2021	670	38	4.12
Jan 2022	710	41	4.62
Mar 2022	680	40	4.22

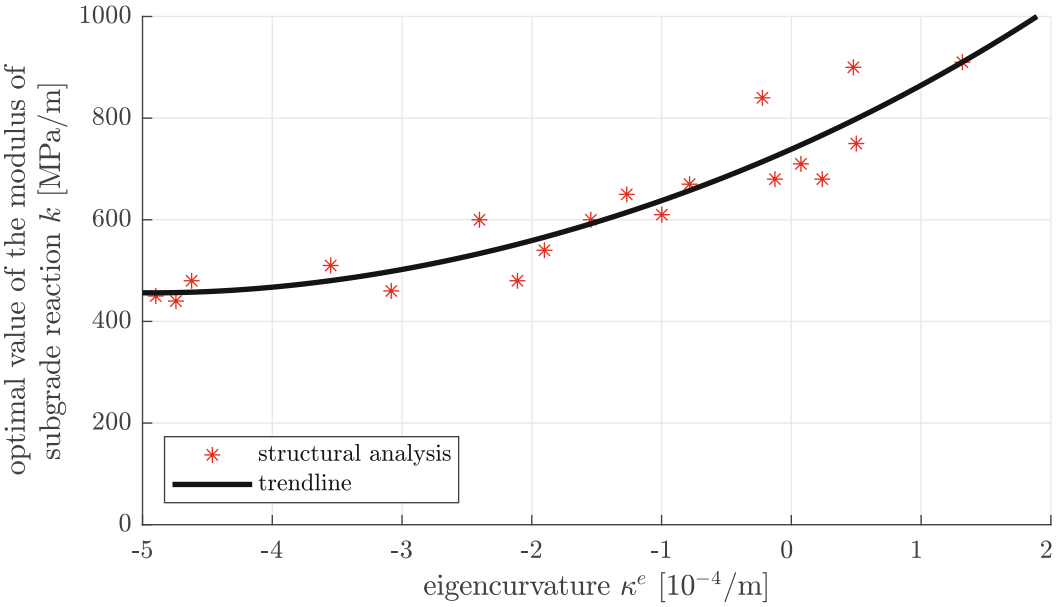

Fig. 2.6: Results from structural analysis of concrete slab "A10": optimal values of the modulus of subgrade reaction k as a function of the eigencurvature κ^e of the slab: markers illustrate values from Tabs. 2.4 and 2.8, the solid graph is a trendline.

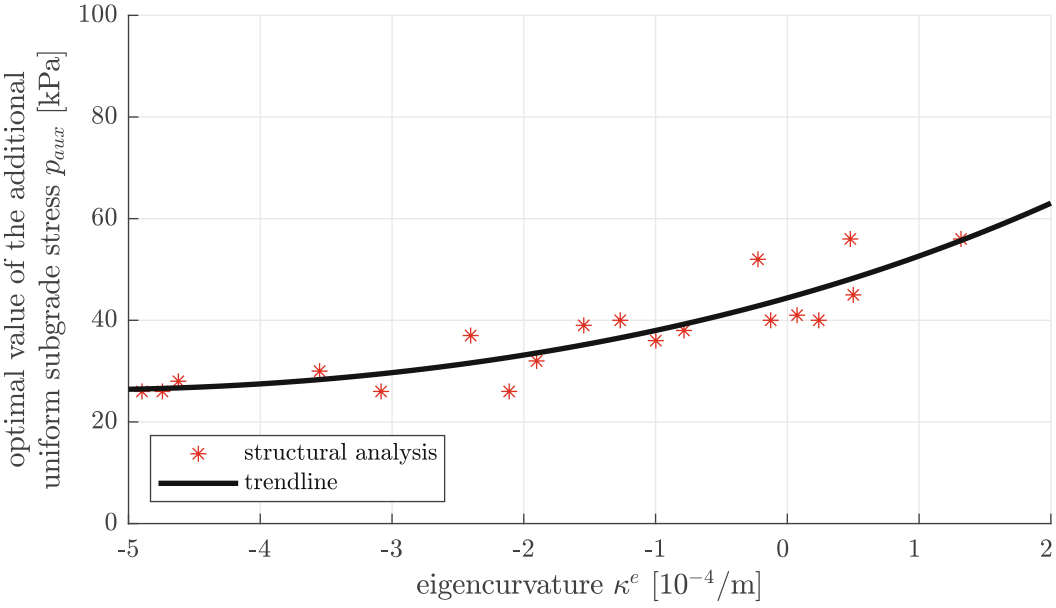

Fig. 2.7: Results from structural analysis of concrete slab "A10": optimal values of the additional uniform subgrade stress p_{aux} as a function of the eigencurvature κ^e of the slab: markers illustrate values from Tabs. 2.4 and 2.8, the solid graph is a trendline.

The corresponding values of the $RMSD$ according to Eq. (2.20) range from 2.54 µm to 4.62 µm, see Tab. 2.8. The achieved $RMSD$-values are satisfactory small in comparison with the measured deflections. The measured deflections are also qualitatively replicated in a satisfactory way, see Fig. 2.8 for the FWD test at 13h13 on Sep 13 and Fig. A.1(c) of Appendix A for all other tests.

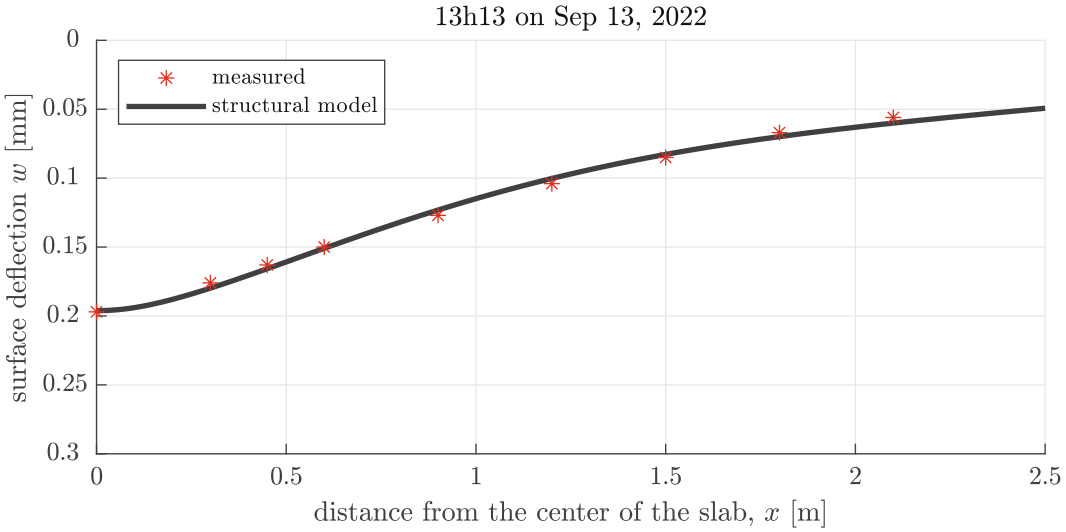

Fig. 2.8: Maximum deflections induced by central FWD testing at 13h13 on Sep 13, 2022 on the curled concrete slab "A10": markers illustrate measured deflections listed in Tab. 2.2, the solid graph illustrates the computed deflection basin, i.e. the solution of Eqs. (2.8) and (2.9) according to Eq. (2.10), see Tab. 2.8 for the corresponding optimal values of the modulus of subgrade reaction k and the additional uniform subgrade stress p_{aux} to be used in Eq. (2.8).

Since the structural simulations accurately reproduce the pointwisely measured deflections, the simulation results are well suited for quantification of the stresses resulting from the FWD load. The normal stresses σ_{xx} and σ_{yy} within the slab follow from the bending moments per length as

$$\sigma_{xx}(x,y,z) = \frac{m_{xx}(x,y)}{h^3/12}\, z, \tag{2.21}$$

and

$$\sigma_{yy}(x,y,z) = \frac{m_{yy}(x,y)}{h^3/12}\, z. \tag{2.22}$$

The bending moments per length m_{xx} and m_{yy}, in turn, follow from inserting the deflection basin according to Eq. (2.10) into the moment-curvature relations as

$$\begin{aligned} m_{xx}(x,y) &= -K\left[\frac{\partial^2 w}{\partial x^2} + \nu\,\frac{\partial^2 w}{\partial y^2}\right] \\ &= \frac{K\,\pi^2}{\ell_x^2\,\ell_y^2}\sum_{m=0}^{N_m}\sum_{n=0}^{N_n} C_{mn}\left(\ell_y^2\,m^2 + \nu\,\ell_x^2\,n^2\right)\cos\left(\frac{m\pi x}{\ell_x}\right)\cos\left(\frac{n\pi y}{\ell_y}\right), \end{aligned} \tag{2.23}$$

and

$$m_{yy}(x,y) = -K\left[\frac{\partial^2 w}{\partial y^2} + \nu\,\frac{\partial^2 w}{\partial x^2}\right]$$
$$= \frac{K\,\pi^2}{\ell_x^2\,\ell_y^2}\sum_{m=0}^{N_m}\sum_{n=0}^{N_n} C_{mn}\left(\ell_x^2\,n^2 + \nu\,\ell_y^2\,m^2\right)\cos\left(\frac{m\pi x}{\ell_x}\right)\cos\left(\frac{n\pi y}{\ell_y}\right). \tag{2.24}$$

Eqs. (2.23) and (2.24) underline that the functions of the bending moments per length are double symmetric with respect to the x- and y-axes. The largest bending moments are induced at the center of the slab, see exemplarily Fig. 2.9 for the FWD test at 13h13 on Sep 13 and Fig. A.1 of Appendix A for all other tests. The largest tensile stresses occur at the center of the slab

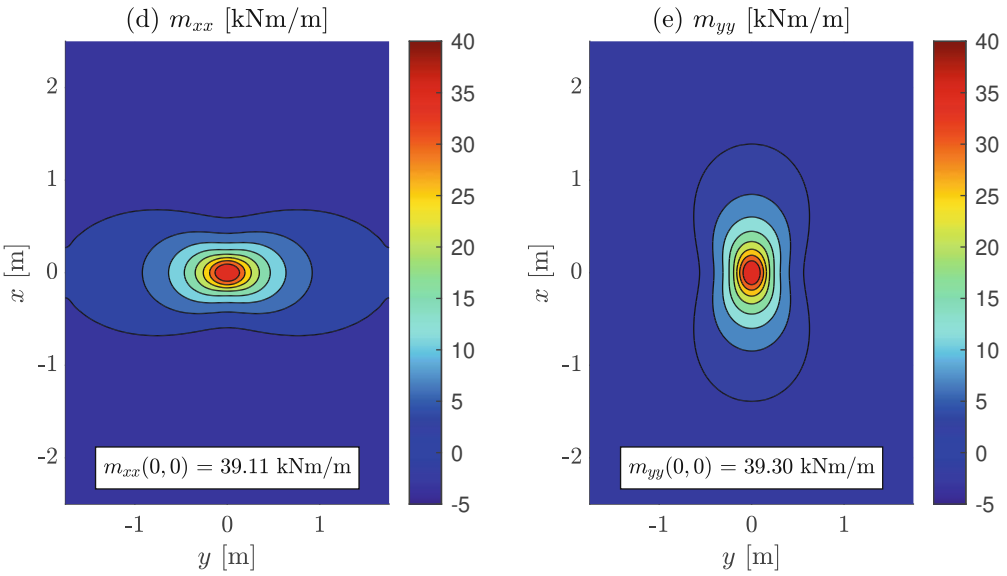

Fig. 2.9: Results from structural analysis of concrete slab "A10": bending moments per length: (a) m_{xx}, and (b) m_{yy}, for the FWD test at 13h13 on Sep 13, 2022 computed according to Eqs. (2.23) and (2.24), respectively.

$(x = y = 0)$ at its bottom surface $(z = +h/2)$. Specifying Eqs. (2.23) and (2.24) for $x = y = 0$ and inserting the resulting expressions together with $z = +h/2$ into Eqs. (2.21) and (2.22), yields the tensile stresses induced by the FWD load at the slab's underside center:

$$\max\sigma_{xx} = \frac{6\,K\,\pi^2}{h^2\,\ell_x^2\,\ell_y^2}\sum_{m=0}^{N_m}\sum_{n=0}^{N_n} C_{mn}\left(\ell_y^2\,m^2 + \nu\,\ell_x^2\,n^2\right), \tag{2.25}$$

and

$$\max\sigma_{yy} = \frac{6\,K\,\pi^2}{h^2\,\ell_x^2\,\ell_y^2}\sum_{m=0}^{N_m}\sum_{n=0}^{N_n} C_{mn}\left(\ell_x^2\,n^2 + \nu\,\ell_y^2\,m^2\right). \tag{2.26}$$

The tensile stresses at the slab's underside center according to Eqs. (2.25) and (2.26), computed for all 19 individual FWD tests, range from 2.96 MPa to 3.27 MPa, see Tab. 2.9. When illustrating them as a function of the thermal eigencurvature of the concrete slab, it is found that the stresses increase moderately with decreasing eigencurvature, see Fig 2.10.

Tab. 2.9: Results from structural analysis of concrete slab "A10": principal normal stresses $\max \sigma_{xx}$ and $\max \sigma_{yy}$ at the slab's underside center, resulting from central FWD testing on the curled slab, computed according to Eqs. (2.25) and (2.26); for all 19 FWD tests.

Time/Date	$\max \sigma_{xx}$ [MPa]	$\max \sigma_{yy}$ [MPa]
13h13	3.22	3.23
14h03	3.25	3.26
15h09	3.26	3.27
16h11	3.24	3.25
17h28	3.22	3.23
18h08	3.17	3.18
19h20	3.12	3.13
20h33	3.08	3.09
21h22	3.04	3.05
07h35	2.96	2.97
09h05	2.97	2.97
10h03	2.99	3.00
12h44	3.13	3.14
13h39	3.19	3.21
Jul 2021	3.13	3.14
Sep 2021	3.10	3.11
Oct 2021	3.08	3.09
Jan 2022	3.06	3.07
Mar 2022	3.08	3.09

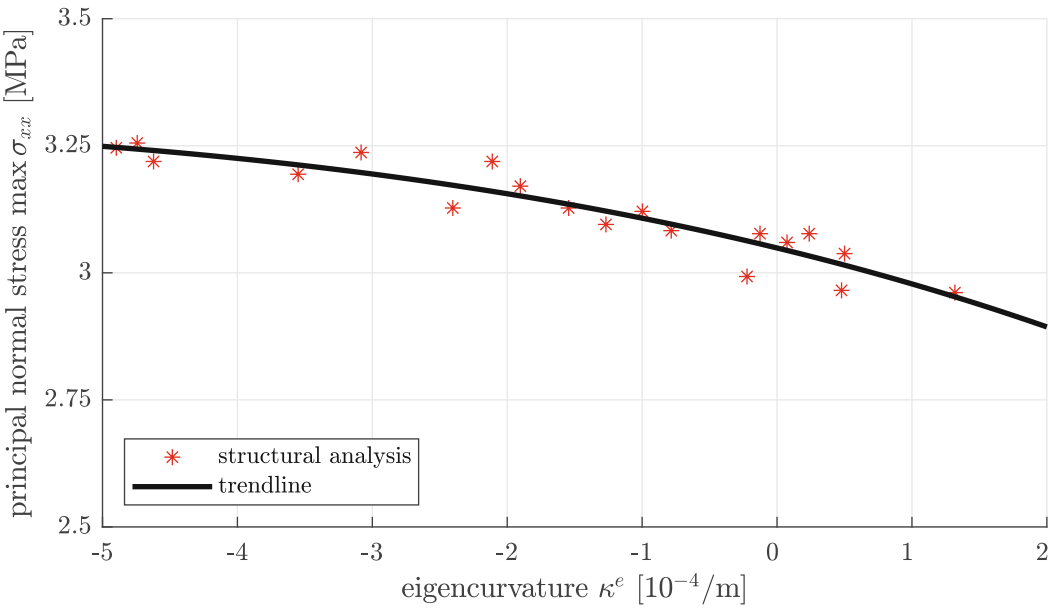

Fig. 2.10: Results from structural analysis of concrete slab "A10": principal normal stresses $\max \sigma_{xx}$ at the slab's underside center, resulting from central FWD testing on the curled slab, as a function of the eigencurvature κ^e of the slab: markers illustrate values from Tabs. 2.4 and 2.9, the solid graph is a trendline.

A convergence analysis regarding the number of deflection modes in the representation of the deflection basin, see Eq. (2.10), is performed in order to demonstrate the reliability of the quantified stresses. Notably, the stresses converge slower than the deflections, because the stresses are proportional to second spatial derivatives of the deflections, see Eqs. (2.21) to (2.24). Therefore, the convergence analysis is focused on the largest tensile stress $\max \sigma_{xx}$ at the slab's underside center, see Eq. (2.25). The structural analysis is repeated for many different values of the summation limits in Eq. (2.25), whereby N_n is always set equal to N_m. The results underline that increasing the number of Fourier coefficients leads to values of $\max \sigma_{xx}$, which increase at first up to a maximum, then decrease, and finally converge to a quasi-stable value, see Fig. 2.11. A reasonable trade-off between computational accuracy and effort appears to be the structural model with 961 Fourier coefficients. Consequently, N_m and N_n were set equal to 59.

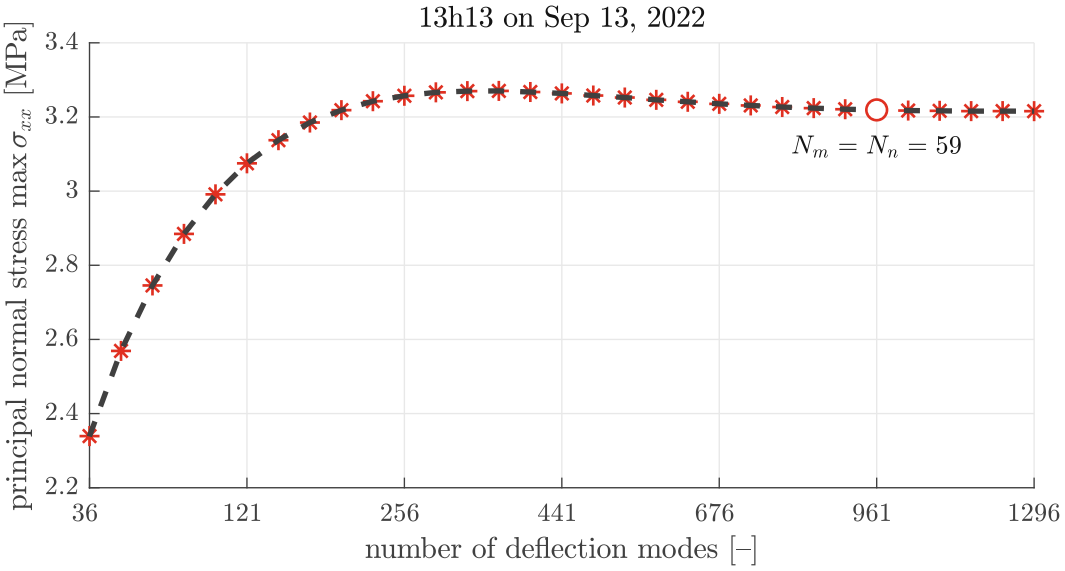

Fig. 2.11: Convergence analysis regarding the largest principal normal stress at the slab's underside center, resulting from FWD testing on the curled slab at 13h13 on Sep 13, 2022: $\max \sigma_{xx}$ according to Eq. (2.10) as a function of the number of prescribed deflection modes.

2.7 Superposition of load cases 1, 2, and 3: Total stresses at the slab's underside center due to dead load, thermal loading, and FWD testing

The total principal tensile stresses at the slab's underside center are equal to the sum of the curling stresses of Fig. 2.3, see also Tab. 2.6, the thermal eigenstresses of concrete of Fig. 2.4, see also Tab. 2.7, and the stresses resulting from FWD testing of Fig. 2.10, see also Tab. 2.9. The total stresses in x-direction are larger than those in y-direction because the curling stresses in x-direction are larger than to those in y-direction, the eigenstresses of concrete in x-direction are equal to those in y-direction, and the FWD-induced stresses in x-direction are almost equal to those in y-direction, see Tab. 2.9. Summing up the corresponding stress values from Tabs. 2.6, 2.7, and 2.9 yields total tensile stresses which range from 2.61 MPa to 5.50 MPa for $k_s = 100$ MPa/m and from 2.46 MPa to 5.64 MPa for $k_s = 250$ MPa/m, see Tab. 2.10. Thus, the modulus of subgrade reaction has a rather moderate influence. The overall largest total tensile stress during

Tab. 2.10: Results from structural analysis of concrete slab "A10": total tensile stresses at the slab's underside center, resulting from dead load, thermal loading, and FWD testing, for different values of the modulus of subgrade reaction k_s: sum of stresses listed in Tabs. 2.6, 2.7, and 2.9.

Time/Date	total tensile stresses [MPa] obtained with moduli of subgrade reaction of:			
	$k_s = 100\,\mathrm{MPa/m}$	$k_s = 150\,\mathrm{MPa/m}$	$k_s = 200\,\mathrm{MPa/m}$	$k_s = 250\,\mathrm{MPa/m}$
13h13	3.77	3.81	3.84	3.86
14h03	4.14	4.19	4.21	4.23
15h09	4.64	4.69	4.71	4.73
16h11	5.50	5.57	5.61	5.64
17h28	4.97	5.03	5.06	5.09
18h08	4.80	4.85	4.89	4.91
19h20	4.32	4.37	4.40	4.41
20h33	3.97	3.98	3.98	3.98
21h22	3.71	3.68	3.66	3.65
07h35	2.61	2.54	2.50	2.46
09h05	2.61	2.58	2.56	2.55
10h03	2.70	2.71	2.72	2.72
12h44	3.60	3.66	3.70	3.73
13h39	3.68	3.75	3.79	3.81
Jul 2021	3.42	3.48	3.51	3.53
Sep 2021	3.10	3.16	3.19	3.21
Oct 2021	3.25	3.29	3.31	3.33
Jan 2022	2.90	2.89	2.89	2.89
Mar 2022	2.82	2.81	2.80	2.79

FWD testing occurred at the FWD test at 16h11 on Sep 13 when the corresponding thermal eigencurvature κ^e of the slab amounted to -3.08×10^{-4}/m. The overall smallest tensile stress corresponds to an eigencurvature of the slab of $+1.32 \times 10^{-4}$/m at the FWD test at 07h35 on Sep 14. When summing up the trendlines of Figs. 2.3, 2.4, and 2.10, it is found that total stresses increase nonlinearly with decreasing eigencurvature of the slab, see Fig. 2.12, whereby one set of trendlines is relevant for the morning and the early afternoon, while the second set is relevant for the late afternoon and evening.

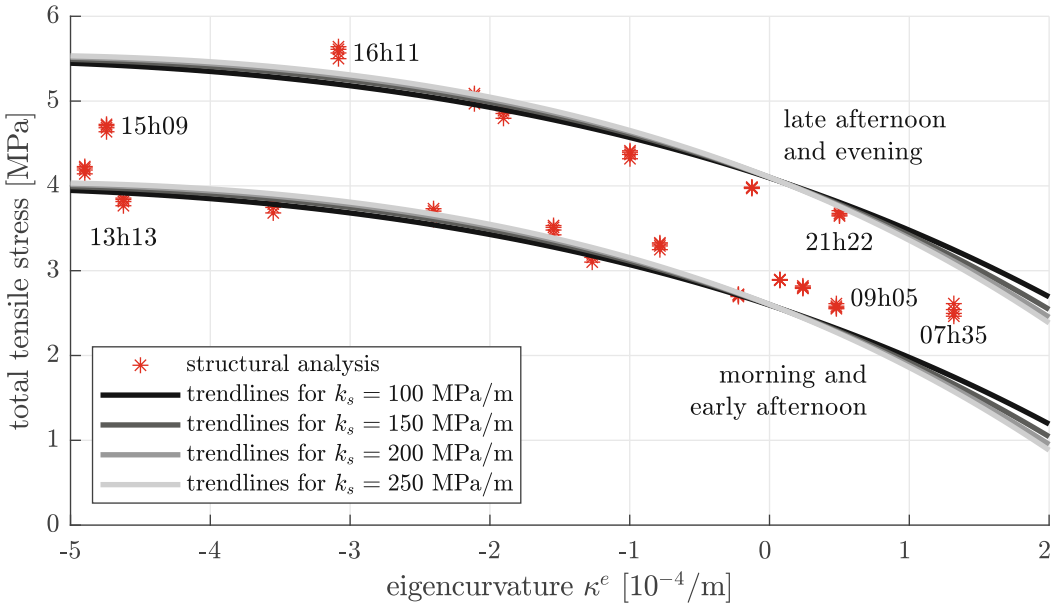

Fig. 2.12: Results from structural analysis of the concrete slab "A10": total tensile stresses at the slab's underside center, resulting from dead load, thermal loading, and FWD testing, for different values of the modulus of subgrade reaction k_s, as a function of the eigencurvature of the slab: markers illustrate values from Tab. 2.10, the solid graphs are trendlines representing the sum of the trendlines shown in Figs. 2.3, 2.4, and 2.10.

The analysis underscores that the largest tensile stresses activated by central FWD testing on a curled concrete slab are predictable, provided that the surface deflections are measured *and* the eigencurvature of the slab is known. Quantification of the eigencurvature of the slab based on temperature histories measured at the *surface* of a pavement slab is tackled next.

Chapter 3

Quantification of eigencurvature of concrete slabs from surface temperature history

Temperature-induced curling significantly contributes to the overall stresses in concrete pavement slabs, see Chapter 2. Quantification of temperature-induced slab curling requires knowledge of the temperature profile across its thickness. One method to obtain such profiles is to install temperature sensors at different depths, as shown at the field testing site described in Chapter 2. However, equipping concrete pavement slabs with embedded temperature sensors is expensive and, therefore, rather an exception. In regions requiring ice warning systems, in turn, surface temperature histories are measured at representative positions along highways. This provides the motivation to quantify the eigencurvature of concrete slabs from temperature histories measured at the slab's *surface*. To this end, the following two idealizations are made: (i) The slab is assumed to exhibit a uniform surface temperature across its top surface. (ii) The multilayered pavement structure and the subgrade underneath are assumed to have virtually the same thermal diffusivity as the concrete slab. Thus, one-dimensional heat conduction into an isotropic and homogeneous half-space will be simulated. This will provide access to the evolution of temperature profiles. The temporal development of the thermal eigencurvature of the slab will be derived from the simulated temperature profile in the uppermost region of the half-space, where the actual concrete pavement slab is located.

3.1 One-dimensional heat conduction into a half-space

An isotropic and homogeneous half-space is analyzed. Its surface is located at $\bar{z} = 0$. Its volume extends infinitely in the positive $\bar{z}$-direction, see Fig. 3.1(a).

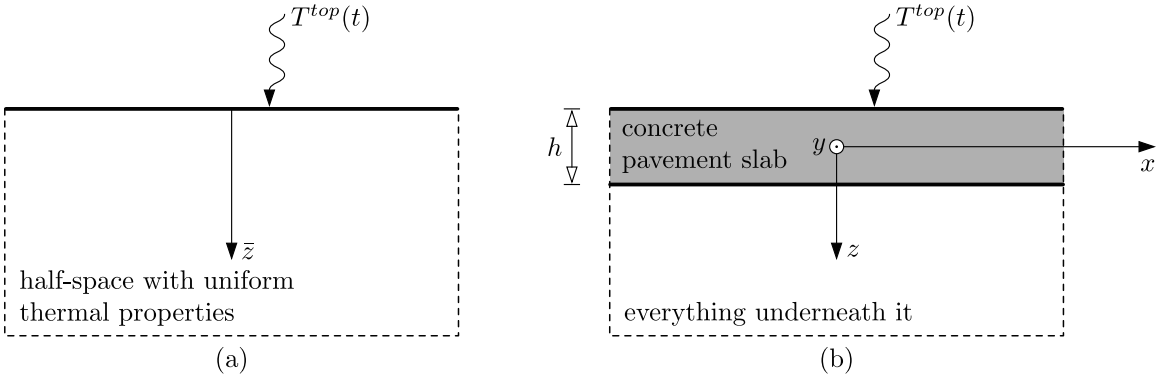

Fig. 3.1: (a) Isotropic and homogeneous half-space, described by coordinate $\bar{z}$ running normal to the surface of the half-space, with origin at the surface, and (b) concrete pavement slab of constant thickness h, described by a Cartesian x, y, z-coordinate system with origin at the center of the slab.

Heat conduction is an initial boundary value problem. The field equation is the heat equation. Regarding one-dimensional heat ingress in $\bar{z}$-direction, it reads as

$$\frac{\partial T}{\partial t} - a \frac{\partial^2 T}{\partial \bar{z}^2} = 0\,, \tag{3.1}$$

where $T = T(\bar{z}, t)$ denotes the temperature field at depth $\bar{z}$ and time t, while a denotes the thermal diffusivity. As initial condition at $t = t_1$, the temperature of the half-space is set equal to a uniform initial temperature value T_{ini}:

$$T(\bar{z}, t{=}t_1) = T_{ini}\,. \tag{3.2}$$

As boundary condition at the surface of the half-space, $\bar{z} = 0$, the measured surface temperature history is prescribed in a stepwise fashion:

$$T(\bar{z}{=}0, t) = T_{ini} + \sum_{i=1}^{N_T} \mathrm{H}(t - t_i)\, \Delta T_i^{top}\,, \tag{3.3}$$

where $\mathrm{H}(t - t_i)$ denotes the Heaviside function. It is equal to 0 for $t < t_i$ and equal to 1 for $t \geq t_i$. The N_T temperature increments ΔT_i^{top} in Eq. (3.3) follow from the measured surface temperature values, $T^{top}(t_i)$, as

$$\Delta T_i^{top} = \begin{cases} T^{top}(t_2) - T_{ini} & \text{for } i = 1\,, \\ T^{top}(t_{i+1}) - T^{top}(t_i) & \text{for } i \geq 2\,, \end{cases} \tag{3.4}$$

see also Fig. 3.2. The second boundary condition refers to the domain infinitely far away from the surface of the half-space, i.e. to $\bar{z} \to \infty$. This far-field boundary condition reads as

$$T(\bar{z} \to \infty, t) = T_{ini}\,. \tag{3.5}$$

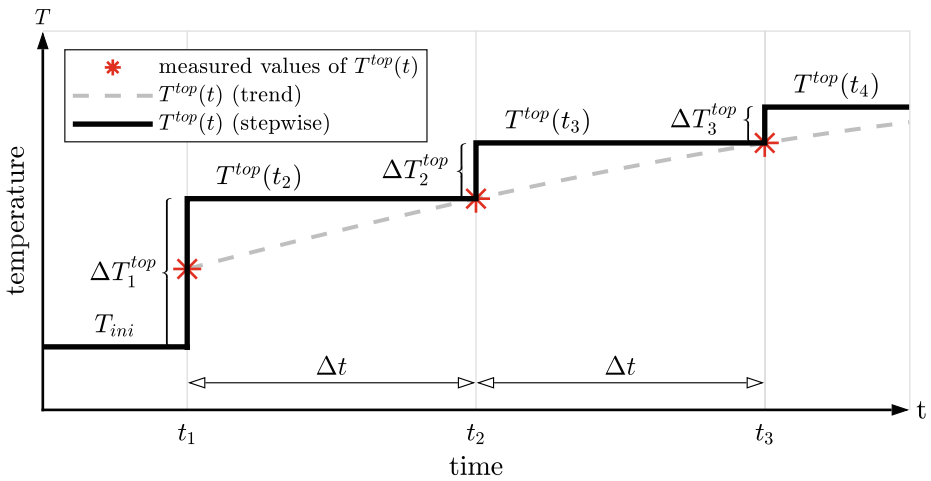

Fig. 3.2: Thermal boundary condition at the surface of the half-space: step-wise representation of measured surface temperature values.

The solution of the problem defined in Eqs. (3.1)–(3.5) reads as [5]

$$T(\bar{z},t) = T_{ini} + \sum_{i=1}^{N_T} \mathrm{H}(t-t_i)\,\Delta T_i^{top}\ \mathrm{erfc}\left(\frac{\bar{z}}{2\sqrt{a\,(t-t_i)}}\right), \tag{3.6}$$

where $\mathrm{erfc}(x) = 1 - \mathrm{erf}(x)$. Notably, $\mathrm{erf}(x) = \frac{2}{\sqrt{\pi}} \int_0^x \exp(-t^2)\,\mathrm{d}t$ denotes the error function, while $\mathrm{erfc}(x)$ denotes the complementary error function.

3.2 Quantification of eigencurvature based on the surface temperature history

As for quantification of the thermal eigencurvature of the concrete pavement slab, the Cartesian x, y, z-coordinate system of Fig. 3.1(b) is used. The relation between the slab-related z-coordinate and the half-space-related $\bar{z}$-coordinate reads as $\bar{z} = z + h/2$, where h denotes the thickness of the slab. Inserting this expression for $\bar{z}$ into Eq. (3.6) yields the temperature field as a function of z:

$$T(z,t) = T_{ini} + \sum_{i=1}^{N_T} \mathrm{H}(t-t_i)\,\Delta T_i^{top}\ \mathrm{erfc}\left(\frac{z+h/2}{2\sqrt{a\,(t-t_i)}}\right). \tag{3.7}$$

The thermal eigencurvature of a concrete pavement slab is, at any time t, equal to the first moment of the thermal eigenstrain distribution prevailing at that time [19], see Eq. (2.2). Thus, inserting Eq. (3.7) into Eq. (2.2) yields

$$\kappa^e(t) = \frac{12\,\alpha_T}{h^3} \sum_{i=1}^{N_T} \mathrm{H}(t-t_i)\,\Delta T_i^{top}\,a\,(t-t_i) \left[\mathrm{erf}\left(\frac{h}{2\sqrt{a\,(t-t_i)}}\right) - \frac{h}{\sqrt{\pi}\,\sqrt{a\,(t-t_i)}}\right]. \tag{3.8}$$

Neither T_{ini}, see Eq. (3.7), nor T_{ref}, see Eq. (2.2), show up explicitly in Eq. (3.8), because they are constant. Still, Eq. (3.8) depends implicitly on T_{ini}, since ΔT_1^{top} is a function of T_{ini}, see Eq. (3.4).

3.3 Exemplary validation based on data from a temperature-monitored field testing site

The performance of the presented approach for quantification of the eigencurvature is demonstrated by applying it to a concrete slab with quasi-continuous in situ temperature monitoring. It is located at kilometer 21 of the highway "A2 – Südautobahn" in Austria. The thickness of the slab amounts to $h = 0.25\,\mathrm{m}$. As for in situ temperature monitoring, the slab was equipped with four Pt100 temperature sensors, installed at positions $z_1 = -0.075\,\mathrm{m}$, $z_2 = -0.035\,\mathrm{m}$, $z_3 = 0.015\,\mathrm{m}$, and $z_4 = 0.065\,\mathrm{m}$. For more details see [19]. Hourly temperature measurements were taken from Sep 23, 2015, 00:00 to Oct 15, 2015, 24:00. Therefore, four temperatures were recorded at 552 instants of time. In order to increase the temporal resolution of the measurements, splines were used to interpolate every three minutes between measured temperatures, see [19] and Fig. 3.2. This results in 11,021 sets of four temperature values, see Fig 3.3.

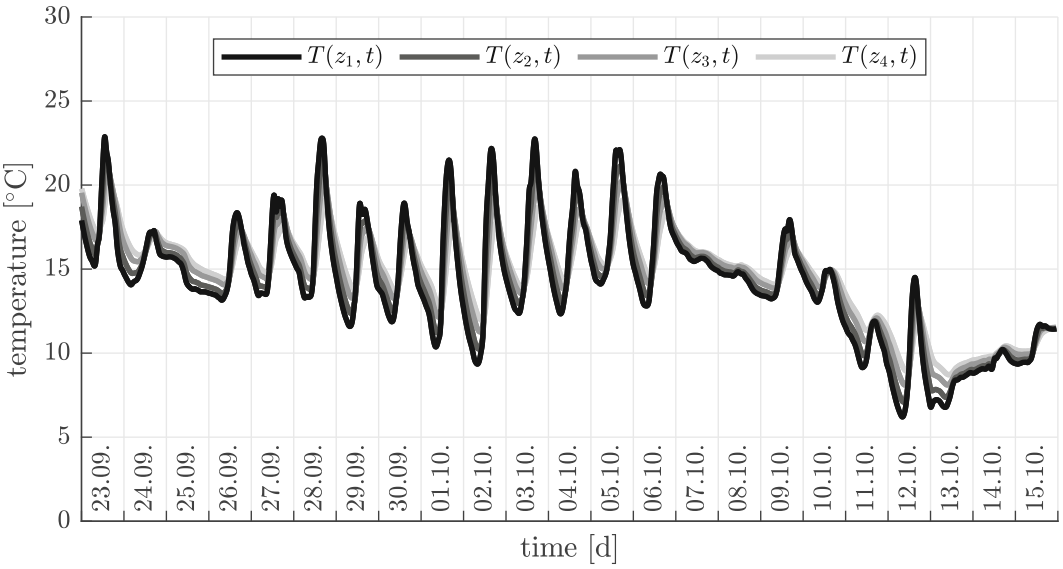

Fig. 3.3: Data from temperature monitoring at the field testing site of highway A2: temperatures measured by Pt100 sensors installed at specific depths of the concrete slab.

The temperature data of Fig. 3.3 allows for quantifying the evolution of the thermal eigencurvature of the concrete slab, as explained next. The temperature profile is fitted, at any time instant t of interest, by means of a quadratic polynomial, see Eq. (2.1), where $A_0(t)$, $A_1(t)$ and $A_2(t)$ are 11,021 sets of optimization coefficients. The thermal eigencurvature of the pavement slab at time t, is obtained by inserting the parabolic temperature field of Eq. (2.1) into Eq. (2.2), see Eq. (2.3) and Fig. 3.4. Notably, the parabolas of Eq. (2.1) were evaluated at $z = -h/2$ in order to determine the surface temperature evolution [19], see Fig. 3.5.

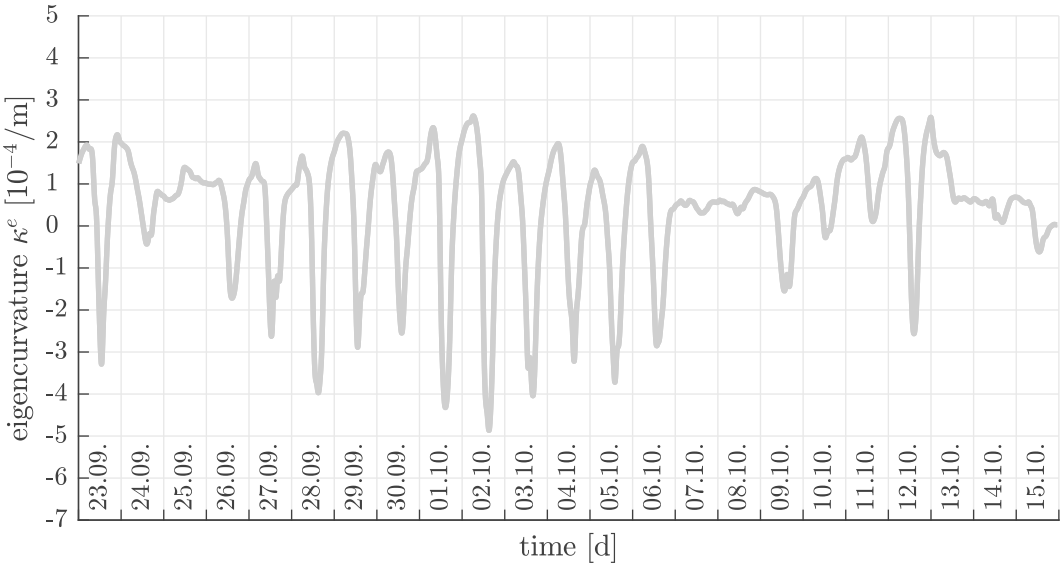

Fig. 3.4: Evolution of the eigencurvature of the concrete slab "A2": κ^e according to Eq. (2.3) after fitting the temperature data of Fig. 3.3 by means of the quadratic polynomial defined in Eq. (2.1).

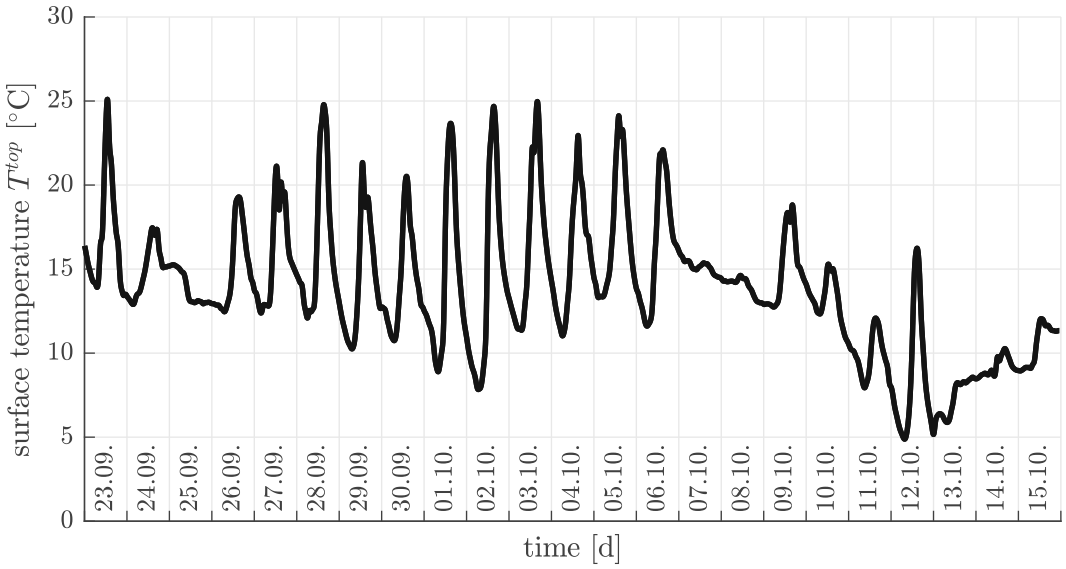

Fig. 3.5: Surface temperature evolution of the slab "A2", after [19].

In the remainder of this section, it is checked how well the eigencurvature evolution of Fig. 3.4, which was derived from temperature measurements *inside the bulk* of the concrete slab, can be computed by means of Eq. (3.8) from the *surface* temperature evolution of Fig. 3.5. The latter has a temporal resolution of three minutes and is prescribed in a stepwise fashion, see Eqs. (3.3) and (3.4). This yields 11,020 temperature steps. Thus, the summation index i in Eq. (3.8) runs from 1 to 11,020. The initial temperature T_{ini} of the half-space is set equal to 17 °C. The thermal diffusivity is taken from [19]: $a = 1.4 \times 10^{-6}\,\mathrm{m^2/s}$. The coefficient of thermal expansion is taken from [28]: $\alpha_T = 1.153 \times 10^{-5}/°\mathrm{C}$, see also Tab. 3.1. Inserting the described

Tab. 3.1: Thickness of the concrete slab "A2", and thermal properties of its concrete

Property	Value	Source
Thickness of the slab	$h = 0.25\,\mathrm{m}$	
Thermal diffusivity of the concrete	$a = 1.4 \times 10^{-6}\,\mathrm{m^2/s}$	[19]
Coefficient of thermal expansion of the concrete	$\alpha_T = 1.153 \times 10^{-5}/°\mathrm{C}$	[28]

quantities into Eq. (3.8) yields the evolution of the thermal eigencurvature of the slab as a function of the surface temperature history, see the black graph in Fig. 3.6. The starting value of the computed evolution of $\kappa^e(t)$ is equal to zero, because the numerical simulation starts with a *uniform* temperature field. With the progress of simulation time, $\kappa^e(t)$ computed from the surface temperature history according to Eq. (3.8) approaches $\kappa^e(t)$ derived from temperature evolutions measured at four different depths inside the slab according to Eq. (2.3), see Fig. 3.6. Both approaches yield virtually the same results from some seven days after the start of the observation period onward.

The quality of agreement after the described run-in phase is quantified by means of the root mean square difference ($RMSD$). It is calculated for the last 15 days of the observation period:

$$RMSD = \sqrt{\frac{1}{N}\sum_{i=1}^{N}\left[\kappa^e_{hss}(t_i) - \kappa^e_{par}(t_i)\right]^2}\,, \tag{3.9}$$

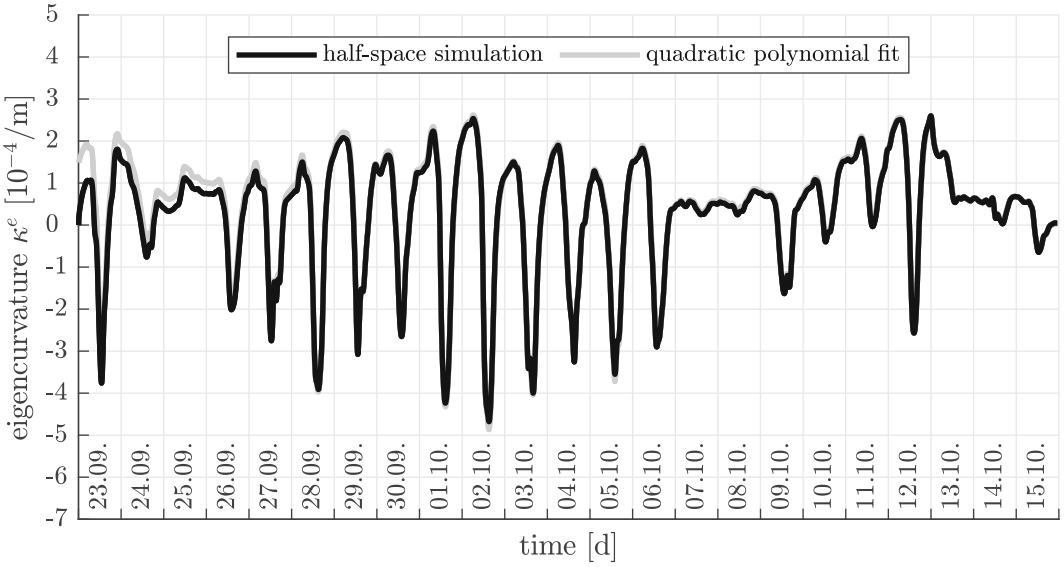

Fig. 3.6: Eigencurvature history of the slab "A2": comparison of (i) the evolution computed by means of Eq (3.8) from the *surface* temperature history of Fig. 3.5, see the black graph, and (ii) the evolution according to Fig. 3.4, computed by means of Eq. (2.3) after fitting the temperature data measured *inside* the slab, see Fig. 3.3, by means of the quadratic polynomial defined in Eq. (2.1), see the gray graph.

where κ^e_{hss} stands for κ^e according to the half-space simulation based on the surface temperature history, see Eq. (3.8), and κ^e_{par} stands for κ^e according to the parabolic fit of four temperatures measured inside the slab's volume, see Eq. (2.3). In addition, the functional argument "t_i" is used in Eq. (3.9) to denote $N = 7200$ specific values of thermal eigencurvatures at time t_i. The $RMSD$ according to Eq. (3.9) amounts to 6.41×10^{-6}/m and is two orders of magnitude smaller than the extreme values of the eigencurvature evolution, amounting to -4.68×10^{-4}/m and $+2.60 \times 10^{-4}$/m, respectively. This underlines that the eigencurvature of a slab can indeed be quantified reliably from the surface temperature history, provided that this history is known over a period of some seven days.

In the interest of computational efficiency for practical applications, we are left with quantifying (i) how much simulation time must have elapsed, until the eigencurvature according to Eq. (3.8) is reliable, and (ii) how large the time intervals between two subsequent time steps may be, without compromising the accuracy of Eq. (3.8) at the end of the run-in phase. These are the topics of the following two sections.

3.4 Minimum duration of the analyzed temperature history

To quantify how much simulation time must have elapsed before the thermal eigencurvature of the slab according to Eq. (3.8) becomes reliable, the computation of $\kappa^e(t)$ according to Eq. (3.8) is repeated six times, starting from six different time instants, i.e. t_1 in Eq. (3.4) is set equal to 00:00 a.m. on Sep 23, Sep 26, Sep 29, Oct 2, Oct 5, and Oct 8, respectively. Disregarding surface temperature values recorded before these start time instants, the evolution of $\kappa^e(t)$ is computed six times. Reliability indicators are computed by subtracting the reference values $\kappa^e(t)$ according to Eq. (2.3) from the six computed evolutions of $\kappa^e(t)$ according to Eq. (3.8). The resulting differences, $\Delta\kappa^e(t) = \kappa^e_{hss}(t) - \kappa^e_{par}(t)$, are plotted as a function of the time elapsed since the

start time instant: $t_{sim} = t - t_1$, see Fig. 3.7. The six graphs in Fig. 3.7 underline that once some seven days have elapsed since the starting time instant, the reliability of $\kappa^e(t)$ according to Eq. (3.8) is sufficiently large for engineering purposes. Consequently, surface temperature measurements should be recorded over a period of at least seven days.

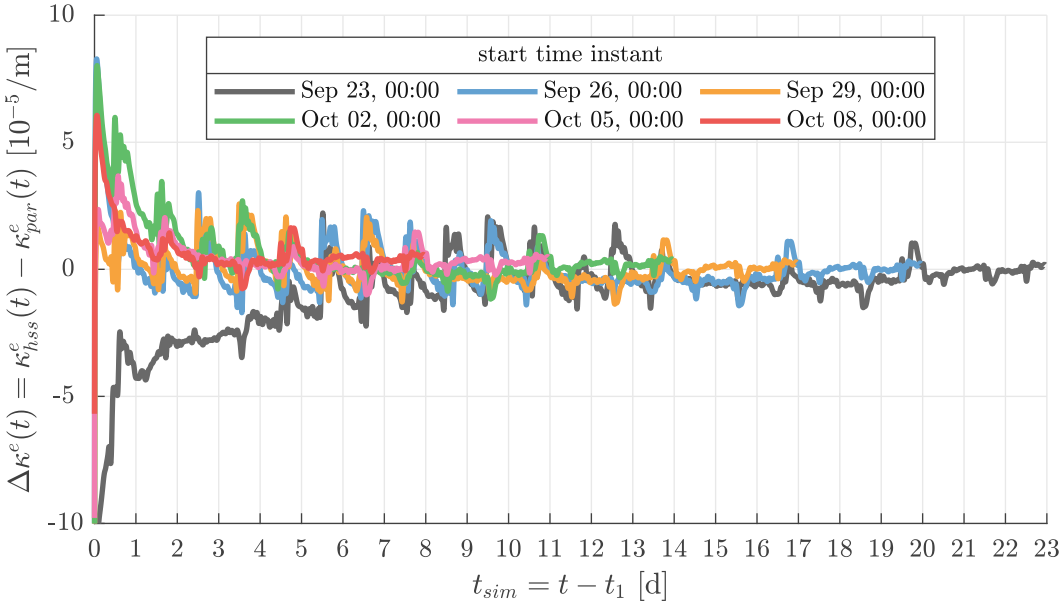

Fig. 3.7: Evolution of the differences between $\kappa^e(t)$ according to Eq. (3.8), computed with six different start time instants, and the reference values $\kappa^e(t)$ according to Eq. (2.3).

3.5 Maximum time step size

To quantify how large the time intervals between two subsequently prescribed surface temperature increments may be, without compromising the accuracy at the end of the run-in phase, the computation of $\kappa^e(t)$ according to Eq. (3.8) is repeated six times. For each computation, the time step size Δt according to Fig. 3.2 is set equal to 3 min, 6 min, 15 min, 30 min, 60 min, and 120 min, respectively. Surface temperature values in between are disregarded. As accuracy indicator, the root mean square difference ($RMSD$) according to Eq. (3.9) is calculated for the last 15 days of the observation period and for each time step size, see Fig. 3.8(a). With increasing time increments, the $RMSD$ increases, see Fig. 3.8(a), while the computation time decreases, see Fig. 3.8(b). A time step size of 15 minutes appears to be an optimal trade-off between computation accuracy and time. Therefore, it is recommended that surface temperature measurements are recorded every 15 minutes.

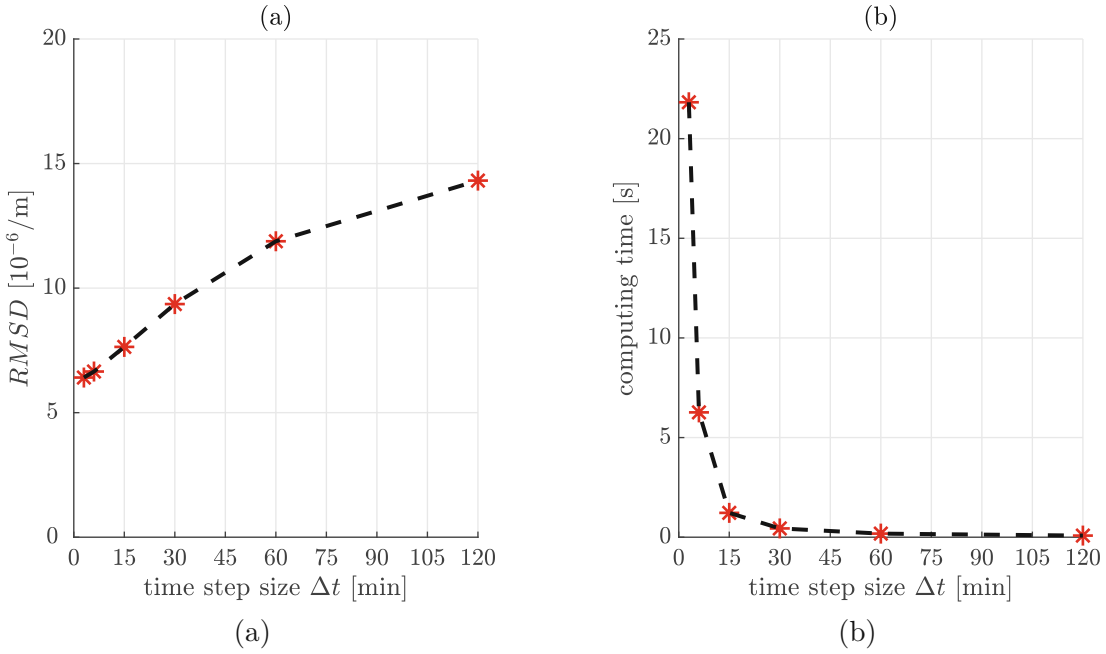

Fig. 3.8: Sensitivity analysis regarding maximum time step size: (a) root mean square difference ($RMSD$) between $\kappa^e(t)$ according to Eq. (3.8) and the reference values $\kappa^e(t)$ according to Eq. (2.3) for time step sizes of 3 min, 6 min, 15 min, 30 min, 60 min, and 120 min and (b) corresponding computing time for each time step size; the computing times have been achieved with Matlab version R2024b [24] running on a *AMD Ryzen 3700X 8-Core Processor* with 32 GB of RAM.

Chapter 4

Transition from research to practical application

4.1 Engineering approach to tensile stresses from FWD testing

Quantification of tensile stresses resulting from central FWD testing on a curled slab, as described in Section 2.6, requires the optimization of the modulus of subgrade reaction and of the additional uniform subgrade stress. Therefore, many structural simulations are to be performed. This represents a considerable computational effort.

As a remedy, an alternative engineering approach is elaborated herein. It limits the required input quantities to the thickness of the slab, h, its flexural rigidity, K, Poisson's ratio of concrete, ν, and the two innermost maximum surface deflections measured during FWD testing, i.e. w_1 measured at the center of the falling weight ($r_1 = 0.0\,\mathrm{m}$) and w_2 measured in the radial distance r_2 from the center of the falling weight. A radial symmetric parabola is used to approximate the deflection basin between the first and the second geophone:

$$w_{par}(r) \approx w_1 + (w_2 - w_1) \times \left(\frac{r}{r_2}\right)^2, \tag{4.1}$$

where w_1, w_2, and r_2 are taken from Tab. 2.2. The parabola agrees reasonably well with the deflection basin derived from the structural model, see Fig. 4.1. This provides the motivation for

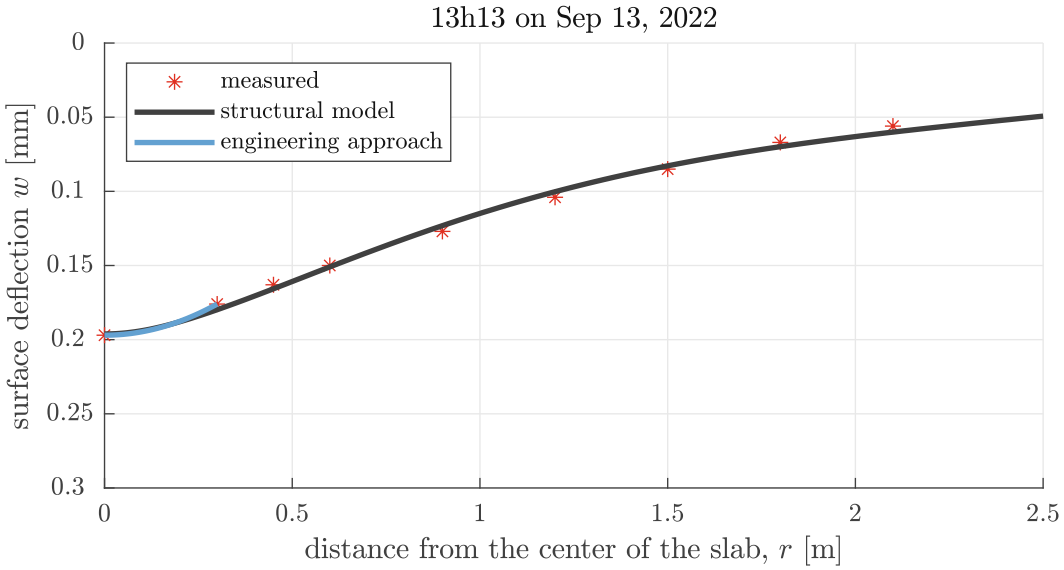

Fig. 4.1: Maximum deflections induced by central FWD testing at 13h13 on Sep 13, 2022 on the curled concrete slab "A10": the markers illustrate measured deflections, see Tab. 2.2, the black solid graph refers to the structural model of Section 2.6, and the blue solid graph refers to the engineering approach, see Eq. (4.1).

computing stresses from the approximated deflection basin according to Eq. (4.1). To this end, the radial coordinate r is replaced in Eq. (4.1) by the Cartesian coordinates x and y: Inserting $r = \sqrt{x^2 + y^2}$ into Eq. (4.1), substituting the resulting expression for $w_{par}(x, y)$ into the first line of Eq. (2.23), inserting the resulting expression for the constant bending moment m_{xx} into Eq. (2.21), and evaluating the obtained expression for $\sigma_{xx}(z)$ at the the slab's underside, i.e. at $z = h/2$, yields the tensile stress at the slab's underside center simply as

$$\sigma_{xx}^{par} \approx \frac{12\,K\,(1+\nu)\,(w_1 - w_2)}{(h\,r_2)^2}\,. \tag{4.2}$$

Evaluation of Eq. (4.2) for values of K, ν, and h from Tab. 2.5 and values of w_1, w_2, and r_2 from Tab. 2.2 yields tensile stresses ranging from 2.97 MPa to 4.21 MPa, see Tab. 4.1. These

Tab. 4.1: Stresses at the underside center of slab "A10", resulting from central FWD testing on the curled slab: comparison of stresses σ_{xx}^{par} computed by means of the engineering approach, see Eqs. (4.1) and (4.2), with stresses $\max \sigma_{xx}$ computed by means of the structural model of Section 2.6, see Eq. (2.25); for all 19 FWD tests.

Time/Date	σ_{xx}^{par} [MPa]	$\max \sigma_{xx}$ [MPa]
13h13	3.28	3.22
14h03	3.43	3.25
15h09	4.21	3.26
16h11	3.75	3.24
17h28	4.06	3.22
18h08	3.59	3.17
19h20	3.75	3.12
20h33	3.28	3.08
21h22	3.43	3.04
07h35	3.43	2.96
09h05	3.12	2.97
10h03	3.12	2.99
12h44	3.28	3.13
13h39	3.59	3.19
Jul 2021	2.97	3.13
Sep 2021	2.97	3.10
Oct 2021	2.97	3.08
Jan 2022	2.97	3.06
Mar 2022	2.97	3.08

engineering-approach-related stresses agree well with (or slightly overestimate) the stresses computed by means of the structural model of Section 2.6, see Fig. 4.2. Thus, the engineering model is very useful. The slight overestimation results in a conservative approach.

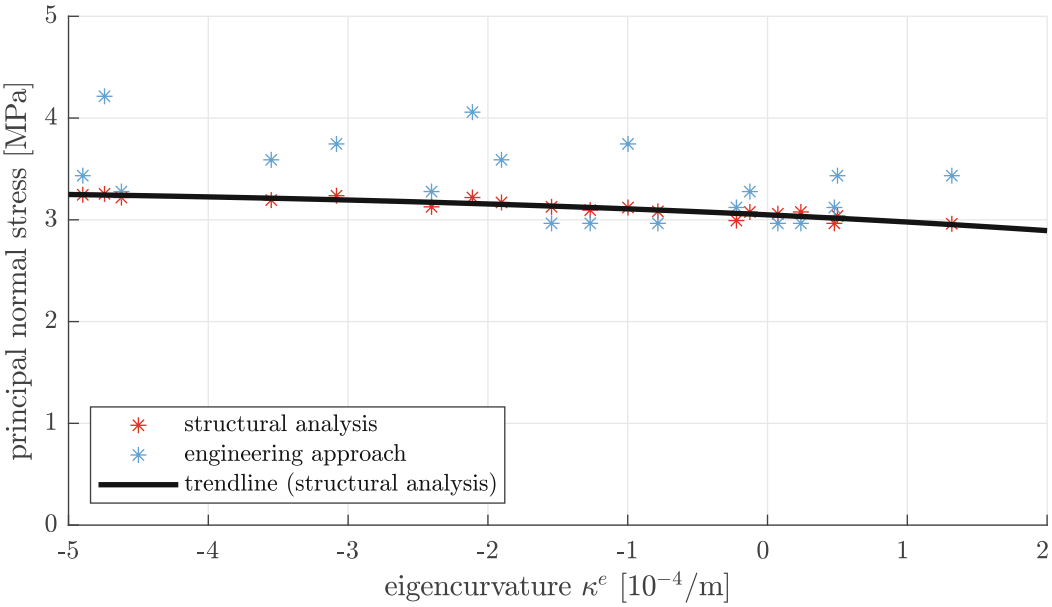

Fig. 4.2: Stresses at the underside center of slab "A10", resulting from central FWD testing on the curled slab, as a function of the eigencurvature of the slab: comparison of stresses σ_{xx}^{par} computed by means of the engineering approach, see Eqs. (4.1) and (4.2) as well as Tab. 4.1, with stresses $\max \sigma_{xx}$ computed by means of the structural model of Section 2.6, see Eq. (2.25) and Tabs. 2.4 and 2.9.

4.2 Tensile stresses resulting from traffic loads

The analyzed FWD tests were performed with a maximum load of 200 kN. However, the Equivalent Standard Axle Load (ESAL) used for pavement design in Austria amounts to 100 kN [15]. Therefore, the design wheel load is equal to 50 kN. This provides the motivation to discuss stresses resulting from the ESAL based on the here-quantified stresses referring to central FWD testing on the curled slab "A10".

A curling-free concrete slab ($\kappa^e = 0$) exhibits full-face contact with the adjacent layer of the pavement structure. In this case, stresses resulting from FWD testing can be quantified by means of multilayered simulations [9]. Accounting for non-destructive FWD testing, linear elastic material behavior is used in these simulations. The resulting linearity of the structural problem implies that all simulation results scale linearly with the intensity of the surface load. This includes the stresses. It is concluded that reducing the central surface load from the FWD force of 200 kN to the design wheel load of 50 kN decreases the tensile stresses at the slab's underside center from some 3.05 MPa, see $\kappa^e = 0$ in Fig. 2.10, to some 0.76 MPa, see $\kappa^e = 0$ in Fig. 4.3.

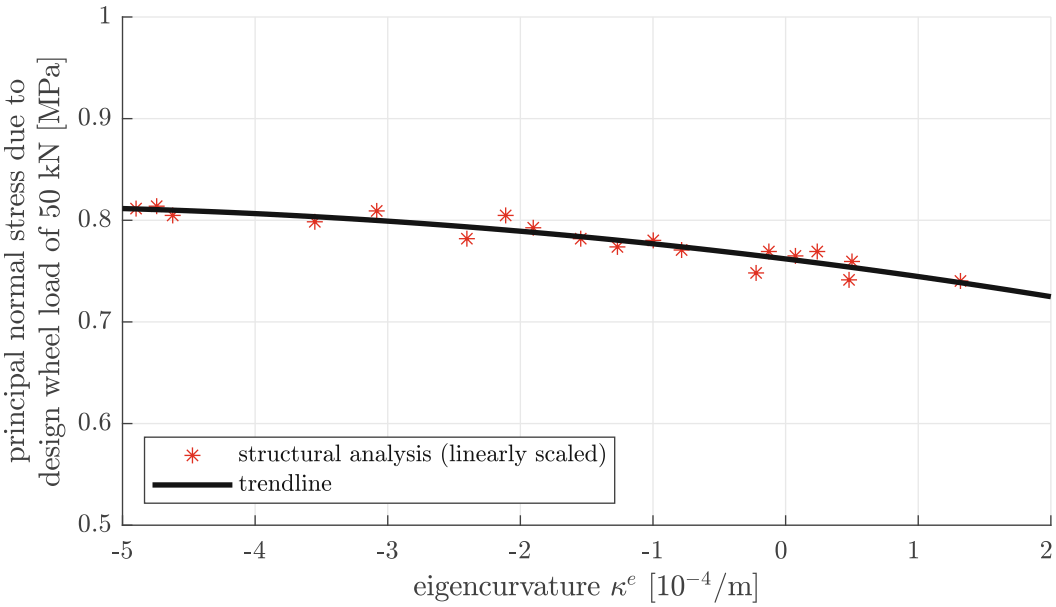

Fig. 4.3: Stresses at the underside center of slab "A10", resulting from a design wheel load of 50 kN running over the curled slab, as a function of the eigencurvature of the slab: markers illustrate values obtained by linearly scaling the results of the structural analysis with a FWD force of 200 kN, see Tab. 2.9, to the design wheel load of 50 kN, the solid graph is a trendline.

Stresses in a curled concrete slab are discussed next. FWD testing with a maximum load of 200 kN on the curled slab "A10" resulted in maximum tensile stresses which are virtually independent of the value of the eigencurvature of the slab, they increase from some 3.05 MPa obtained for $\kappa^e = 0$ by less than 7 % to some 3.25 MPa obtained for the in absolute terms largest thermal eigencurvature, $\kappa^e = -5 \times 10^{-4}$/m, see Fig. 2.10. Therefore, it is intuitive to assume, that stresses due to a central vertical loading scale linearly with the intensity of this loading for all values of the thermal eigencurvature, such that they can be quantified by dividing the stresses of Fig. 2.10 by the maximum FWD load of 200 kN and by multiplying the result with the intensity of the traffic load of interest. As for a traffic load of 50 kN, the estimated stresses range from some 0.7 MPa to 0.8 MPa, see Fig. 4.3.

The total tensile stresses related to traffic running over a curled slab are obtained again by superimposing the stresses due to dead load and curling (Fig. 2.3), thermal eigenstresses of concrete (Fig. 2.4), and stresses due to the traffic load (Fig. 4.3), see Fig. 4.4. The total stresses increase in the morning up to some 1.5 MPa. During the afternoon, they increase quickly from some 1.5 MPa to some 3.0 MPa. During the later afternoon and evening, they decrease to some 1.0 MPa. During the night and in the earlier morning, the total stresses may be as small as 0.5 MPa, see the lowest markers in Fig. 4.4.

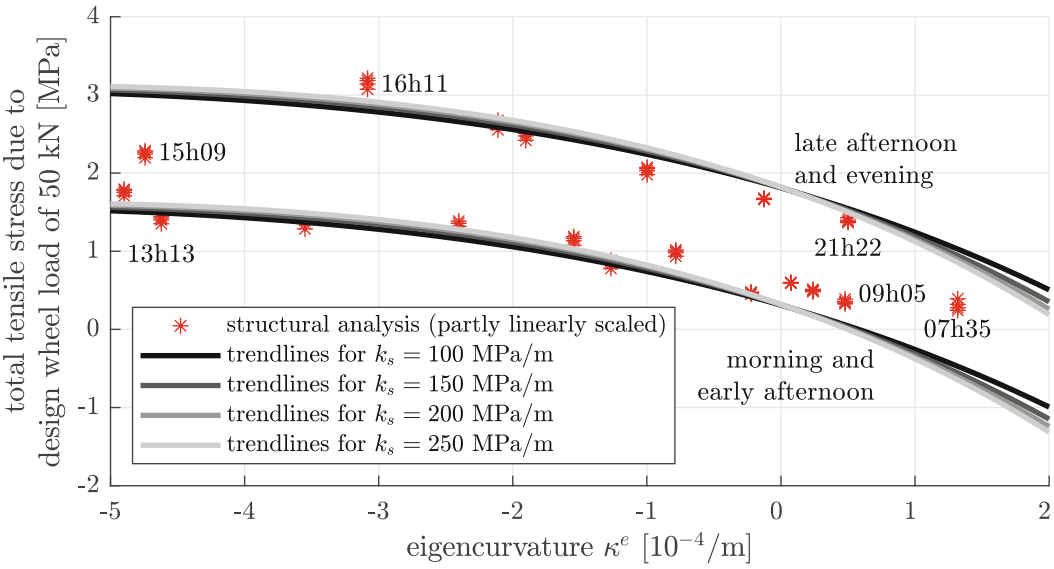

Fig. 4.4: Total stresses at the underside center of the concrete slab "A10" resulting from dead load, thermal loading, and a design wheel load of 50 kN running over the curled slab, for different values of the modulus of subgrade reaction k_s, as a function of the eigencurvature of the slab: markers illustrate values obtained by superimposing the marker values of Figs. 2.3, 2.4, and 4.3., the solid graphs are the superposition of the trendlines shown in these three figures.

4.3 Implications for highway operation and pavement design

The same design vehicle running over the same slab will induce tensile stresses of 0.5 MPa during the night and in the early morning, but tensile stresses of more than 3.0 MPa during the afternoon, see Fig. 4.4. This underlines that overloaded vehicles are particularly harmful to pavement structures when running over slabs during periods of time in the afternoon, when relatively large values of the thermal eigencurvature of the slab are combined with large values of the thermal eigenstress of concrete.

In the future, highway operators can perform real-time quantitative monitoring of the eigencurvature evolution by using surface temperature measurements from ice warning systems as input for the model of Chapter 3. Thus, they can anticipate periods during which the traffic stresses will be particularly small or large. Then, it is recommended (i) to operate traffic control stations with truck weighing stations preferentially during time intervals with large tensile stresses, and (ii) to schedule exceptional heavy-vehicle traffic in the early morning, when both the thermal eigencurvature of the slab and the thermal eigenstress of concrete are particularly small.

Regarding pavement design, concrete fatigue is a decisive design criterion for rigid pavements, but the long-term exposure conditions are largely unknown. The results of the present thesis underline that traffic-induced tensile stresses experienced by concrete slabs are strongly influenced by the thermal eigencurvature of the slab and by the thermal eigenstresses of concrete. Thus, identification of realistic exposure conditions, i.e. of realistic histories of tensile stress circles, requires knowledge of (i) the volume, the composition, and the temporal distribution of the traffic loads, (ii) the eigencurvature history, and (iii) the eigenstresses. As regards point (i), the volume and temporal distribution of heavy traffic on Austrian highways is recorded at road toll stations [12]. Combining these data with representative distributions of truck types allows for the transition to distributions of corresponding axle loads, see e.g. [3]. As regards points (ii) and (iii), the model of Chapter 3 is very likely to play an important role in the future.

Chapter 5

Conclusions

The following conclusions are drawn from the here-performed analysis of central FWD testing at a well-instrumented field testing site:

- Surface deflections measured during central FWD tests correlate with the thermal eigencurvature of the concrete slab: the maximum measured deflections increase linearly with increasing absolute value of the negative eigencurvature. Thereby, the absolute value of the slope increases with increasing proximity to the center of the slab.

- Tensile stresses at the slab's underside center can be decomposed into three portions: stresses due to dead load and curling of the slab, self-equilibrated thermal eigenstresses of concrete, as well as stresses induced by FWD testing.

- To compute stresses resulting from dead load and curling, the slab was modeled as a thin Kirchhoff plate with traction-free edges, resting on a Winkler foundation. The plate was subjected to different values of uniform thermal eigencurvature. The principal stresses at the slab's underside center vanish in case of vanishing eigencurvature, they are tensile in case of negative eigencurvature, and they are compressive otherwise. The absolute values of the stresses increase with increasing absolute values of the eigencurvature. Virtually the same stresses were obtained for different values of the modulus of subgrade reaction in the here-investigated realistic interval from 100 MPa/m to 250 MPa/m.

- Thermal eigenstresses of concrete at the slab's underside were quantified analytically. During the course of one representative autumn day, the eigenstresses of concrete exhibit a non-trivial hysteretic correlation with the eigencurvature of the slab. In the morning and early afternoon, the eigenstresses are compressive and virtually constant, while the negative eigencurvature increases. Within two to three hours in the afternoon, the eigenstresses change from compressive to tensile, while the eigencurvature is virtually constant. In the late afternoon and evening, the eigenstresses are tensile and virtually constant, while the negative eigencurvature decreases. During the night, the eigenstresses change from tensile to compressive, while the eigencurvature is small.

- To compute tensile stresses resulting from the FWD testing, the slab was modeled as a thin Kirchhoff plate with traction-free edges, resting on a Winkler foundation extended by a uniform subgrade stress. The plate was subjected to the FWD load of 200 kN. To best replicate the test-specific deflections measured by the geophones, the values of both the modulus of subgrade reaction and the uniform additional subgrade stress were optimized. The test-specific optimal values correlate well with the test-specific values of the thermal eigencurvature of the slab. The FWD-induced tensile stresses at the slab's underside center depend only moderately on the value of the eigencurvature of the slab. For engineering purposes they can be set constant.

- An alternative engineering approach to tensile stresses resulting from the FWD testing consists of approximating the deflection basin in the immediate vicinity of the falling weight by means of a radial symmetric parabola running through the two innermost geophone-measured deflection values. The stresses are computed by means of constitutive relations of Kirchhoff's linear theory of thin plates. The engineering approach is useful and conservative, as it delivers stresses which are very close to or only slightly larger than the stresses computed from the structural model.

- The (total) tensile stresses at the underside center of a curled concrete slab which is subjected to central FWD testing are predictable, provided that the thermal eigencurvature of the concrete slab is known. They increase with increasing absolute value of the negative eigencurvature in the morning and the early afternoon, and they decrease with decreasing negative eigencurvature during the late afternoon and evening.

The following conclusions are drawn from the computation of thermal eigencurvature based on a known surface temperature history:

- Prescribing surface temperature steps as boundary condition for the simulation of one-dimensional heat ingress into an initially isothermal, homogeneous, and isotropic half-space which exhibits the thermal properties of concrete, allows for quantifying the temporal evolution of the temperature profile and, consequently, of the thermal eigencurvature of the concrete slab.

- The computed eigencurvature is reliable provided that (i) the analyzed surface temperature history is equal to or longer than seven days, and (ii) the temperature steps are prescribed in intervals of 15 minutes or less.

As regards practical pavement engineering, the results of the present study suggest the following conclusions:

- The same vehicle running over the same slab will induce up to six-times as large tensile stresses in the afternoon, when the slab exhibits a large negative eigencurvature and large thermal eigenstresses of concrete at its underside, compared to the stresses induced in the earlier morning, when the slab exhibits a small eigencurvature and small thermal eigenstresses of concrete at its underside.

- Real-time quantitative monitoring of the eigencurvature of concrete slabs is possible by using surface temperature measurements from ice warning systems as input for the thermo-mechanical model of Chapter 3.

- It is recommendable to operate traffic control stations with truck weighing stations preferentially during times when both the absolute value of the negative eigencurvature of the slab and the tensile eigenstresses of concrete at the slab's underside are particularly large.

- It is recommendable to schedule exceptional heavy-vehicle traffic during times when both the eigencurvature of the slab and the eigenstresses of concrete at the slab's underside are particularly small.

- It will be interesting to combine the data from eigencurvature-monitoring with corresponding data describing axle load distributions, in order to determine realistic histories of tensile stress cycles for the fatigue assessment of existing concrete slabs and for the fatigue design of future pavement structures.

Finally, the limitations of the presented study are listed as follows:

- The first part of the study was limited to 19 FWD tests with maximum force of 200 kN on one field testing site. Additional FWD experiments with different maximum forces are desirable, in order to validate the stress scaling approach of Section 4.2.
- The second part of the study was limited to 23 days of temperature monitoring of another field testing site. The analysis of additional temperature monitoring data is desirable, in particular of data recorded during extreme weather events such as hail showers [28].
- As for the structural analysis and the computation of tensile stresses, the slab was idealized as a homogeneous plate. In the future, it will be interesting to account for different stiffnesses of the top concrete and the bottom concrete layers.
- The linear elastic simulations regarding the load case "dead load and curling" could not be validated herein, since no surface deflection measurements are available for a curled slab free of surface loading. Such data would allow for assessing the influence of dowels and tie bars as well as the influence of concrete creep on the stresses due to dead load and curling.

Appendices

Appendix A

Summary of structural analysis for all FWD tests

The following pages contain diagrams illustrating the results of the structural analysis for all 19 FWD tests performed. Each page is dedicated to one FWD test. The diagrams are organized at follows:

(a) Temperature profiles within the slab "A10" during FWD testing: markers illustrate measured temperature values T_5, T_6, T_7 and T_{surf} from Tab. 2.3, the solid graphs illustrate the best-fit quadratic polynomials according to Eq. (2.1).

(b) Root mean square differences $RMSD$ according to Eq. (2.20) as a function of (i) the modulus of subgrade reaction k, see the abscissa, and (ii) the additional uniform subgrade stress p_{aux}, see the ordinate the red crosses mark the pair of values k and p_{aux} at the minimum of the $RMSD$

(c) Maximum deflections induced by central FWD testing on the curled concrete slab "A10": markers illustrate measured deflections listed in Tab. 2.2, the solid grpahs illustrate the computed deflection basins, i.e. the solution of Eqs. (2.8) and (2.9) according to Eq. (2.10), see Tab. 2.8 and (b) for the corresponding optimal values of the modulus of subgrade reaction k and the additional uniform subgrade stress p_{aux} to be used in Eq. (2.8).

(d) Results from the structural analysis of the concrete slab "A10": bending moment per length: m_{xx} computed according to Eq. (2.23); see Tab. 2.8 and (b) for the corresponding optimal values of the modulus of subgrade reaction k and the additional uniform subgrade stress p_{aux}

(e) Results from the structural analysis of the concrete slab "A10": bending moment per length: m_{yy} computed according to Eq. (2.24); see Tab. 2.8 and (b) for the corresponding optimal values of the modulus of subgrade reaction k and the additional uniform subgrade stress p_{aux}

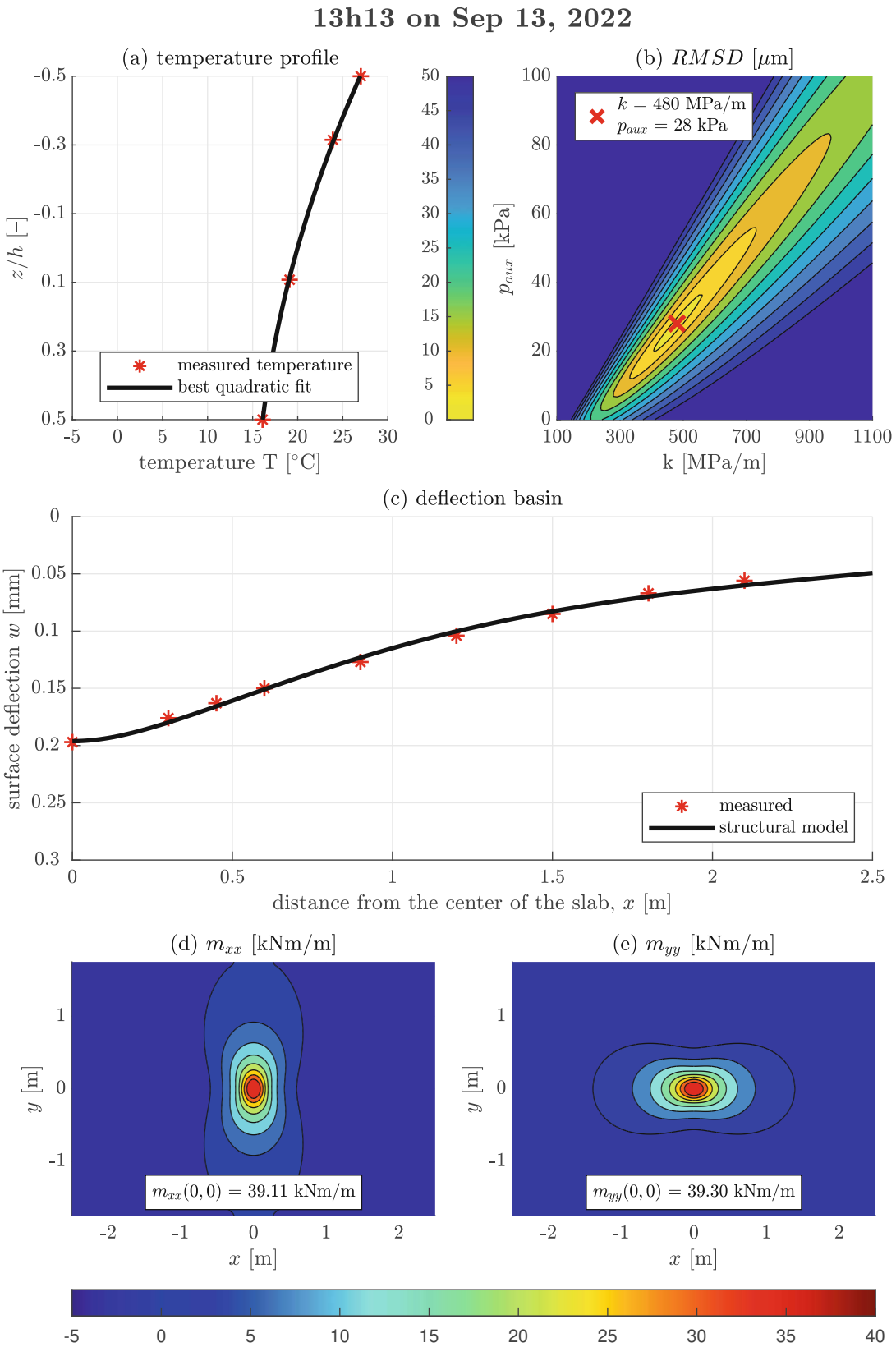

Fig. A.1: Temperature fit (a) and results of structural analysis (b)–(e) for the FWD test at 13h13 on Sep 13, 2022; the figure is continued on the following pages.

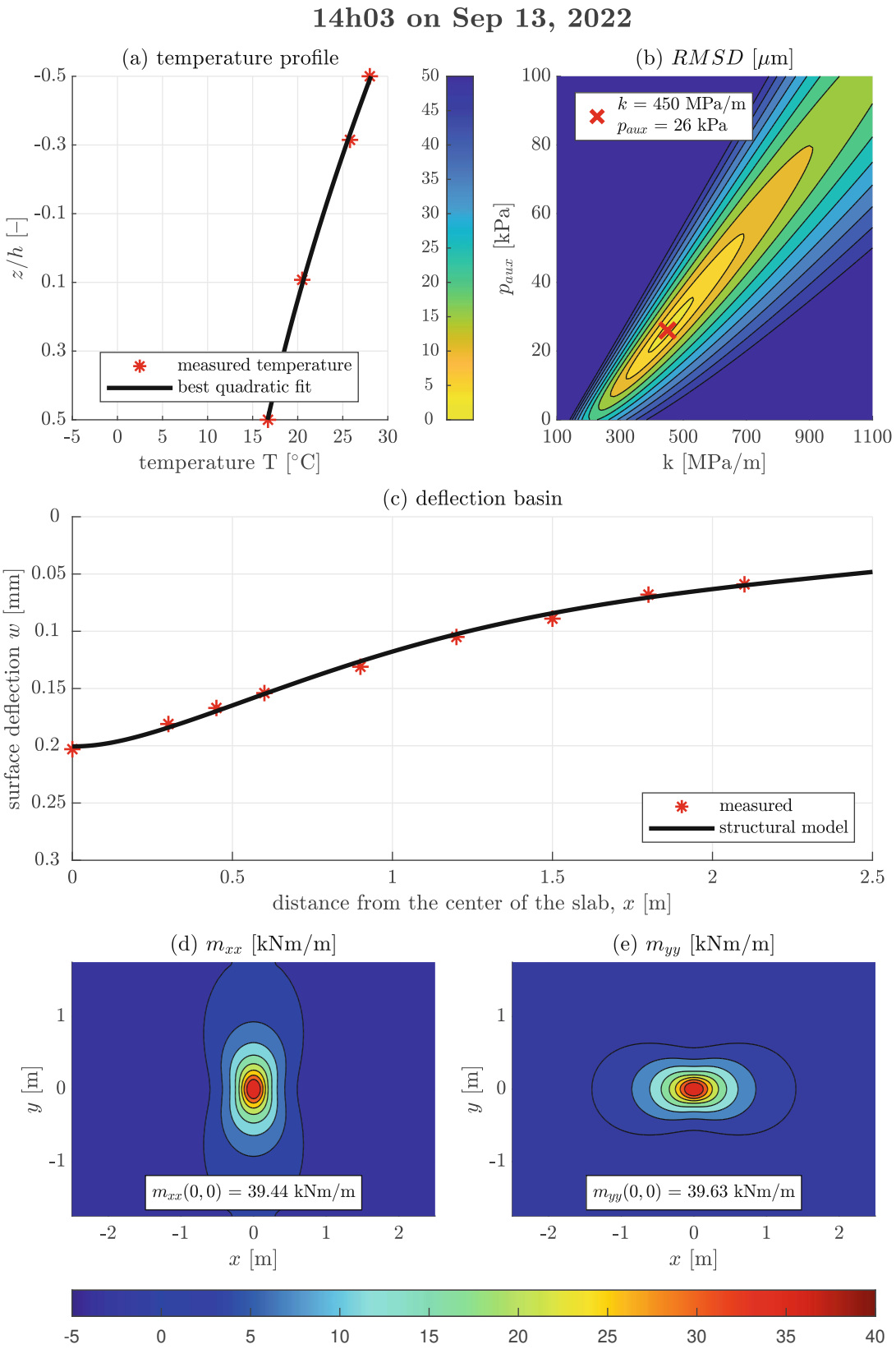

Fig. A.1 [cont'd]: Temperature fit (a) and results of structural analysis (b)–(e) for the FWD test at 14h03 on Sep 13, 2022.

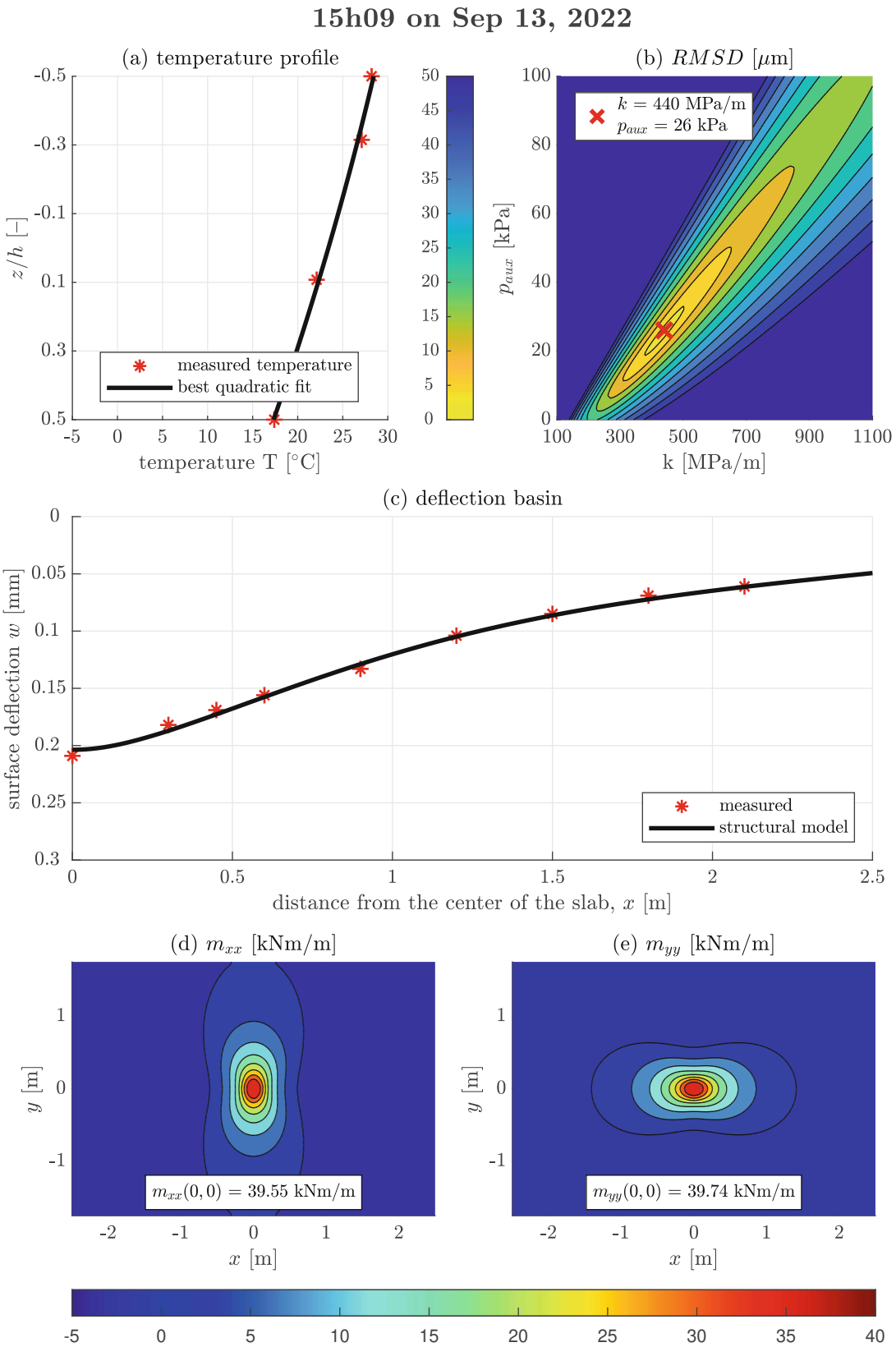

Fig. A.1 [cont'd]: Temperature fit (a) and results of structural analysis (b)–(e) for the FWD test at 15h09 on Sep 13, 2022.

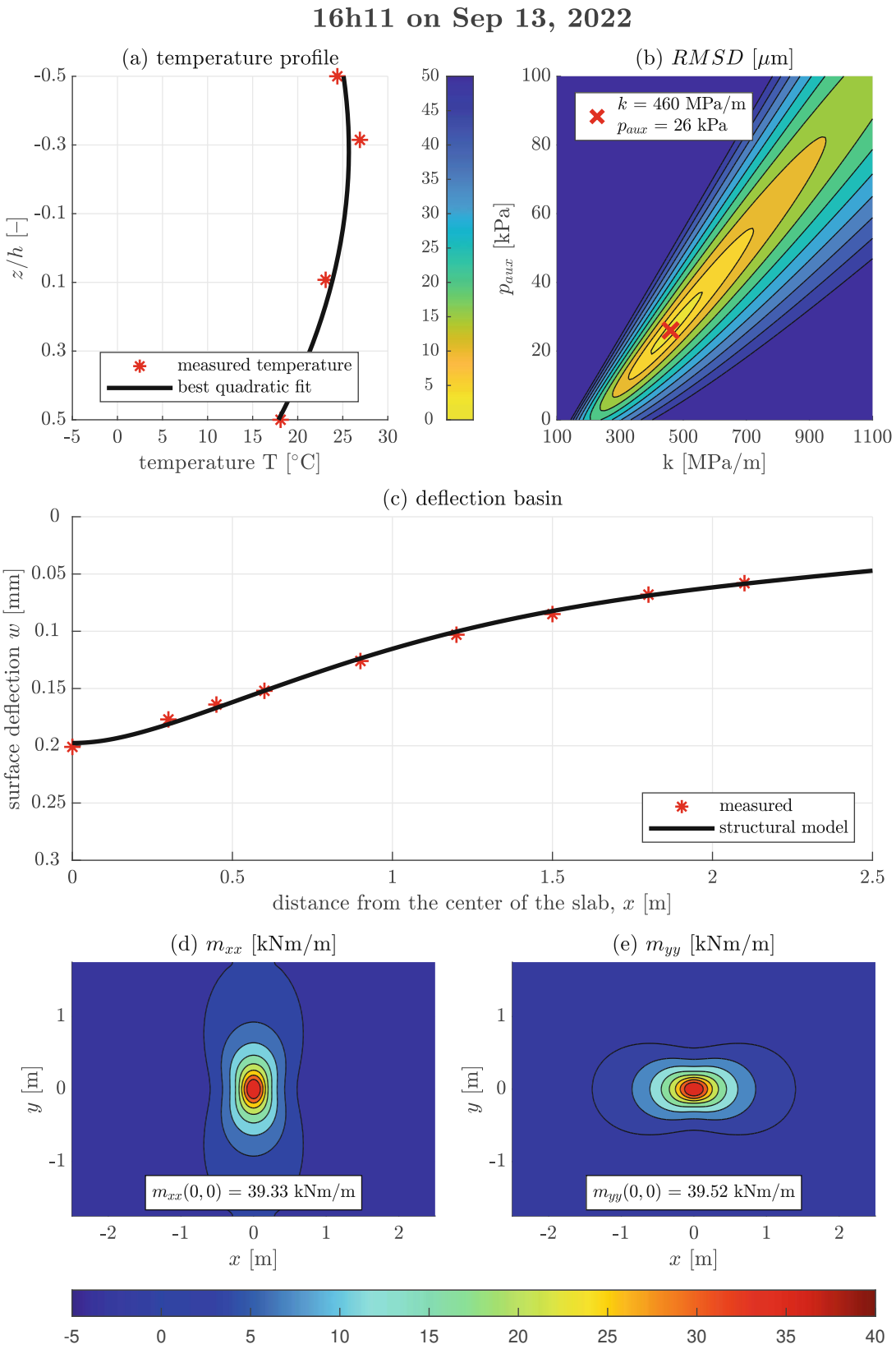

Fig. A.1 [cont'd]: Temperature fit (a) and results of structural analysis (b)–(e) for the FWD test at 16h11 on Sep 13, 2022.

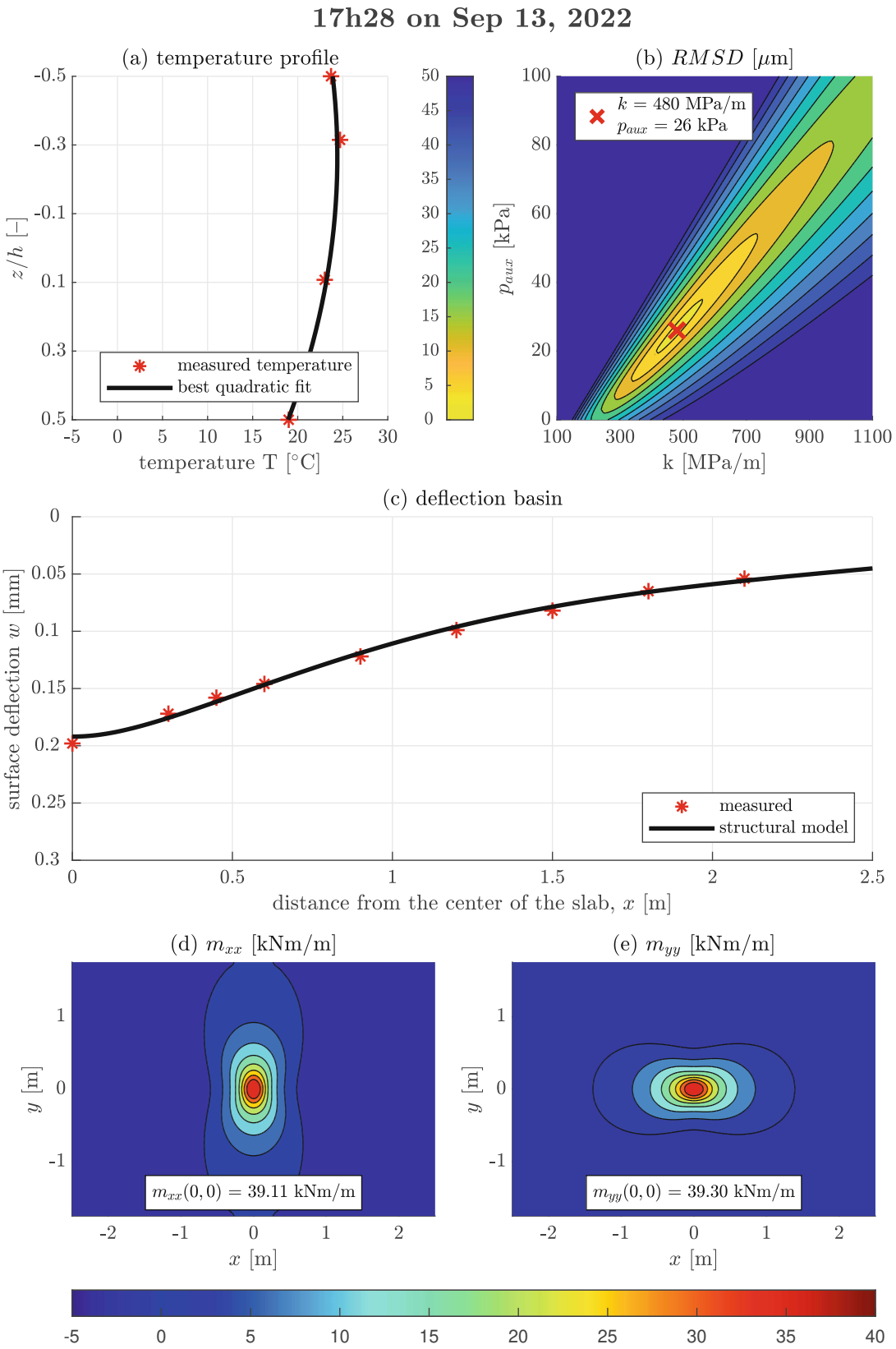

Fig. A.1 [cont'd]: Temperature fit (a) and results of structural analysis (b)–(e) for the FWD test at 17h28 on Sep 13, 2022.

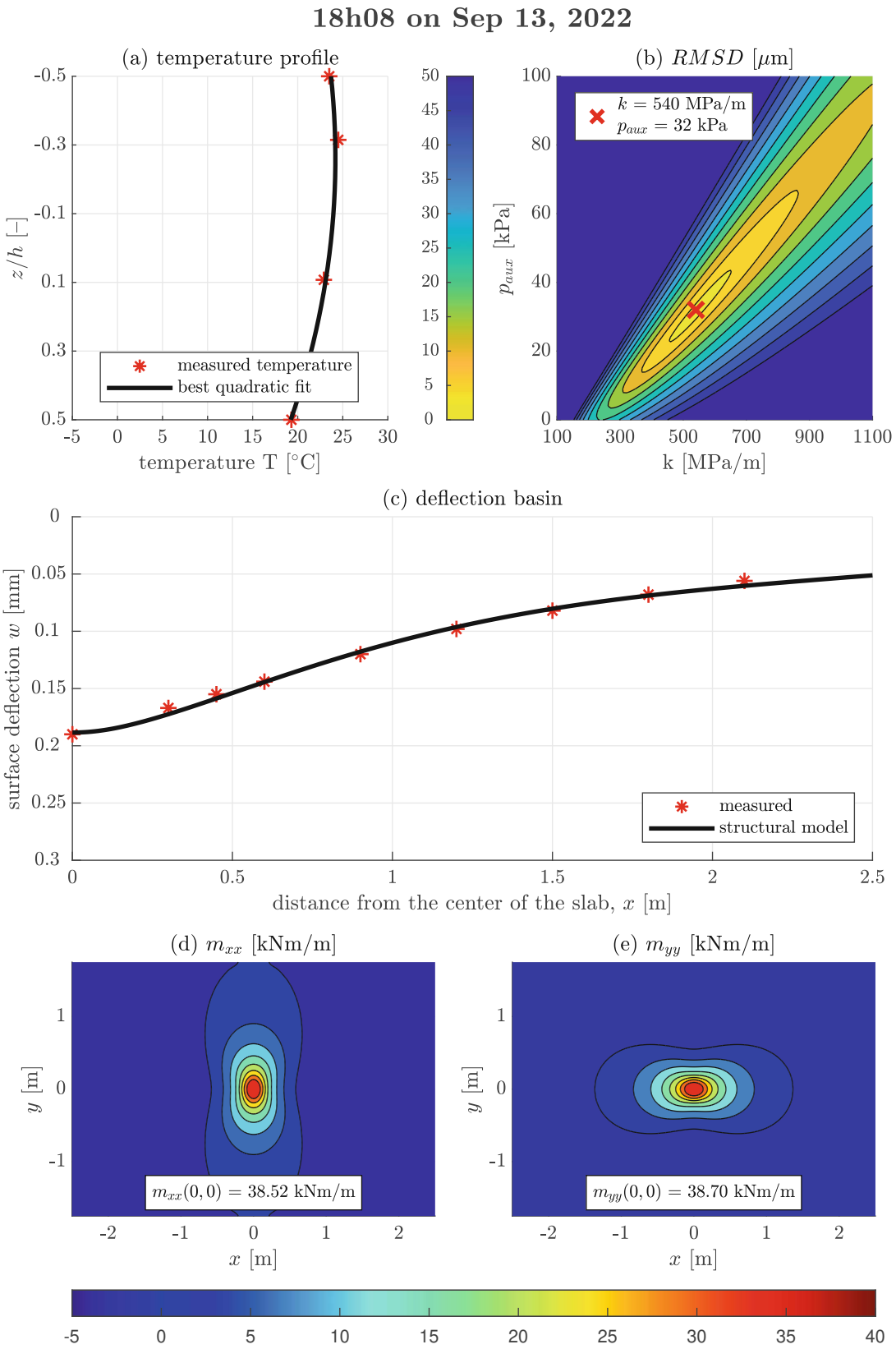

Fig. A.1 [cont'd]: Temperature fit (a) and results of structural analysis (b)–(e) for the FWD test at 18h08 on Sep 13, 2022.

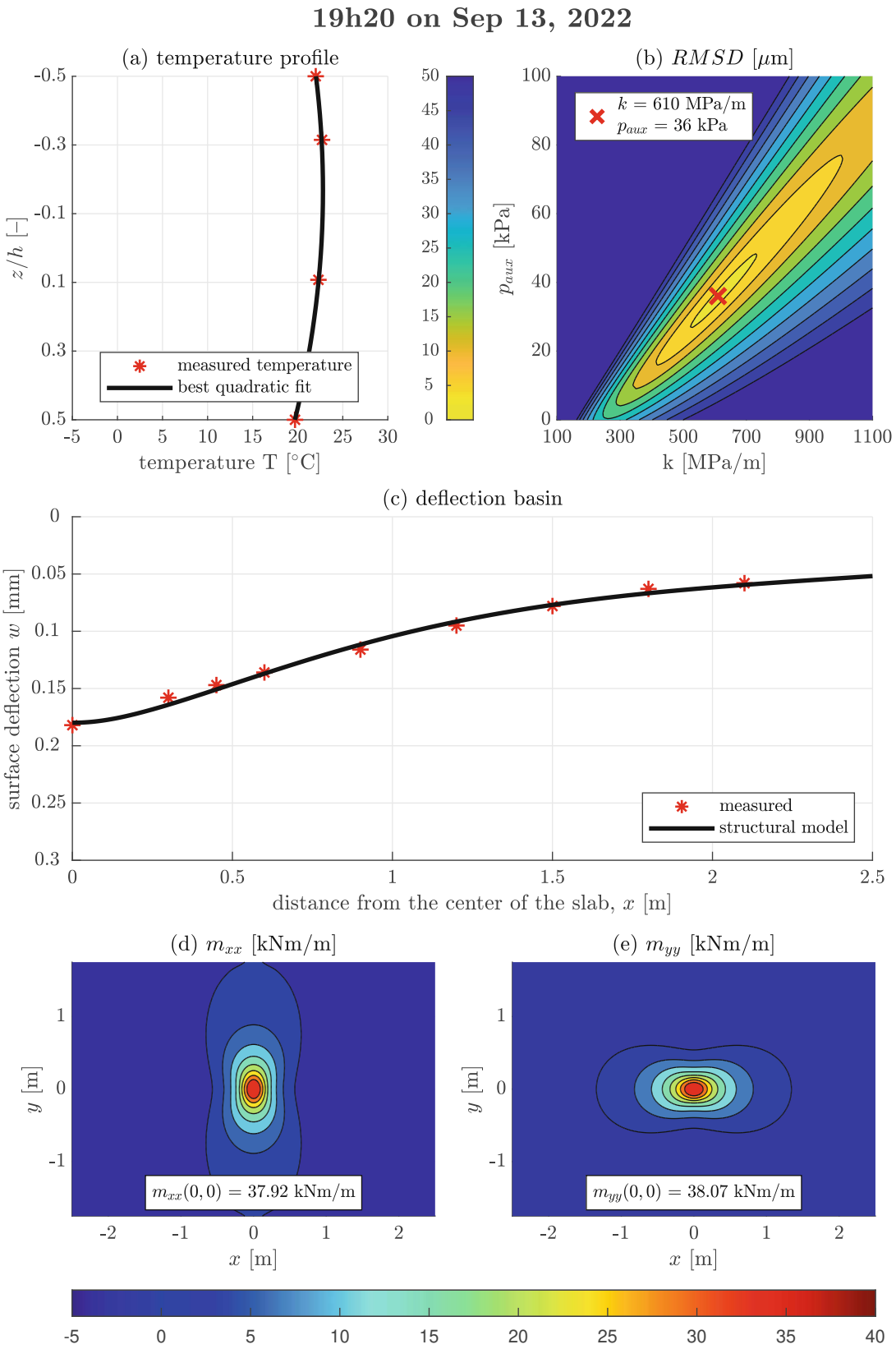

Fig. A.1 [cont'd]: Temperature fit (a) and results of structural analysis (b)–(e) for the FWD test at 19h20 on Sep 13, 2022.

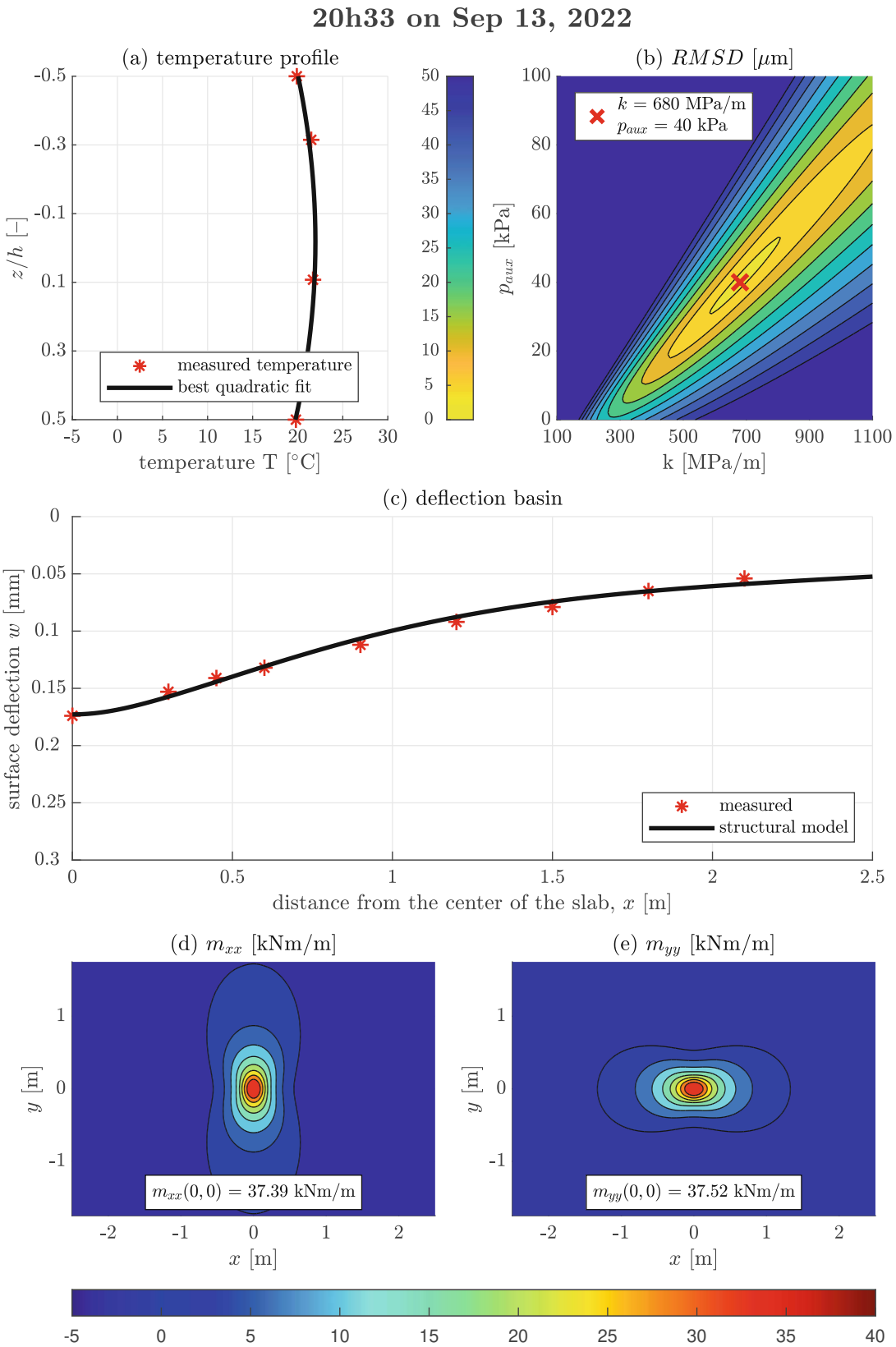

Fig. A.1 [cont'd]: Temperature fit (a) and results of structural analysis (b)–(e) for the FWD test at 20h33 on Sep 13, 2022.

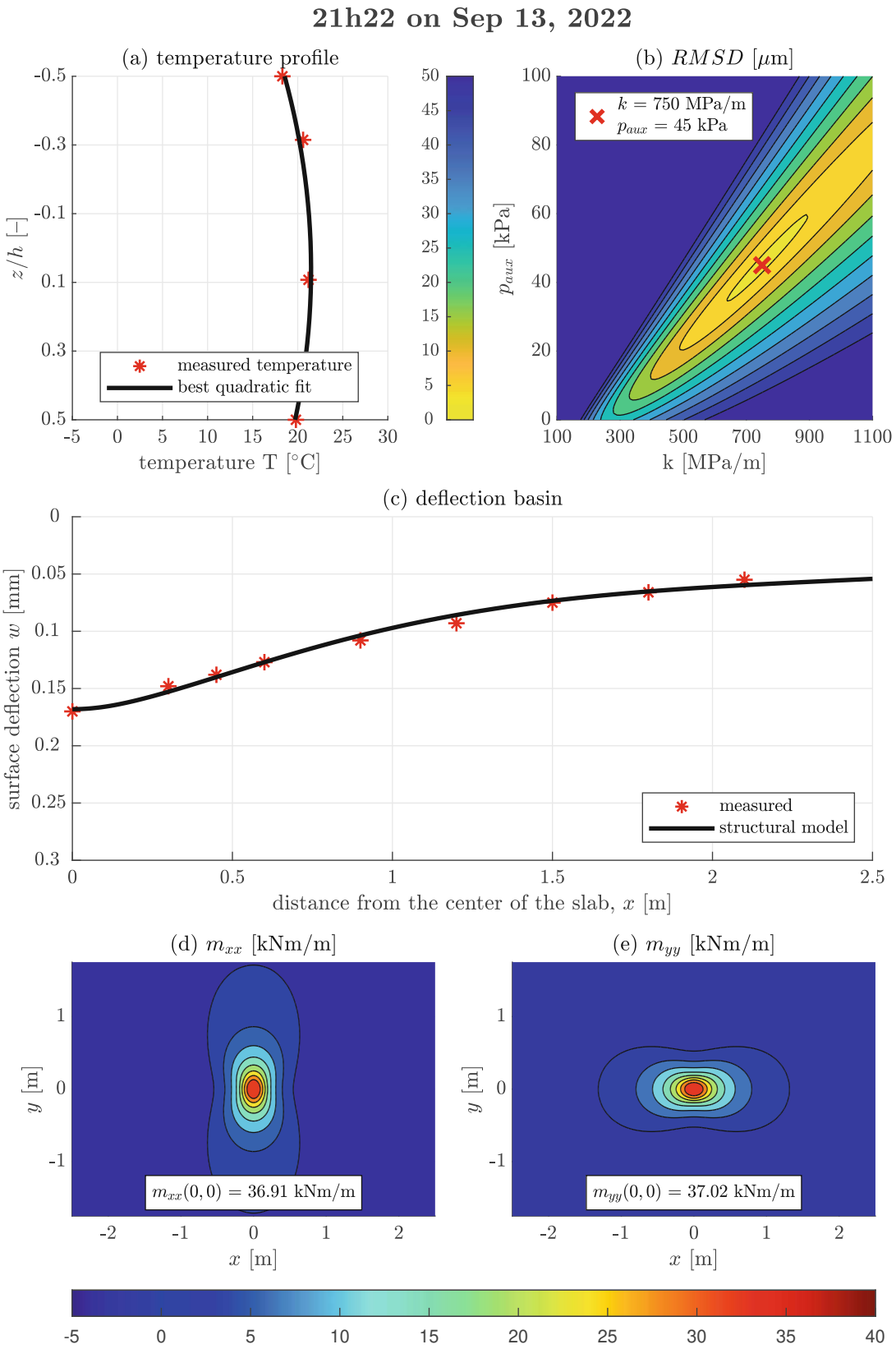

Fig. A.1 [cont'd]: Temperature fit (a) and results of structural analysis (b)–(e) for the FWD test at 21h22 on Sep 13, 2022.

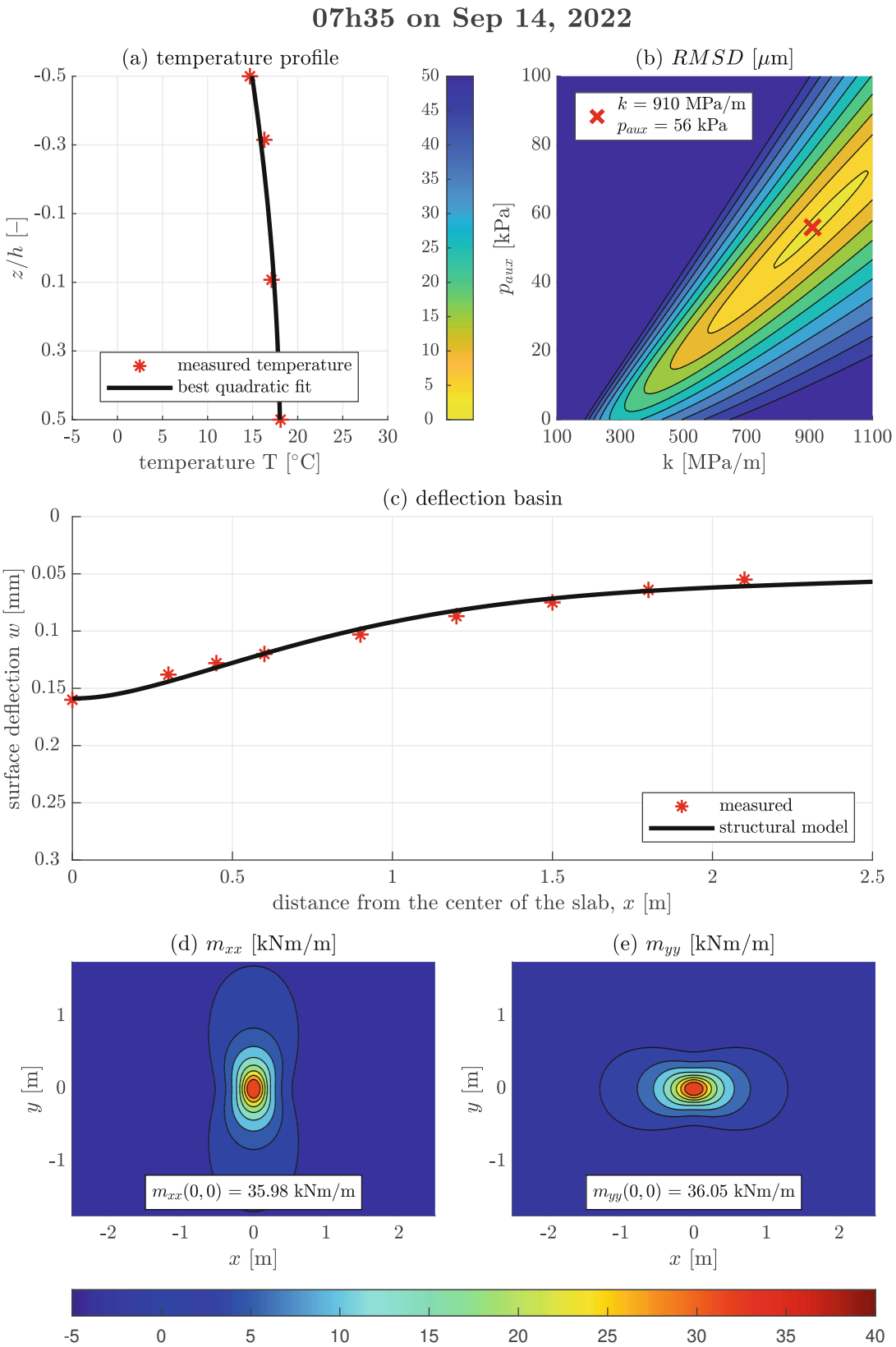

Fig. A.1 [cont'd]: Temperature fit (a) and results of structural analysis (b)–(e) for the FWD test at 07h35 on Sep 14, 2022.

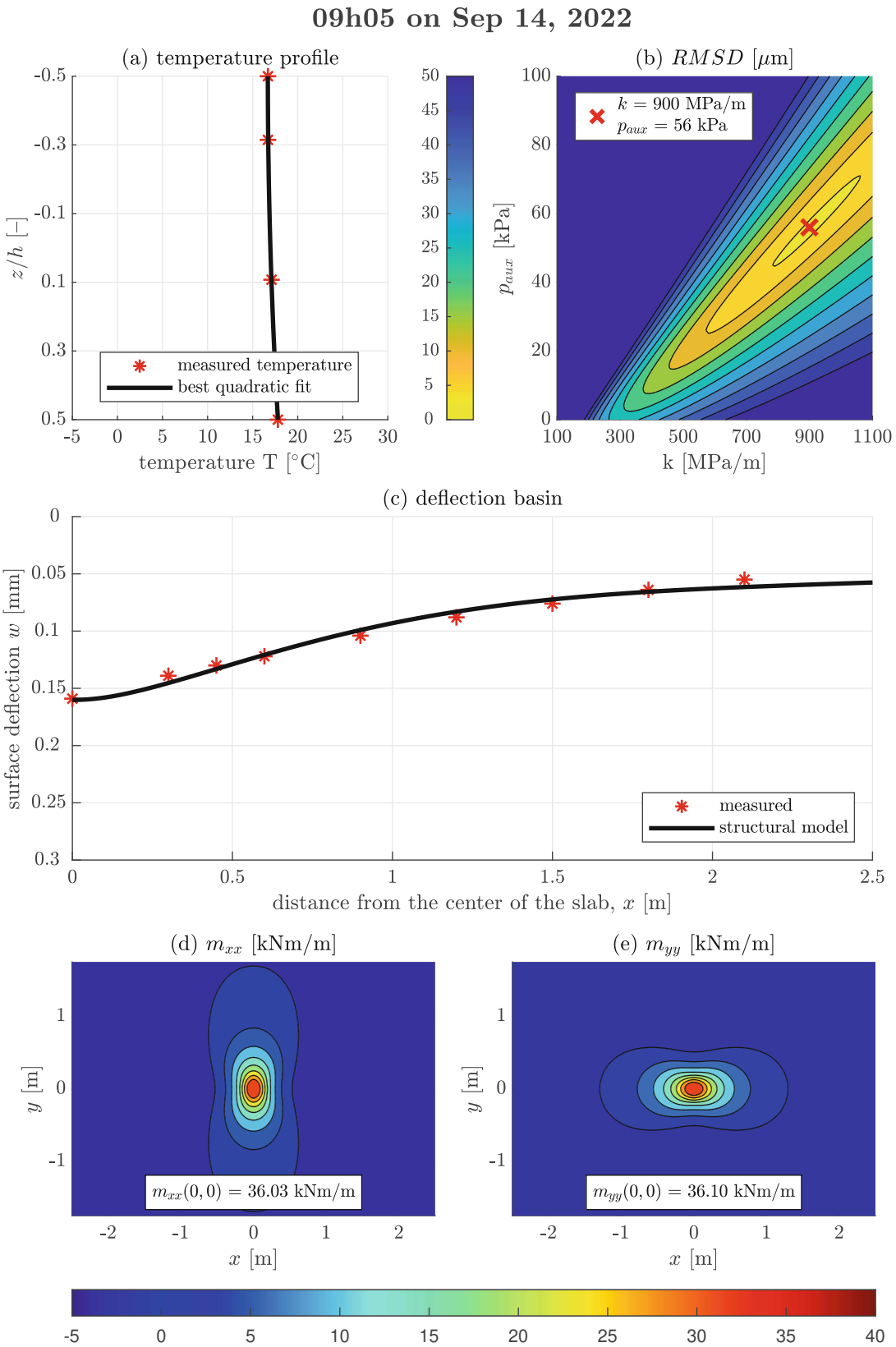

Fig. A.1 [cont'd]: Temperature fit (a) and results of structural analysis (b)–(e) for the FWD test at 09h05 on Sep 14, 2022.

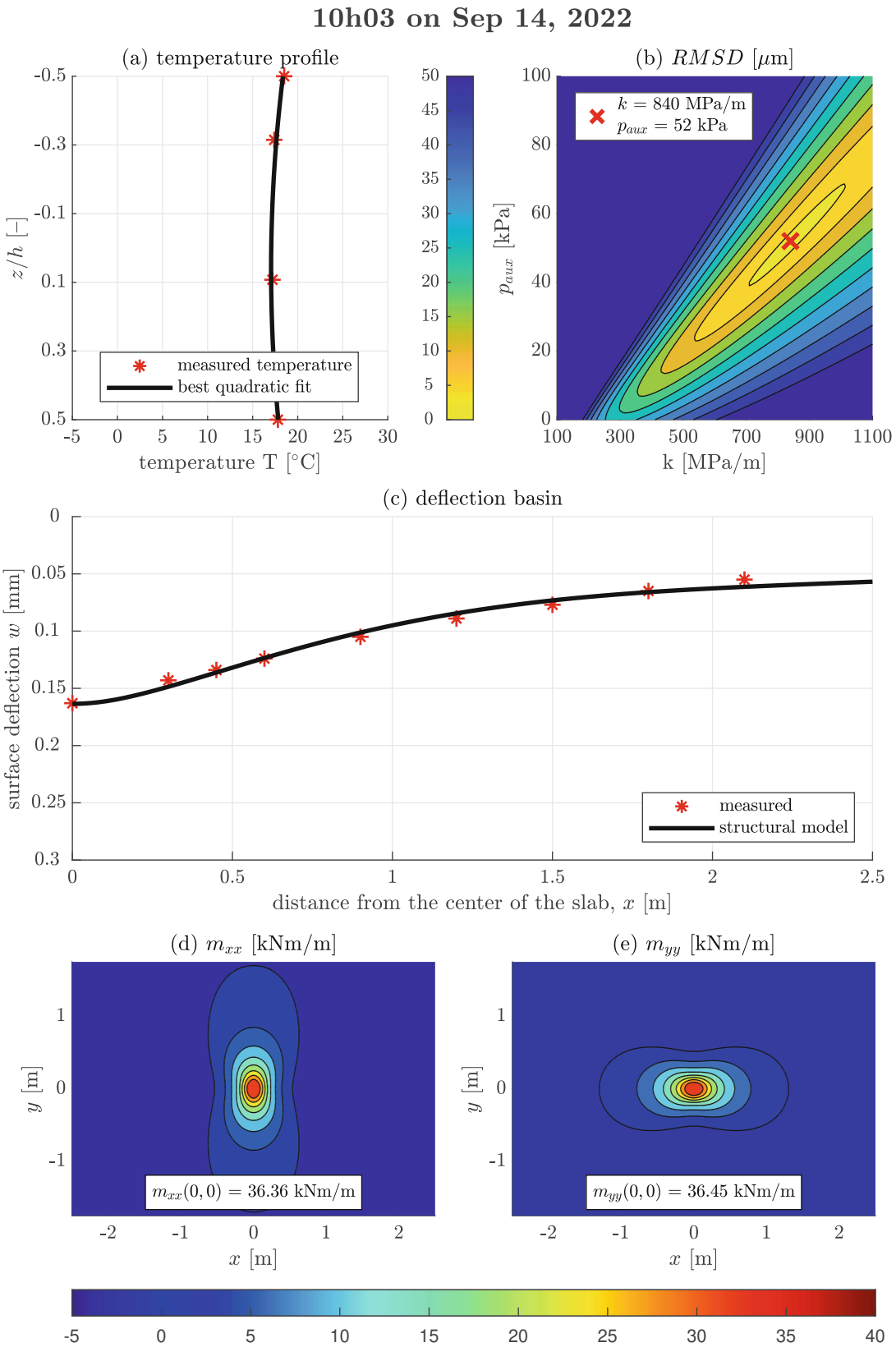

Fig. A.1 [cont'd]: Temperature fit (a) and results of structural analysis (b)–(e) for the FWD test at 10h03 on Sep 14, 2022.

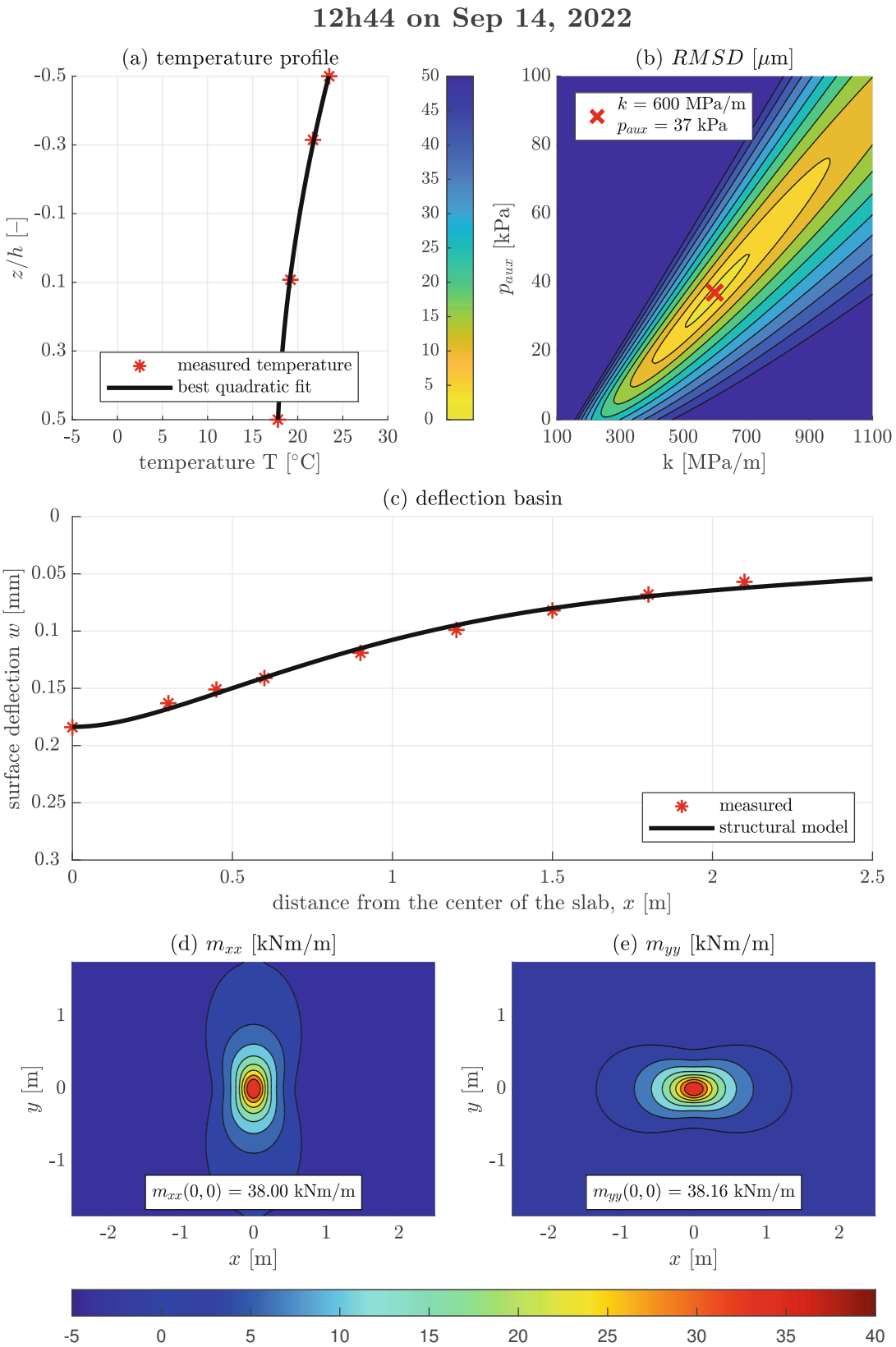

Fig. A.1 [cont'd]: Temperature fit (a) and results of structural analysis (b)–(e) for the FWD test at 12h44 on Sep 14, 2022.

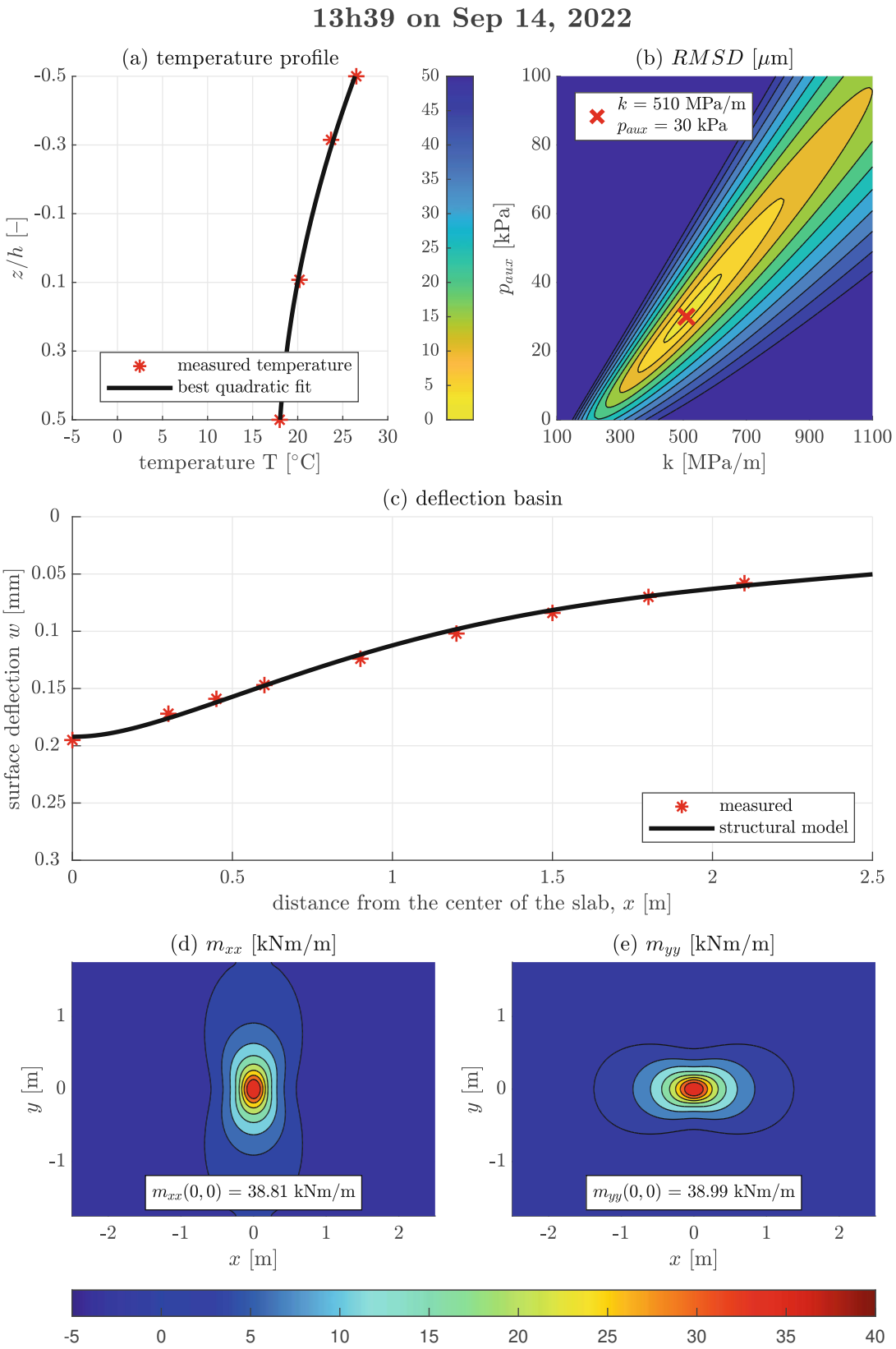

Fig. A.1 [cont'd]: Temperature fit (a) and results of structural analysis (b)–(e) for the FWD test at 13h39 on Sep 14, 2022.

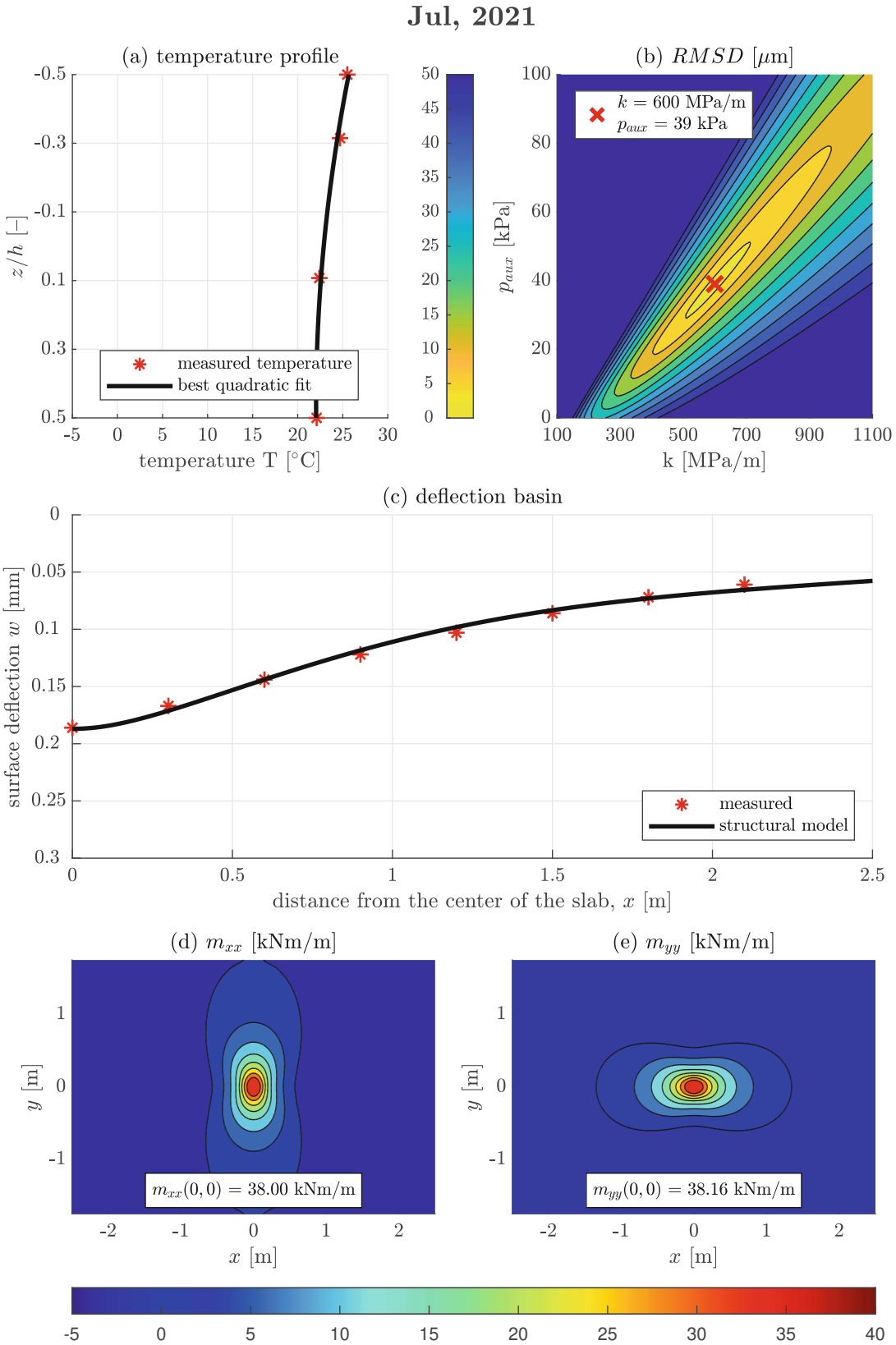

Fig. A.1 [cont'd]: Temperature fit (a) and results of structural analysis (b)–(e) for the FWD test in Jul, 2021.

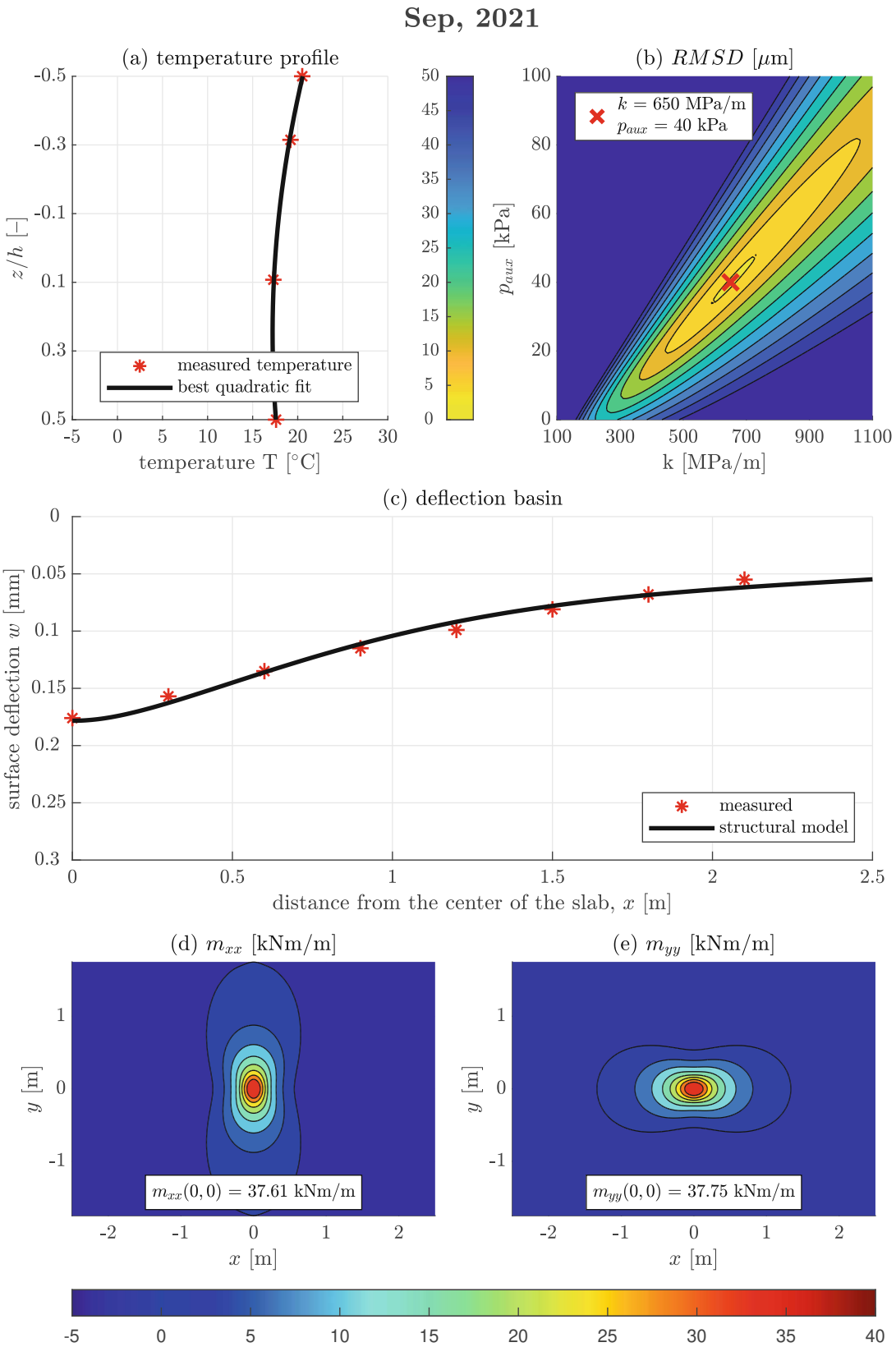

Fig. A.1 [cont'd]: Temperature fit (a) and results of structural analysis (b)–(e) for the FWD test in Sep, 2021.

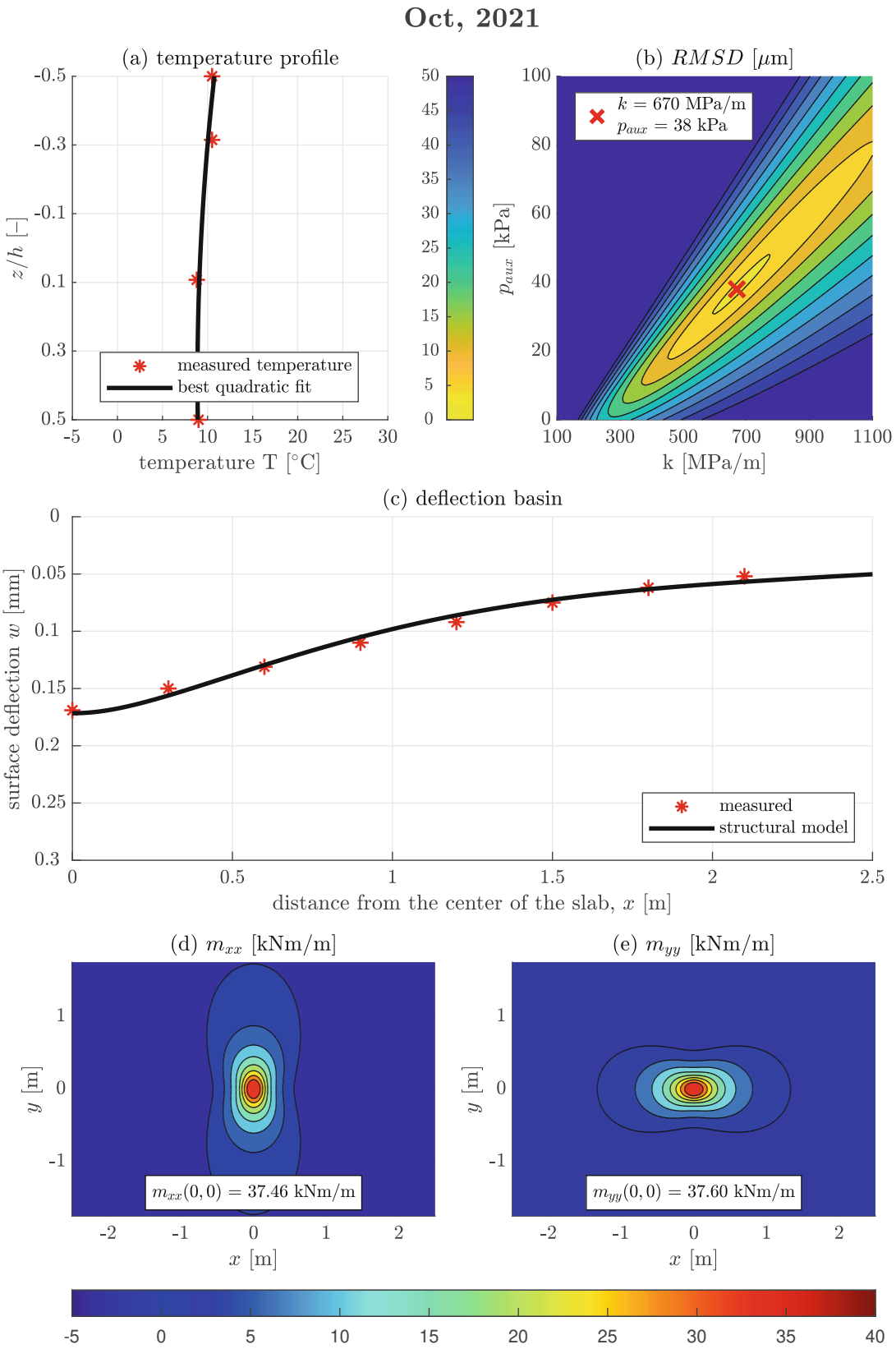

Fig. A.1 [cont'd]: Temperature fit (a) and results of structural analysis (b)–(e) for the FWD test in Oct, 2021.

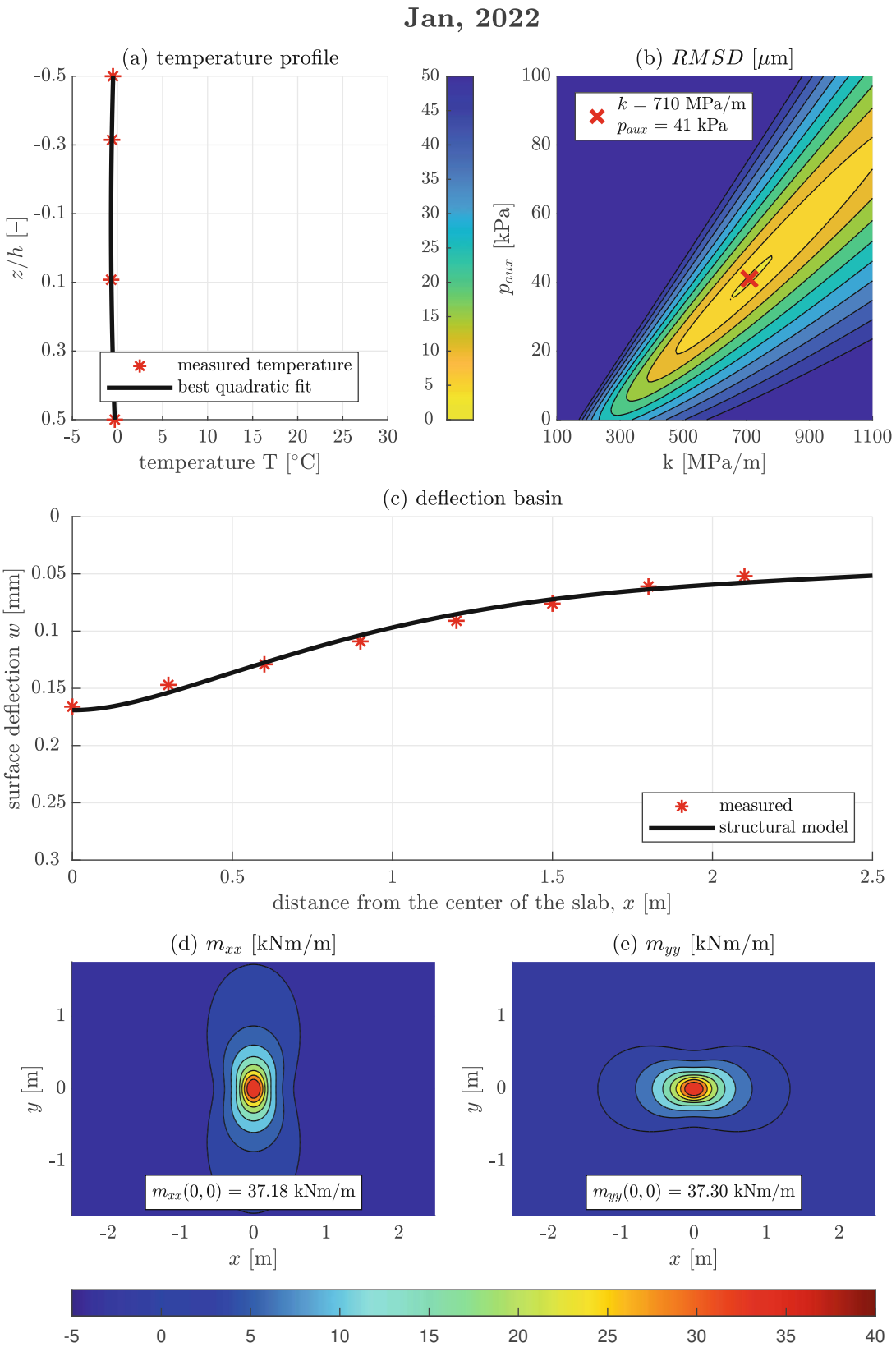

Fig. A.1 [cont'd]: Temperature fit (a) and results of structural analysis (b)–(e) for the FWD test in Jan, 2022.

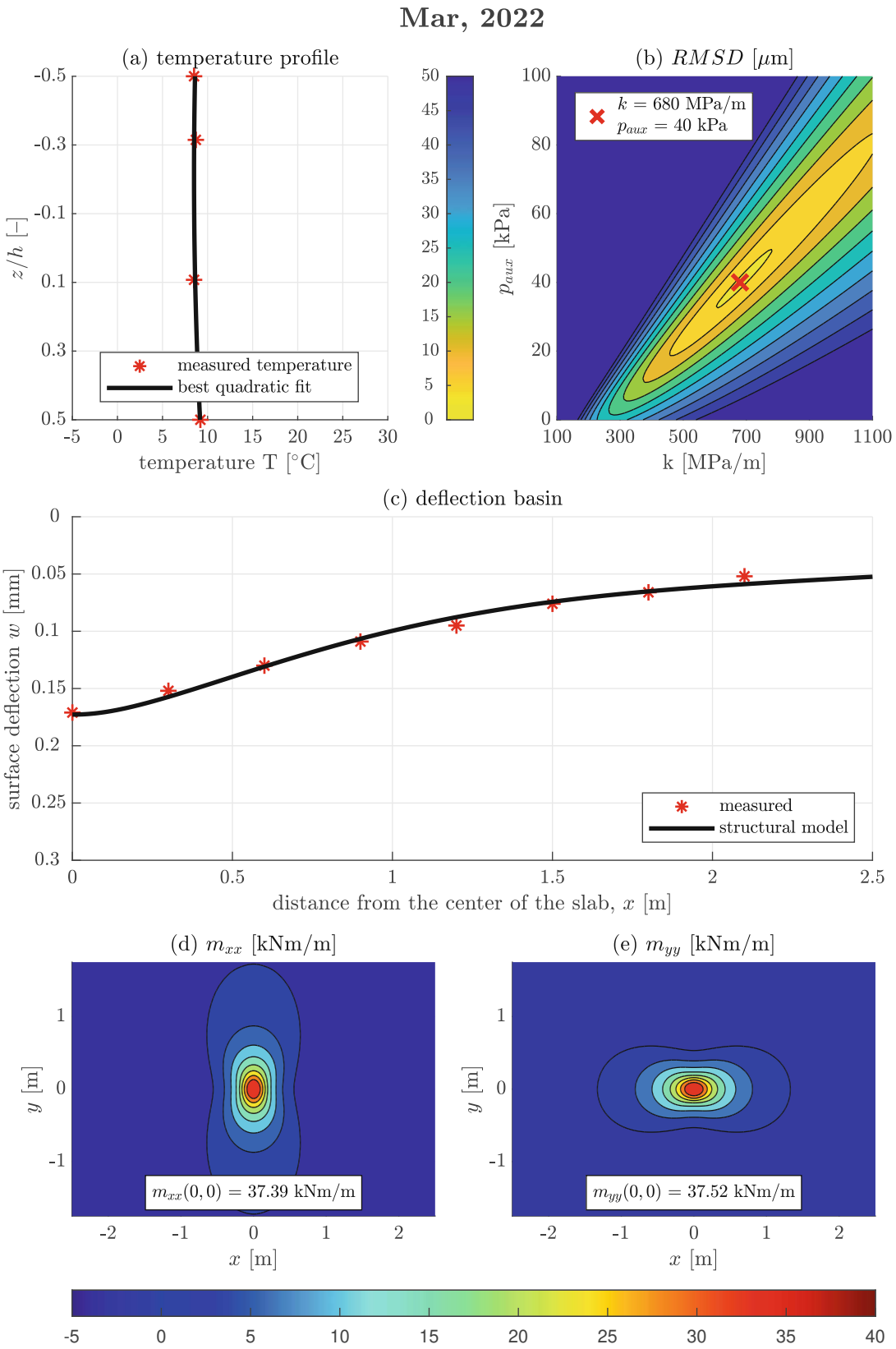

Fig. A.1 [cont'd]: Temperature fit (a) and results of structural analysis (b)–(e) for the FWD test in Mar, 2022.

Appendix B

List of Symbols

symbol	meaning
$A_0(t)$, $A_1(t)$, $A_2(t)$	optimal coefficients of the parabolic temperature fitting polynomial
a	thermal diffusivity
C_{mn}	Fourier coefficients
E	effective modulus of elasticity of concrete of the homogeneous slab
E_{bc}	modulus of elasticity of bottom concrete
E_{tc}	modulus of elasticity of top concrete
G_i	geophone i at radial distance r_i
$H(t-t_i)$	Heaviside function
h	thickness of the homogeneous concrete slab
h_{as}	thickness of the asphalt layer
h_{bc}	thickness of the bottom concrete layer
h_{cs}	thickness of the cement-stabilized granular layer
h_{tc}	thickness of the top concrete layer
h_{ub}	thickness of the unbound granular layer
i	summation index
K	flexural rigidity of the concrete slab
k	modulus of subgrade reaction used in load case 2
k_s	modulus of subgrade reaction used in load case 1
$\mathcal{L}^{ext}$, $\mathcal{L}^{int}$	virtual power of external forces and internal forces, respectively
ℓ_x	length of the concrete slab
ℓ_y	width of the concrete slab
m	summation index
m_{xx}, m_{yy}	bending moments per length
m_{xy}, m_{yx}	twisting moments per length
N	number of specific values of $\kappa^e_{hss}(t_i)$ and $\kappa^e_{par}(t_i)$ considered in $RMSD$
N_g	number of geophones
N_m	number of deflection modes considered with respect to the x-direction
N_n	number of deflection modes considered with respect to the y-direction
N_T	number of temperature increments
n	summation index
n_{FWD}	number of FWD tests performed right after another
$p(x,y)$	external load resulting from FWD testing
p_{aux}	additional uniform subgrade stress
q	dead load of the concrete slab
q_x, q_y	shear forces per length
$RMSD$	root mean square difference between $\kappa^e_{hss}(t_i)$ and $\kappa^e_{par}(t_i)$

symbol	meaning
$RMSD(k, p_{aux})$	root mean square difference between $w_i(x_i)$ and $w(k, p_{aux}; x_i, y=0)$
r	radial distance, measured from the center of the slab
r_c	radius of the load plate
r_i	radial distance of geophone G_i, measured from the center of the slab
$T(z,t)$	temperature field in slab-related coordinates
$T(\bar{z},t)$	temperature field in half-space-related coordinates
T_i	temperature measured in depth $\bar{z}_i$
T_{ini}	uniform initial temperature of the half-space
T_{ref}	reference temperature
T_{surf}	measured surface temperature at $\bar{z}_{surf} = 0.0\,\mathrm{m}$
$T^{top}(t)$	measured surface temperature history of the concrete slab
t	time variable
t_1	initial time instant of simulation
t_i	simulation time at the i^{th} temperature increment
t_{sim}	elapsed simulation time since initial time instant
$w(x,y)$	deflection basin resulting from FWD testing
$\hat{w}$	virtual velocity field
w_i	average value of the maximum surface deflection measured by geophone G_i in n_{FWD} subsequent FWD tests
$w_{par}(r)$	approximated deflection basin between the first and the second geophone
x, y, z	concrete-slab-related Cartesian coordinates
x_i	x-coordinate of geophone G_i
z_1–z_4	concrete-slab-related z-coordinates of the installed temperature sensors
$\bar{z}$	half-space related coordinate
$\bar{z}_i$	depth at which the temperature T_i is measured
$\bar{z}_{surf}$	depth at which the surface temperature T_{surf} is measured
α_T	coefficient of thermal expansion of concrete
$\Delta\Delta$	bilaplacian operator
ΔT_i^{top}	i^{th} temperature increment at the surface of the concrete slab
$\Delta\kappa^e(t)$	difference between $\kappa^e_{hss}(t_i)$ and $\kappa^e_{par}(t_i)$
Δt	time step size of the surface temperature history
$\varepsilon^e(t)$	thermal eigenstretch of the midplane of the slab
$\kappa^e(t)$	thermal eigencurvature of the concrete slab
$\kappa^e_{hss}(t_i)$	thermal eigencurvature according to half-space simulation
$\kappa^e_{par}(t_i)$	thermal eigencurvature according to parabolic temperature fit
ν	Poisson's ratio of concrete
ρ	effective mass density of concrete of the homogeneous slab
ρ_{bc}	mass density of bottom concrete
ρ_{tc}	mass density of top concrete
$\boldsymbol{\sigma}$	Cauchy stress tensor
σ_{eigen}	thermal eigenstress of concrete
σ_{xx}, σ_{yy}	normal stresses in the x- and y-direction
σ^{par}_{xx}	FWD-induced tensile stresses estimated by engineering approach
σ_{xy}, σ_{yx}	shear stresses in the x-y plane
σ_{xz}, σ_{yz}	shear stresses in the x-z and y-z plane
$\max\sigma_{xx}$, $\max\sigma_{yy}$	largest FWD-induced principal tensile stresses in x- and y-direction

Bibliography

[1] J. M. Armaghani, T. J. Larsen, and L. L. Smith. "Temperature Responce of Concrete Pavements". In: *Transportation Research Record* 1121 (1987), pp. 23–33.

[2] R. Blab. "Einflussgrößen bei der Bemessung hochbelasteter Betonstraßen (in German)". In: *Betonstraßen*. Wien, 2005, pp. 22–30.

[3] R. Blab, L. Eberhardsteiner, K. Haselbauer, B. Marchart, and T. Hessmann. *Implementierung des GVO und LCCA-Ansatzes in die österreichische Bemessungsmethode für Straßenoberbauten OBESTO*. Wien: Bundesministerium für Verkehr, Innovation und Technologie; ÖBB-Infrastruktur AG; Autobahnen- und Schnellstraßen-Finanzierungs Aktiengesellschaft, 2014.

[4] R. D. Bradbury. *Reinforced concrete pavements*. Washington, D.C.: Wire Reinforcement Institute, 1938.

[5] H. S. Carslaw and J. C. Jaeger. *Conduction of Heat in Solids*. 2. ed., 1. issued in paperback. Oxford: Clarendon Press, 1986.

[6] B. Choubane and M. Tia. "Nonlinear Temperature Gradient Effect on Maximum Warping Stresses in Rigid Pavements". In: *Transportation Research Record* 1370 (1992), pp. 11–19.

[7] R. Díaz Flores, M. Aminbaghai, L. Eberhardsteiner, R. Blab, M. Buchta, and B. L. A. Pichler. "Multi-directional Falling Weight Deflectometer (FWD) testing and quantification of the effective modulus of subgrade reaction for concrete roads". In: *International Journal of Pavement Engineering* 24(1) (2021), p. 2006651.

[8] R. Díaz Flores, M. Aminbaghai, L. Eberhardsteiner, R. Blab, M. Buchta, and B. L. A. Pichler. "T-shaped arrangement of geophones for rapid quantification of asymmetric behaviour of concrete slabs in central FWD tests". In: *International Journal of Pavement Engineering* 24(1) (2023), p. 2179050.

[9] R. Díaz Flores, V. Donev, M. Aminbaghai, R. Höller, L. Eberhardsteiner, M. Buchta, and B. L. A. Pichler. "Asphalt-related temperature correction of deflections measured in central FWD tests on a concrete-over-asphalt composite pavement". In: *International Journal of Pavement Engineering* 25(1) (2024), p. 2301454.

[10] Dlubal Software GmbH. *RFEM 5*. Version 5.31.01. Germany, 2023.

[11] V. Donev, R. Díaz Flores, L. Eberhardsteiner, L. Zelaya-Lainez, C. Hellmich, M. Buchta, and B. L. A. Pichler. "Instrumentation of Field-Testing Sites for Dynamic Characterization of the Temperature-Dependent Stiffness of Pavements and Their Layers". In: *Structural Control and Health Monitoring* 2023 (2023), pp. 1–25.

[12] L. Eberhardsteiner and R. Blab. "Design of bituminous pavements – a performance-related approach". In: *Road Materials and Pavement Design* 20(2) (2019), pp. 244–258.

[13] L. Eberhardsteiner, K. Flotin, K. Bayraktarova, K. Haselbauer, B. L. A. Pichler, M. Aminbaghai, P. Pratscher, and R. Blab. *Optimierte Bemessung starrer Aufbauten OBESTAS (in German)*. Wien: Bundesministerium für Verkehr, Innovation und Technologie; ÖBB-Infrastruktur AG; Autobahnen- und Schnellstraßen-Finanzierungs Aktiengesellschaft, 2016.

[14] J. Eisenmann and G. Leykauf. “Verkehrsflächen aus Beton”. In: *Beton-Kalender 2007*. Berlin, 2006, pp. 93–263.

[15] FSV. *RVS 03.08.63 Oberbaubemessung*. Wien: Forschungsgesellschaft Straße – Schiene – Verkehr, 2016.

[16] P. Germain. “Sur l’application de la méthode des puissances virtuelles en mécanique des milieux continus (in French)”. In: *Comptes Rendus de l’Académie des Sciences Paris, Série A* 274 (1972), pp. 1051–1055.

[17] H. K. Hilsdorf and C. E. Kesler. “Fatigue Strength of Concrete Under Varying Flexural Stresses”. In: *ACI Journal Proceedings* 63(10) (1966), pp. 1059–1076.

[18] R. Höller, M. Aminbaghai, L. Eberhardsteiner, J. Eberhardsteiner, R. Blab, B. L. A. Pichler, and C. Hellmich. “Rigorous amendment of Vlasov’s theory for thin elastic plates on elastic Winkler foundations, based on the Principle of Virtual Power”. In: *European Journal of Mechanics - A/Solids* 73 (2019), pp. 449–482.

[19] S. J. Schmid, R. Díaz Flores, M. Aminbaghai, L. Eberhardsteiner, H. Wang, R. Blab, and B. L. A. Pichler. “Significance of eigenstresses and curling stresses for total thermal stresses in a concrete slab, as a function of subgrade stiffness”. In: *International Journal of Pavement Engineering* 24(2) (2023), p. 2091136.

[20] X. P. Shi, T. F. Fwa, and S. A. Tan. “Flexural Fatigue Strength of Plain Concrete”. In: *ACI Materials Journal* 90(5) (1993), pp. 435–440.

[21] L. W. Teller and E. C. Sutherland. “The Structural Design of Concrete Pavements; Part 2: Oberserved Effects of Variations in Temperature and Moisture on the Size, Shape, and Stress Resistance of Concrete Pavements Slabs”. In: *Public Roads* 16(9) (1935), pp. 169–197.

[22] R. Tepfers. “Tensile Fatigue Strength of Plain Concrete”. In: *ACI Journal Proceedings* 76(8) (1979), pp. 919–933.

[23] R. Tepfers and T. Kutti. “Fatigue Strength of Plain, Ordinary, and Lightweight Concrete”. In: *ACI Journal Proceedings* 76(5) (1979), pp. 635–652.

[24] The MathWorks Inc. *MATLAB R2024b*. Version 24.2.0.2712019. Natick, Massachusetts, United States, 2024.

[25] J. Thomlinson. “Temperature variations and consequent stresses produced by daily and seasonal temperature cycles in concrete slabs”. In: *Concrete Constructional Engineering* 36(6) (1940), pp. 298–307.

[26] U.S Department of Transportation. *LTPP Manual for Falling Weight Deflectometer Measurements Operational Field Guidelines*. Version 3.1. United States. Federal Highway Administration. Office of Infrastructure Research and Development, 2000.

[27] V. Z. Vlasov and U. N. Leont’ev. *Beams, plates and shells on elastic foundations*. Jerusalem: Israel Program for Scientific Translations, 1966.

[28] H. Wang, R. Höller, M. Aminbaghai, C. Hellmich, Y. Yuan, H. A. Mang, and B. L. A. Pichler. “Concrete pavements subjected to hail showers: A semi-analytical thermoelastic multiscale analysis”. In: *Engineering Structures* 200 (2019), p. 109677.

[29] H. M. Westergaard. “Analysis of Stresses in Concrete Roads Caused by Variations of Temperature”. In: *Public Roads* 8(3) (1927), pp. 54–60.

[30] H. M. Westergaard. “Stresses in Concrete Pavements Computed by Theoretical Analysis”. In: *Public Roads* 7(2) (1926), pp. 25–35.

[31] E. Winkler. *Die Lehre von der Elasticitaet und Festigkeit mit besonderer Rücksicht auf ihre Anwendung in der Technik, für polytechnische Schulen, Bauakademien, Ingenieure, Maschinenbauer, Architekten etc. (in German)*. 1. Theil. Prag: Dominicus, 1867.